Deutsches Zentrum
für Luft- und Raumfahrt e.V.

Final Report IB554-06/04

SANTANA-
Smart Antenna Terminal Design

Liu Ying

Institut für Kommunikation und Navigation
Oberpfaffenhofen

DLR

Abstract

This project is embedded in SANTANA (Smart Antenna Terminal) project. The project goal is to design a Ka-band circularly polarized antenna radiator for the receiver SANTANA system. The research work focuses on two types of circularly polarized antennas: aperture-coupled patch antenna and CPW-fed patch antenna. A two steps design process is used. Firstly, only the antennas and their feed structure are designed and optimized. Secondly, a via-transition to connect to a MMIC layer is added. When designing the aperture-coupled patch antenna, a simplified cavity model method for computation is used to achieve the computational model. Both of the structures are optimized. The aperture-coupled microstrip feed patch antenna is selected to fabricate, so that a transition-VIA is added to the bottom of it. After comparing simulation results and measurement results, the two types of radiators‘s different behavior can be easily observed. Also, the influences of the transition-VIA to the radiator are obviously seen.

Preface

This work was submitted as a Master thesis at the international Master program "Hardware for Wireless Communication" (COMAS) at Chalmers University of Technology.

The Smart Antenna Terminal Design project was funded by German Ministry of Education and Research (BMBF) under the administration of German Aerospace Center (DLR) covered by research contracts 50YB0101 and 50YB0104. The project duration was from August 2nd, 2004 to April 30th, 2005. This project was supervised by Dr. Michael Thiel, antenna group, DLR. The examiner was Prof. Per-Simon Kildal, Head, Antenna group, Chalmers University of Technology.

CONTENTS

LIST OF FIGURES

ABBREVIATION LIST

CPW	Coplanar Waveguide
CP	Circular Polarization
LHCP	Left Hand Circular Polarization
RHCP	Right Hand Circular Polarization
MMIC	Monolithic Microwave Integrated Circuit
PPM	Parallel plate modes
RHCP	Right Hand Circular Polarization
TEM	Transverse electromagnetic
TRL	Through Reflect Line
VSWR	Voltage of Standing Wave Ratio

1 Introduction

1.1 Overview of Smart Antenna Terminal (SANTANA)

The demand for broadband data communication is increasing rapidly nowadays. Satellite systems offer unique possibilities to connect professional mobile users to broadband data networks and services. Mobile satellite broadband applications will push the demand for novel smart antenna terminals to replace conventional reflector-type terminals. Due the large bandwidth requirement, most of the broadband satellite systems choose Ka-band (approximately 20 GHz for the downlink and 30 GHz for the uplink) as their operating bandwidth [1].

Generally speaking, a smart antenna is a multi-element antenna arranged in a special form and connected through complex weights. The pattern of the multi-antenna element can be adjusted by the weights. In SANTANA project, the digital beam-forming (DBF) is used to adapt the directional characteristics to the environment and to generate multiple beam patterns. This makes it very important to choose the appropriate components, substrate material and technologies when designing the single element of the antenna array in order to allow a cost-efficient implementation. Furthermore, due to the very small wavelengths in the Ka-band, the integration of the antenna elements together with the active MMIC electronics and the digital circuitry is a particularly critical issue as it leads to high packaging densities [2]. These constraints have to be taken into account when designing a single element radiator. The task of this Master thesis Project is to develop a circularly polarized radiator for the receiver system of the smart antenna. Suitable structures for circular polarization are chosen and simulated.

1.2 Software tools

All the simulations are carried out with Ansoft Designer V2.1 and Ansoft HFSS v9.2 Ansoft Designer is developed based on Method of Moment (MoM), which is very efficient for planar antennas. Firstly, one can use the “patch estimator” function to get a good start point together with theoretical computation. Then, this model is simulated and optimized. The “Parametric” function is very useful when tuning the different parameters of the antenna to study their influences on the radiation characteristics. Until the simulation results are close to the requirements, “Optimization” function can be used to achieve the goal. By setting up different “Deembed distances”, one can check the input impedance at different positions along the feedline. After the antenna models are qualified in Designer, they are converted to Ansoft HFSS V9.2 to recheck again. A small frequency-band shift of about 50MHz to 200MHz has been observed. It is because the HFSS is based on the Finite Element Method (FEM). In this case, some tuning is necessary. Finally, some fabrication considerations also are taken into account, such as glue layers, vias, and the area of the radiator plate, etc. The HFSS model is then converted to DXF file and recruited in AutoCAD. Finally, the DXF file is converted to Gerber file by the software ASM500 and sent to fabrication.

1.3 Required specification

There are some well-known basic constraints of the printed antenna such as cost savings, low profile and light weight. These general requirements should be taken into account at the first place. Besides, the RF electronic specifications are the key criteria to judge the performance of the antenna. The required specification of the Receiver smart antenna array is given in [2]. Here we conclude it in Table 1.

Table 1: Design requirement for the receiver radiator

Parameter	Value
Downlink frequency	19.7- 20.2 GHz
Polarization	Circular (LHCP)
Antenna Gain	5 dB (for the array 35 dB)
Radiation pattern beamwidth (at –3dB) for the array	Approx. 5°
Side lobes level	< -20 dB
Axial Ratio	< 3 dB
Maximum scan angle	60°

For the single element design, the numerical specification can not reach the goals well as shown in Table 1, such as antenna gain of 35 dB and 3 dB beamwidth of about 5°. However, the abilities of the antenna array will be greatly enhanced after the digital beam-forming (DBF).

2 Background theories

2.1 Axial ratio and return loss [3]

The polarization ellipse is the curve which the peak of the E-field describes when the time varies in a plane normal to the propagation direction of the wave. The ellipse can be characterized by its maximum and minimum field values, $|E_{\max}|$ and $|E_{\min}|$, respectively. The axial ratio of the ellipse is defined by

$$(AR)_{dB} = 10\log\left|\frac{E_{\max}}{E_{\min}}\right|^2 dB \qquad (2.1.1)$$

For a desired circular polarization the axial ratio AR in dB and the amplitudes of the co- and cross-polar fields are related by

$$(AR)_{dB} = 10\log\left[\frac{|E_{co}|+|E_{xp}|}{|E_{co}|-|E_{xp}|}\right]^2 dB \qquad (2.1.2)$$

For an ideally circularly polarized wave the axial ratio is unity (0dB). The axial ratio is infinity for an ideally linearly polarized wave. Usually, the axial ratio no larger than 3dB in the working frequency band can be seen as a good circular polarization.

2.2 Circular polarization

The main parameters needed to evaluate an antenna's performance include radiation pattern, gain, impedance, and polarization. Polarization describes the vector nature of the radiated electric field. In [3], Per-Simon gives practical illustration of circular polarization. When the electric field vector oscillates along a line, it is called linear polarization. However, the plane wave's E-field can also rotate an angle 2π in the xy-plane when the time passes through a period T.

Then we can simply define right-hand circular (RHC) polarization for waves propagating in the z-direction by the unit vector

$$\hat{co} = (\hat{x} - j\hat{y})/\sqrt{2} \qquad (2.2.1)$$

which means that the y-component has a phase factor $-j = e^{-j\pi/2}$ compared to the x-component. In other words, the y-component of the field should have the same amplitude as x-component, but with $90°$ phase delay. Figure 1 illustrates the E-field factors or linear and RHC circular polarizations.

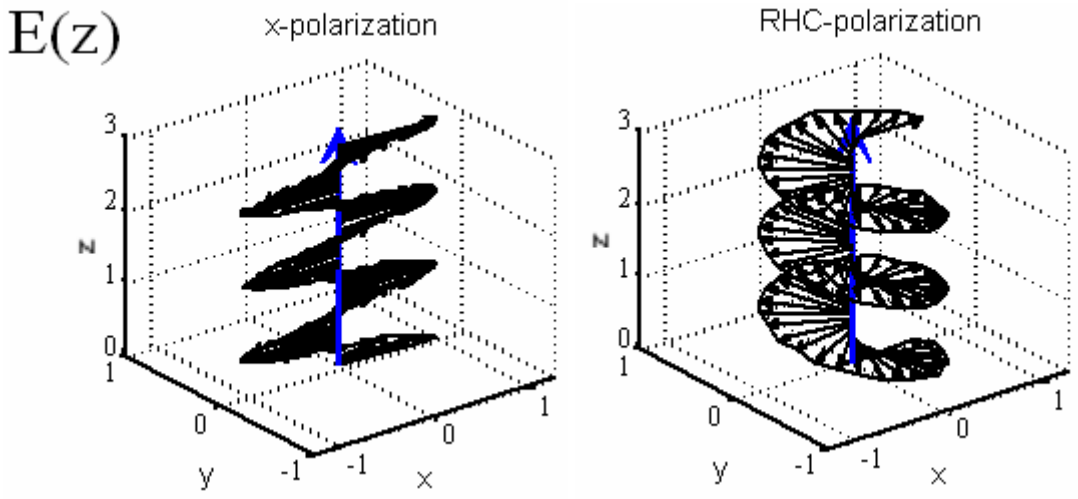

Figure 1: Comparison the E-field vector for linear and RHC circular polarizations [3]

It can be concluded that circularly polarized waves can be produced when two orthogonal linear polarizations with $90°$ phase difference and equal amplitude are excited. Various printed antennas are capable of satisfying these requirements. They can be classified as resonator and traveling-wave types. The traveling-wave type of antenna is usually constructed from a microstrip transmission line, which generates circular polarization by radiating orthogonal field components with appropriate phases along discontinuities in the traveling-wave line. A microstrip antenna is a resonator-type antenna. It is usually designed for single-mode operation that radiates mainly linear polarization. For a circularly polarized radiation, a patch must support orthogonal fields of equal amplitude but in-phase quadrature. These requirements can be accomplished by a single patch with proper excitations or by an array of patches with an appropriate arrangement and phasing [4]. For an array to generate or receive circular polarized signal, usually each single element of it is required to be circularly polarized. Although a circularly polarized (CP) array can be composed of linear polarized (LP) elements by geometrical position arrangement and digital beam forming of the feeding network. For example, sequential rotation with linear elements repeated rotation of sub-arrays [1]. However, this reduces the radiation efficiency. In order to improve the performance of the antenna array, the circularly polarized radiator is better to be used as the element than the linearly polarized radiator. The techniques for a single microstrip patch to generate CP are presented in Chapter 4.5 Nearly square truncated-corner patch.

For the receiver antenna, polarization must be matched to the orientation of the radiated field to receive the maximum field intensity of the EM wave. For the linear polarized antenna, the orientation is very important. If not oriented properly, a portion of the signal is lost. For the circular polarized antenna, the axial ratio is a key factor to scale the ability of transmitting or receiving a circular polarized wave. If the transmitting antenna uses right-hand circular polarization (LHCP), then generally the receiving antenna should also use LHCP to receive the signal.

2.3 Microstrip patch antenna

Basically, a microstrip patch antenna consists of a radiating patch on one side of a dielectric substrate and a ground plane on the other side as shown in Figure 2. The patch is generally made of conducting material such as copper or gold and can take any possible shape. The radiating patch and the feedline can be photo etched on the dielectric substrate. The geometry of the patch is usually square, rectangular, circular, triangular, or truncated-corner rectangular as which is used in this design.

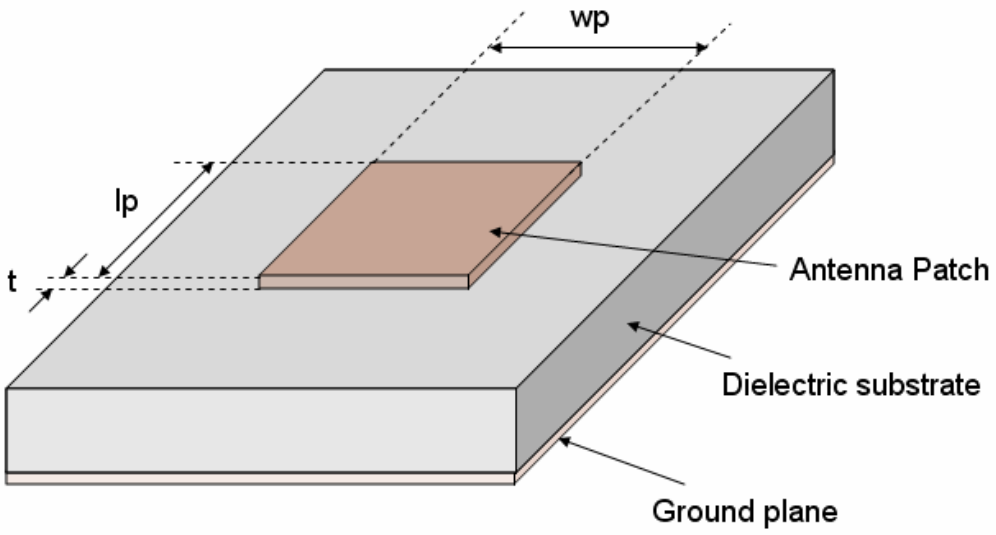

Figure 2: Structure of Microstrip patch antenna

Microstrip patch antennas radiate mainly from the fringing fields between the patch edge and the ground plane. Generally speaking, a thick dielectric substrate with a low dielectric constant provides better efficiency, larger bandwidth and better radiation efficiency [5]. However, usually such a configuration leads to a larger antenna patch size, which is a disadvantage when designing an antenna array. While higher dielectric constant substrate material gives less efficient and narrower bandwidth, it can reduce the size of the patch. Hence, a compromise should be reached between the antenna patch dimensions and the antenna performance. Also, selecting an appropriate feed technique can help to balance between the substrate dielectric constant and the bandwidth, for example, coplanar waveguide (CPW) feed can operate well on the high dielectric constant substrate and at the same time gives broader bandwidth than the microstrip feedline, which is presented in Chapter 3.4 and Chapter 5.1.

As a popular technique in wireless applications, microstrip patch antennas have many advantages, such as low-profile structure, low weight and fabrication cost, easily integration, capable of dual and triple frequency operations, etc. However, microstrip patch antennas also have some drawbacks, for example the narrow bandwidth, low efficiency, low gain, radiation losses, discontinuities from the junctions, and surface wave excitation. Microstrip patch antennas have a very high antenna quality factor (Q), which represents the losses associated with the antenna [ ]. Then it is understandable that a large Q leads to narrow bandwidth and low efficiency. Q can be reduced by increasing the thickness of the substrate. But as the thickness increases, and increasing fraction of the total power delivered by the source goes into a surface wave. This surface wave contribution can be counted as an unwanted power loss since it is ultimately scattered at the dielectric bends and causes degradation for the antenna characteristics. Through observing to the near field of the radiator, this surface wave phenomenon particularly stands out when using the CPW feed, which is presented in Chapter 5.5.

3 Microstrip antenna feeding strategies

3.1 Probe feed

There are several techniques to feed a microstrip antenna patch, such as coaxial feed, microstrip feed, coplanar waveguide feed. The coaxial feed shown in Figure 3 is also called probe feed. With this type of feeding technique, it is easy to adjust input impedance by selecting feed pint positions. As the frequency increases to tens of Giga Hertz, the positions of the feeding point could be extremely sensitive, thus the tolerance of fabrication becomes bad. This brings many difficulties in manufacturing for large size array.

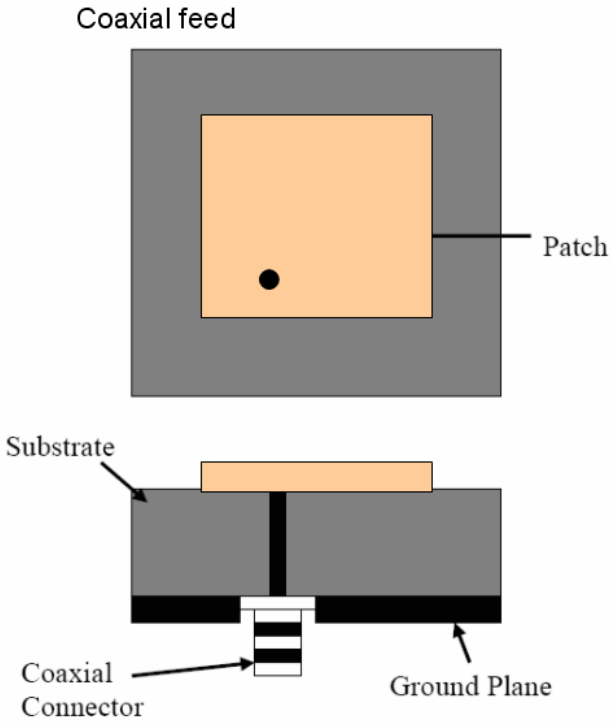

Figure 3: Coaxial fed antenna

For circular patch, probe feed is the most usual case. In this project, rectangular patch is chosen as the radiator patch. Thus, the feeding strategies for the rectangular patch are discussed specifically.

3.2 Coplanar feeding techniques

For rectangular patch, the microstrip feeds can be coplanar and non-coplanar feed. Coplanar feeds include direct edge feed (Figure 4 (a)), non-radiating edge feed (Figure 4 (b)), inset feed (Figure 4 (c)), and gap coupling (Figure 4 (d)).

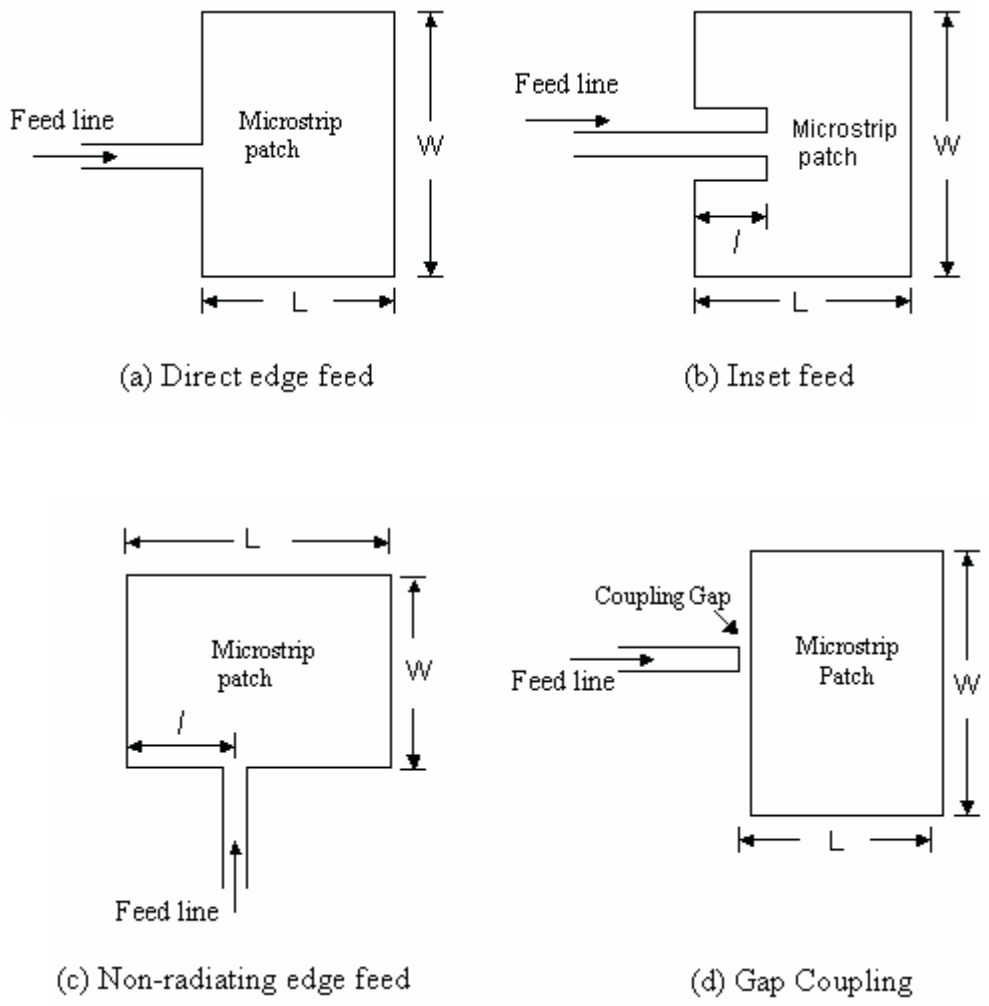

Figure 4: Microstrip feeds and their equivalent circuits

Case a, the direct edge feed is the most direct way to transmit the energy from the microstrip feed line to the patch. By using this type of feed, the feed network can be placed closer to the ground plane, resulting in reduction of radiation from various transmission line discontinuities. At the same time, the patch ground spacing can be increased to obtain greater bandwidth. However, it is difficult to achieve impedance matching by this means. Even if good matching is obtained, it would be very sensitive to the position of the feeding point. This calls low fabrication tolerance.

Compared to the direct edge feed wit**h Case b t**he inset feed, it is easier to achieve the impedance matching, but gives worse radiation pattern, due to its irregular geometry figure. Similar to the inset feed, the non-radiating edge feed (**Case c)** can also give easy impedance matching, but its radiation pattern is asymmetrical.

Generally speaking, for direct contact feeds, the best impedance match is obtained when the contact point is off-centered. This produces asymmetries in the excitation, which introduce

higher order modes. These higher order modes induce a cross-polarized component in the principal plane antenna patterns, which draw power from the dominant mode TM_{010} and results in degradation of the antenna's main beam.

Due to these drawbacks of the direct feeds, some non-contacting feeding techniques are introduced. **Case d** is a type of gap coupling coplanar feeding technique. However, this feeding technique is limited by many disadvantages factors, such as difficult coupling and extremely narrow gap. Even though it can achieve better impedance matching than the direct feeding, it is seldom used in the microstrip antenna design.

3.3 Non-coplanar feeding techniques

In the former chapter, several coplanar feeding techniques are introduced. The coplanar feeding microstrip antennas are easy to fabricate, and usually have fewer layers than the non-coplanar feeding antennas. However, the undesired radiation from the feed lines will bring some cross-polarization element. It may reduce the polarization purity and increase the sidelobe level [7]. In this project, when design the distances between adjacent elements, taking into account both mutual coupling and grating lobes effects, the distance between the adjacent element is chosen to be $\lambda/2$. This also causes some limitation of using coplanar feeding.

Thus, non-coplanar feeding is preferred. Non-coplanar feeding needs at least two substrate layers. Even though this increases the manufacturing costs, it is still widely used because of the benefits that multilayer structure brings. Fist, the non-coplanar feeding gives better bandwidth; second, the ground plane of the feeding line can also act as a shielding ground which can attribute the unidirectional radiation. The most popular non-coplanar microstrip feeding techniques are the proximity-coupled feeds (Figure 5) and aperture-coupled microstrip feeds (Figure 6).

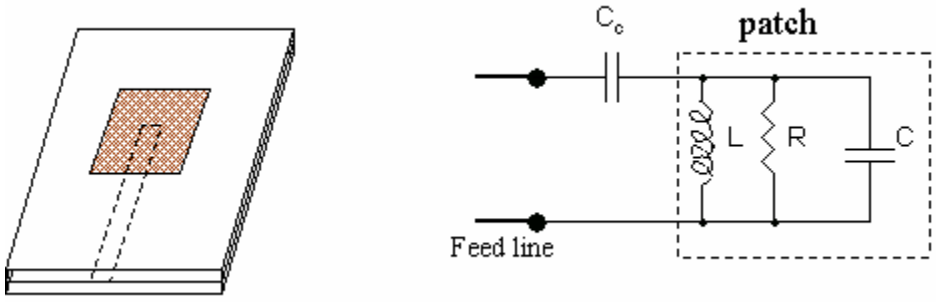

Figure 5: Proximity coupled microstrip antenna and its equivalent circuit

Figure 5 shows a proximity coupled microstrip antenna. In this structure, the behavior of the antenna patch can be equal to a RLC parallel circuit, the power is capacitive coupled from the microstrip line. Beside all the advantages above, the drawback is the spurious radiation from the feed. To reduce the spurious radiation from the feed, an aperture coupled structure as Figure 6 is introduced.

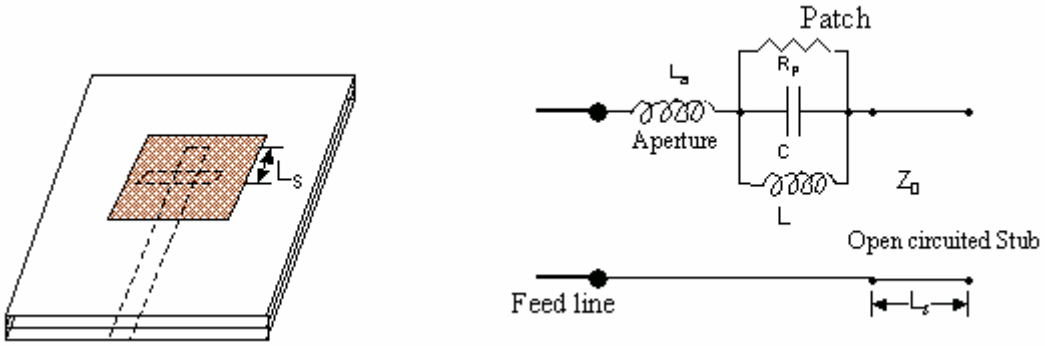

Figure 6: Aperture-coupled microstrip feed antenna and its equivalent circuit

The aperture coupled feeding technique demands two or three layers. The ground with slot separates the radiating patch and the microstrip feed line. Coupling between the patch and the feed line is made through magnetic field coupling of the slot. Unlike the co-axial feeding and the coplanar feeding, in which the patch natural frequency coincides with the resonant frequency of the whole structure, the patch and the aperture have their own resonant frequencies respectively. The resonant frequency of the whole structure (f_r) relates to the resonant frequency of the patch (f_p) and the resonant frequency of the aperture (f_{ap}) in a complicated way. This is presented in detail in Chapter 4.3 (Cavity model analysis).

The coupling aperture is usually centered under the patch, leading to lower cross polarization due to symmetry of the configuration. The amount of coupling from the feed line to the patch is determined by the shape, size and location of the aperture. Coupling level is primarily determined by the length of the slot. The width of the slot affects the coupling level less than the slot length. The ratio of slot length to width is typically 1/10 [8].

The main advantage of this feeding technique is the reduction of spurious radiation from the feed. However, the layer structure becomes more complex. This reduces the efficiency of the antenna.

3.4 Coplanar waveguide feeding techniques

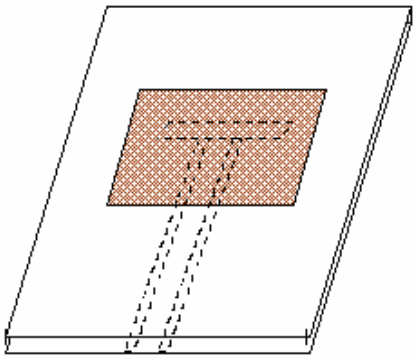

Figure 7: Coplanar Waveguide feed

Finally, a simple and economical feeding technique is introduced as shown in Figure 7. The CPW feed is preferred by many designers because of its single layer structure, low spurious radiation, and unidirectional radiation. As a feeding plan of this project, the coplanar waveguide feed is presented in detail in the following chapter.

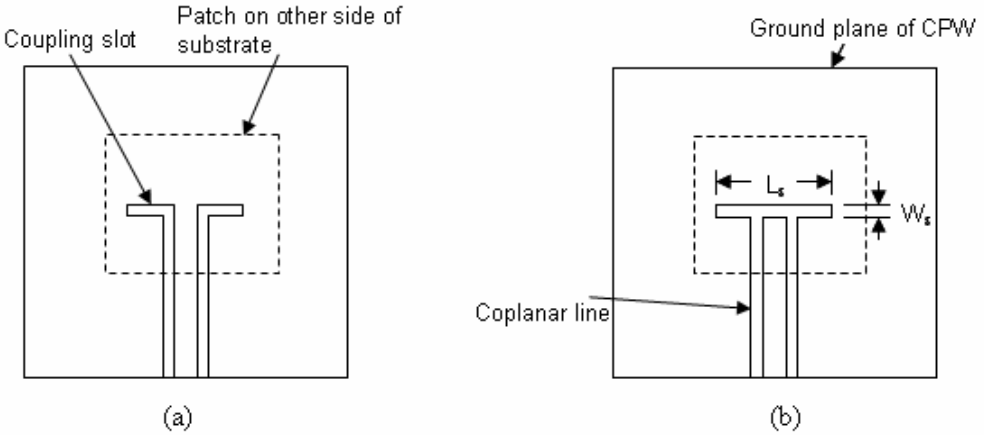

Figure 8: Coplanar waveguide feed of the microstrip patch antenna. (a) Inductive coupling by splitting the coupling slot into two halves by the CPW. (b) Capacitive coupling between the patch and the slot.

The CPW feed technique has many advantages especially for antenna arrays. For example, it has broader bandwidth than the microstrip feedline when operating on substrate with high dielectric constant. As shown in Figure 8, the inner conductor of a CPW feedline may connect to the rectangular coupling slot in an inductive (Figure 8 (a)) or capacitive (Figure 8 (b)) way. The inductive coupling CPW feedline ends with a short-circuited inner conductor, while the capacitive coupling ends with an open-circuited inner conductor.

In [9], some research on the inductively and capacitively coupled CPW-fed antenna at around 5GHz is presented. It is found that, the main difference between inductively and capaci-

tively coupled antennas is their different equivalent resonating circuits. The inductively coupled antennas are equivalent to strongly coupled parallel RLC resonators, so the slot length has a strong effect on the impedance locus, especially the real part of the input impedance. While the capacitively coupled antennas equivalent to series RLC circuit with a small and slowly varying real part. This means, when increasing the slot length of the capacitively coupled antennas, the impedance locus is hardly changed. Instead the loaded resonant frequency decreases. As a result, the S_{11} does not significantly depend on the slot length. Thus, practically, the inductively coupled antennas are more used in the real designs. In order to compensate the slots' inductive effects to the input impedance, a tuning stub is sometimes added to the short-circuited inner conductor of the CPW feedline as shown in Figure 9.

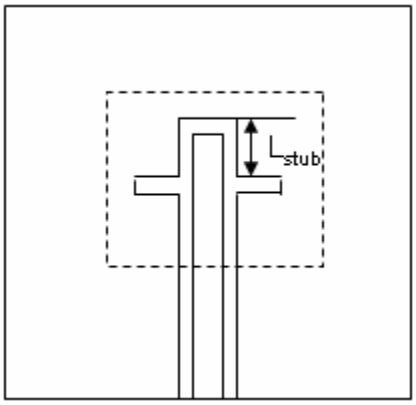

Figure 9: Inductively coupled slot with tuning stub

4 Aperture-coupled microstrip antenna design

The aperture coupled patch antennas have found widespread applications in communication systems during the last decade. The main advantage of using this type of antenna is the ability to use separate substrates for the feeding network and the patch itself. Figure 10 shows the geometry of the proposed aperture-coupled microstrip antenna, a truncated-corner patch is printed on the top substrate and excited by a non-resonant slot in the ground plane which is in turn excited by a microstrip line printed on a separate substrate covering the other side of the ground plane. This configuration reduces the surface wave effects on the patch antenna that the other feeding strategies especially CPW feed may have. Thus, it enhances its bandwidth. At the same time, it is isolating the feeding lines spurious radiation and leaves more space for the feeding network. This latter advantage makes it more suitable for the antenna array systems.

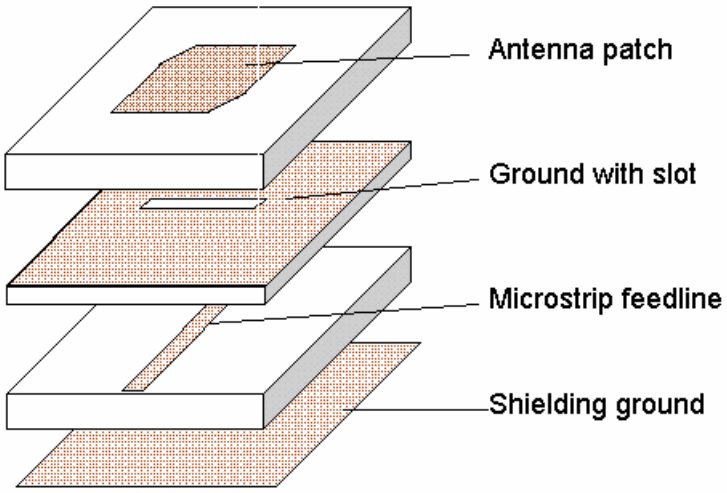

Figure 10: Layer structure of aperture-coupled antenna radiator (without transition)

4.1 Introduction to the design approach

There are two ways to design the circularly polarized aperture coupled microstrip antenna. One is to use two uncoupled apertures each one excited by a different feed line and each aperture provides in turn a separate linear polarization of the patch. Then, phase shifters or power dividers are needed to combine the signals from the two feed lines to get the desired circularly polarized signal. In this way, circularly polarized antenna arrays can be designed by using a complicated multilayer structure and feeding network.

In this project, an alternative method is adopted. At the beginning, an approximate model should be achieved by calculating the equivalent circuit. Then, this computed model is drawn in Ansoft Designer. This simulation software is based on Methods of Moment which is very efficient for the planar multilayer structure. Finally, the model is exported to Ansoft HFSS and optimized, which is based on 3D FEM.

Several models can be used when analyzing the radiating aperture, such as transmission line model and cavity model. In this project, cavity model is used to calculate the initial model of the antenna element.

4.2 Propagating modes analysis

An equivalent four-port circuit is used in analyzing the waves propagating in two parallel microstrip lines coupled by a rectangular slot in [7]. Since the antenna patch can be considered as a wide open-circuited microstrip line, the edges perpendicular to the feed line direction are the radiating edges. The shape of the aperture should be axial symmetrical along the feed line direction, such as crossing slot aperture and rectangular slot. Chapter 4.4 “Comparison of two types of coupling apertures” illustrates why the rectangular slot is chosen in this project.

The rectangular slot should be positioned parallel to these two radiating edges and exactly at the mid-distance position as shown in Figure 11, thus, the maximum coupling between the slot and the patch is achieved. Here, the slot can be equal to an incremental magnetic current source polarized in z direction [3]. Thus, for thin substrates, the dominant mode of the slot cavity is TM_{100}. (Note that, if the slot is along x direction, then the TM_{010} mode will be excited. In this cavity model, both TM_{100} and TM_{010} mode are considered which is presented in Chapter 4.3 (a)).

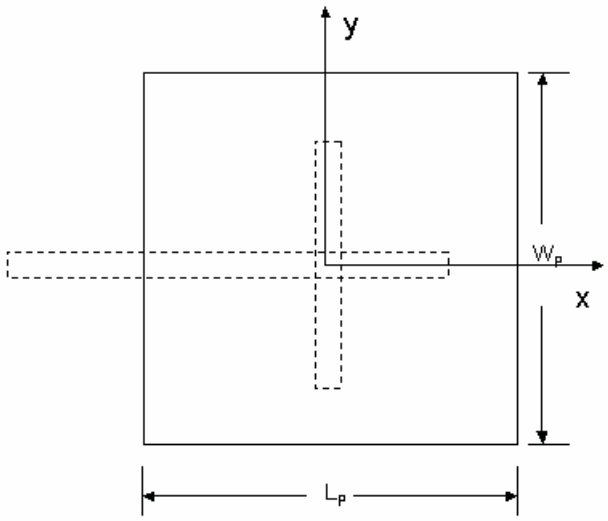

Figure 11: The rectangular slot positioned at x=0 (the mid-distance along the radiating edges)

Usually, a thin substrate of the aperture is preferred, thus, the computations only consider the dominant mode TM_{10}. This is a very important assumption of the cavity model. The width of the slot (w_s) should be small enough to be considered a small perturbation to the feedline fields where quasi-TEM waves propagate. Moreover, the slot should be long enough to avoid interact-tions between the feedline field and the slot edges. Thus, some useful limitations of the slot's dimension is drawn by [7] ,

$$l_{slot} \geq w_{line} + n \cdot d_{sub}, \quad \text{with } n \geq 6 \qquad (4.2.1)$$

where w_{line} is feedline width and d_{sub} is substrate thickness of the ground with slot. The ratio of slot length l_{slot} to its width w_{slot} is typically 10.

4.3 Simplified Cavity model analysis

The cavity model analysis is a classical analyzing approach of simple geometries, such as rectangular, circular and triangular patches. The introduction of perturbation segments will affect the cavity model field. Therefore, we make an approximation to the truncated-corner rectangular patch and ignore its truncated corners to avoid the complicated computation. With the help of the

simulation software, we do not need an exactly precise computation. A simplified cavity model analysis is sufficient for an evidential and solid starting point of design work.

The main purpose of using an equivalent model is to find out the total input impedance Z_{in} seen from the exciting port to the microstrip feed line. As explained in Chapter 4.2, the computations usually only consider the dominant mode TM_{100} and assume the rectangular slot on the ground plane as a magnetic current source.

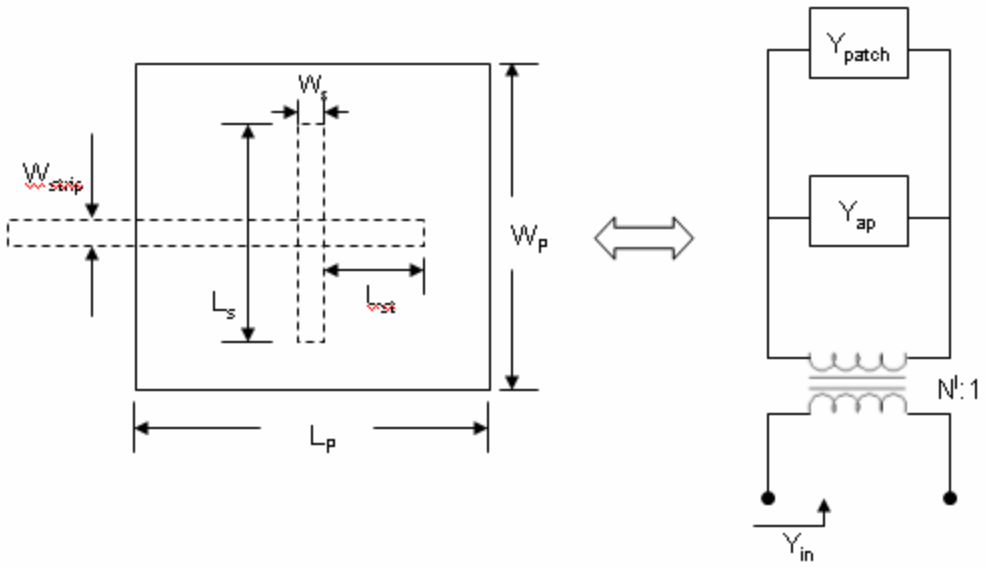

Figure 12: Aperture-coupled microstrip antenna and its equivalent circuit

Under the above premises, we make the equivalent circuit as shown in Figure 12 and analyze the cavity model by the following steps [10]:

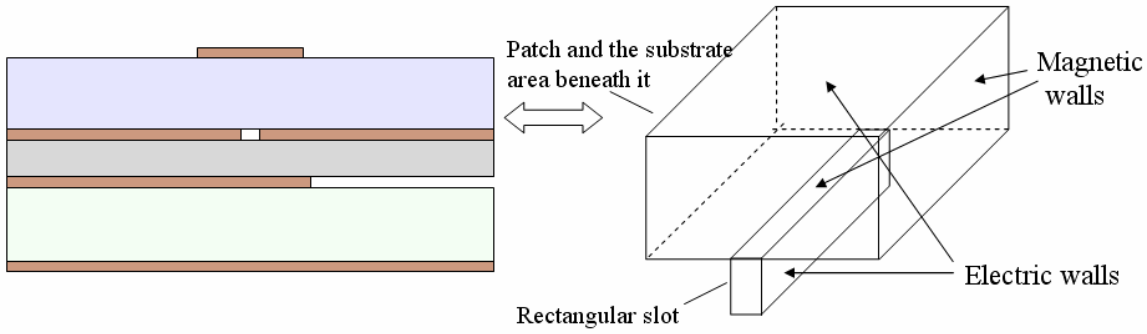

Figure 13: The aperture-coupled antenna's equivalent cavity model

a) The first step is to consider the microstrip antenna as a cavity, bounded by four "magnetic walls" around the edges of the patch, and two "electric walls" (See Fig. 13). The equivalent cavity is filled with a dielectric ε_{reff} . The resonant frequency of the patch is then[11]:

$$TM_{pq0}\,\text{mode:}\;\; f_p^{p,q} = \frac{c}{2\sqrt{\varepsilon_{reff}}}\sqrt{\left(\frac{p}{l_p}\right)^2 + \left(\frac{q}{w_p}\right)^2} \qquad (4.3.1)$$

When only dominant mode TM_{10} is considered, the resonant frequency of the patch is decided by the length of the patch l_p. This can be observed from Fig 20 (S_{11} values by different length of the patch) in the simulation results. Considering all the layers use the same type of substrate RT/duroid 5880 ($\varepsilon_r = 2.2$), then we can have a computational result of $l_p = 5.06\,\text{mm}$. After optimization to the structure in Ansoft HFSS, the optimized l_p has a length of 4.85mm, which is close to the computational result. The width of the patch w_p affects the resonant resistance of the patch: the larger w_p gives lower resistance. Let $l_p = w_p$, then the resonant frequencies of TM_{100} and TM_{010} modes become identical. Thus, dual linear polarization is desired. Furthermore, if some perturbation is added to the patch and makes the phase shift of these two linear polarizations, the CP can be generated. This is the reason why square patch is widely used in circular polarization and dual linear polarization. Practically, when taking into account the impedance matching, it is found that a nearly square patch has the better performance than a square patch after perturbation (see Chapter 4.5).

b) The second step is to take into account the thickness of the ground with slot, and consider the slot as a cavity ending upon two "magnetic walls" on the super and sub substrates (see Fig.13). In another word, the slot can be considered as a rectangular waveguide ending with two substrate materials. As the thickness of the metal ground is only 17 17, so the dominant resonant mode is TE_{100}. According to the equation of the cutoff frequency of rectangular waveguide, the resonant frequency of the slot can be calculated as [11]:

$$TE_{100}\,\text{mode:}\;\; f_s = \frac{c}{2l_s\sqrt{\varepsilon_{req}}} \qquad (4.3.2)$$

ε_{req} is the equivalent dielectric constant inside the slot, in [12] the approximate expression is,

$$\varepsilon_{req} \approx \frac{\left(\varepsilon_{r1} + \varepsilon_{r2}\right)}{2} \qquad (4.3.3)$$

In this project, the substrate of the patch, ground with slot and the microstrip feed line use the same substrate Rogers RT/duroid 5880. So we have $\varepsilon_{r1} = \varepsilon_{r2} = 2.2$.

c) In step (a) and (b), the resonant frequency of the patch f_p and that of the slot f_s have been related to the geometrical dimension of the patch and the slot. How to relate these two resonant frequencies to the resonant frequency of the whole structure f_{total} depends on the specific situations. For example, when f_p and f_s are close to each other, the bandwidth of the total structure is enhanced, but it may introduce strong parallel plate modes to the system (see Chapter 4.8 simulation results and analysis). Finally, f_{total} should be coincided with the operating frequency at Ka-band.

In some articles ([7], [13]), the patch is analyzed as a series resonant circuit or parallel resonant circuit (see Figure12). However, all these complicated equivalences are based on a simple assumption that only the dominant mode is considered. More general and precise model should take into account the higher-order modes. This can be simulated in HFSS. In step (a) and (b), let $f_p = f_0 = 19.95GHz$ (19.95GHz is the center frequency of the operating bandwidth.), the approximate dimension of the patch can be calculated.

From [14], some experimental results prove that, the non-resonant slot has less transmitssion loss than the resonant slot. It is found that, for the resonant slot, the amount of radiated power tends to increase with frequency, but the increase is less evident as the slot becomes shorter. As a consequence, the coupling is significantly improved by using a shorter slot, the resonant frequency of which is higher than the operating frequency. Hence we can setup the f_s several hundred mega Hz higher than f_p. In this way, the length of the slot l_s can be estimated, and the width of the slot w_s usually is $1/10 l_s$ [8]. Then setup this model in HFSS, analyze the simulation result and tuning the parameters, these procedures are presented in Chapter 4.8 Simulation result analysis. Thus, the cavity model analysis is simplified under the assumption of the patch's resonant frequency is the same as the central frequency of the operating bandwidth, associated with the parametric simulations in Ansoft HFSS, good simulation results can be quickly achieved.

4.4 Comparison of two types of coupling apertures

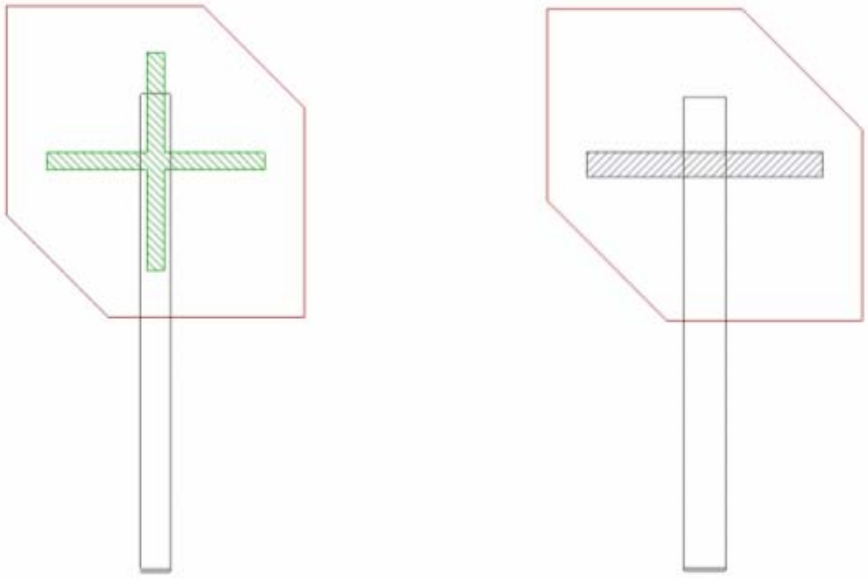

Figure 14: Crossing-slot coupled Microstrip line feeding patch structure

A common technique for producing circular polarization is to excite two orthogonal linearly polarized elements wit a 90°phase difference. This method can be utilized in the aperture-coupled antenna by using a crossing slot as shown in Figure 14. The modes excited in different edges of the patch are presented in Chapter 4.2. The slot along x-direction, in which lies the microstrip feedline, mainly excites TM_{01} mode. Because it is in the same direction as the feedline, the energy is poorly coupled to the slot. When designing the dimensions of the antenna, it is more efficient when using fewer variables. The main purpose of having a crossing-slot is to excite two modes in perpendicular directions. This can also be done by nearly square patch, which is introduced in Chapter 4.5. Moreover, since the insertion loss of a microstrip array is mostly incurred in the power distribution transmission lines, the length and complexity of these lines should be minimized. As a result, the single-slot feed patch is selected as the element of the array.

4.5 Truncated-corner nearly square patch

There are basically two techniques for a single microstrip patch to generate circular polarization (CP) as shown in. One is to have a square or circular patch excited by two orthogonally located feeds with 90°phase difference. The other is to have a physically perturbed patch excited by a single-slot feed.

Popular perturbation configurations are truncated-corner patches. As illustrated in Fig 15, they operate on the same principle of detuning degenerate modes of a symmetrical patch by perturbation segments [4]. .

The excitation source of the patch is a rectangular slot, which is centrally beneath it. As we analyzed in Chapter 4.3, the TE_{100} mode propagated in the slot cavity will excite TM_{100} and TM_{010} mode in two orthogonal directions, when the patch has a rectangular geometric. After it is truncated with two diagonal corners, the fields underneath the patch are perturbed by the small truncations. The perturbation splits the field into two orthogonal modes (as shown in Figure 15, mode 1 and mode 2) with quadrature phases. The mode 1 and mode 2 (Fig 15) can be seen as being synthesized from mode TM_{100} and TM_{010}'s components along the diagonals. The perturbation contributes the phase shift of the two modes. When the amount of perturbation causes two orthogonally polarized fields with equal amplitudes and $90°$ phase different, CP can be radiated. The CP level can be adjusted by tuning the depth of truncation.

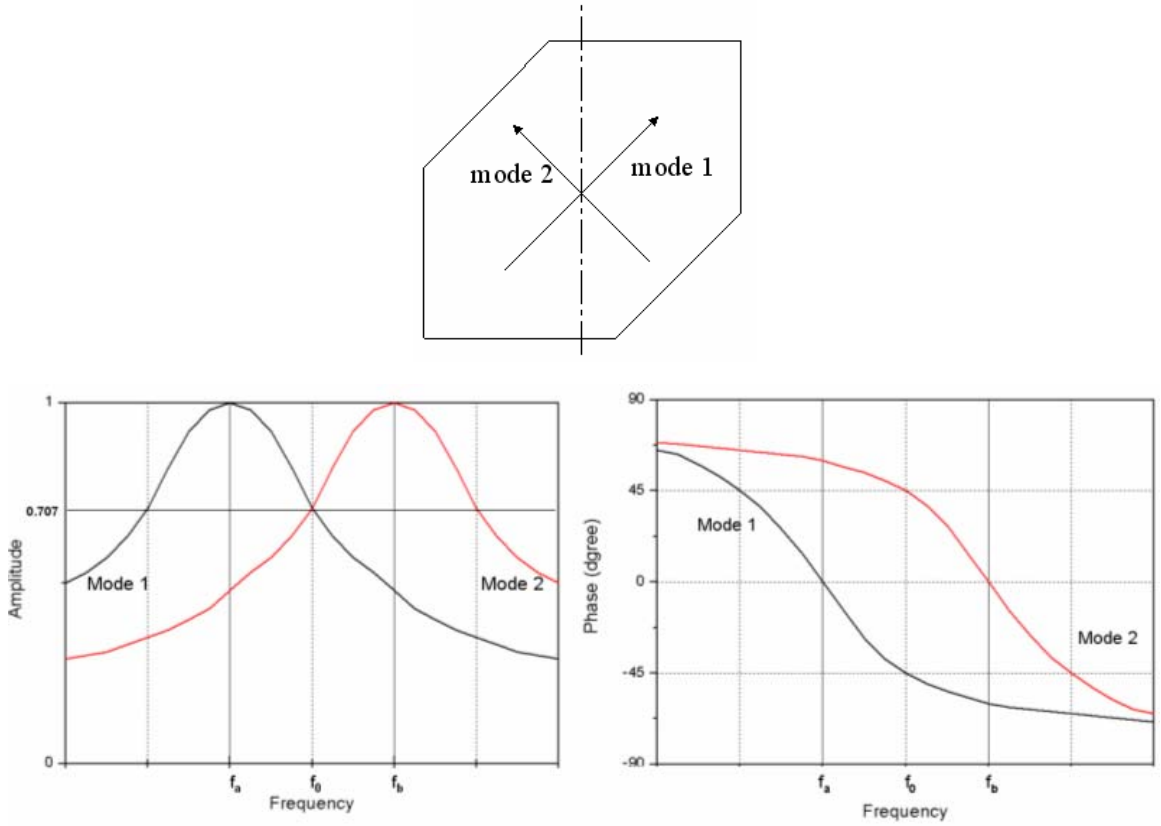

Figure 15: Amplitude and phase of orthogonal modes for singly fed circularly polarized microstrip antennas.

Usually, a square patch is perturbed to generate CP. Through some tests and comparison, a nearly square patch turns out to have better performance than the former one. It is presented in Chapter 4.3, the resonant frequency is decided by the length of the patch (l_p). While tuning the

width of the patch (w_p) can change the resonant resistance of the patch. When a square patch is used to excite CP, it is found that the good impedance matching and good axial ratio can not be achieved at the same frequency. From Figure 16 and Figure 17, we can see that, for a truncated-corner nearly square patch resonating at 19.95 GHz, when changing w_p to the same value as l_p, the resonant frequency keeps the same. This proves the theoretical conclusion in Chapter 4.3 (a), the resonant frequency is decided by the length of the patch, and the width of the patch only influences the resonance impedance and the cross polarization level at the resonant frequency. Hence, by changing the w_p value (usually let w_p shorter than l_p), the bandwidth for low cross polarization level (also we can say low axial ratio level [3]) can be shifted to 19.95 GHz.

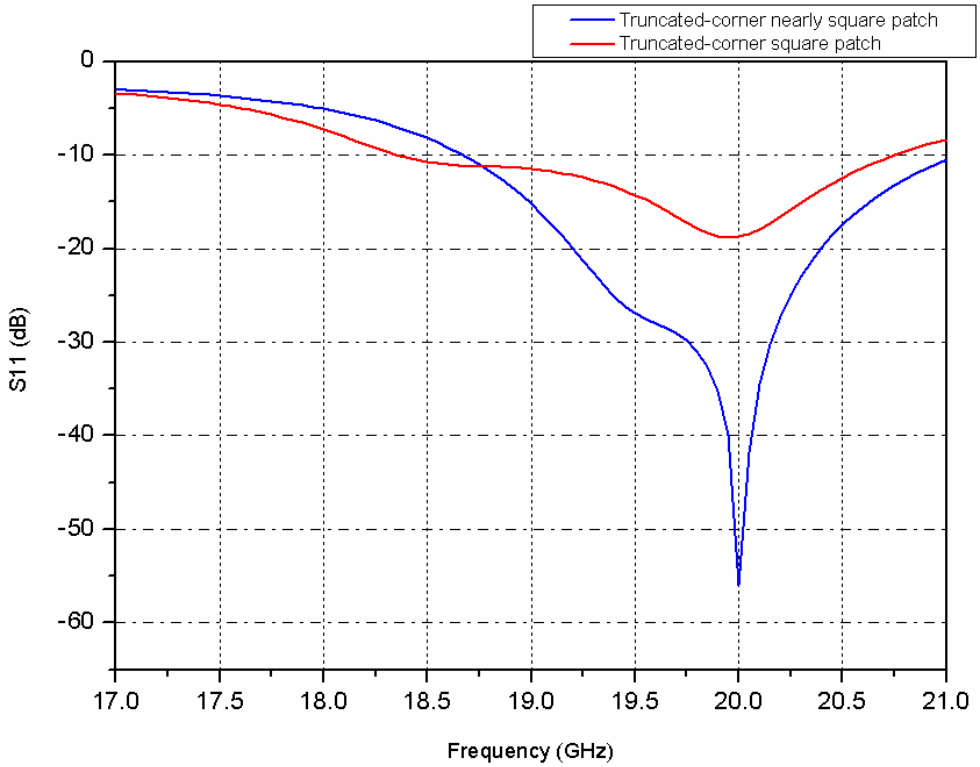

Figure 16: S_{11} curves of Truncated corner nearly square and square patch

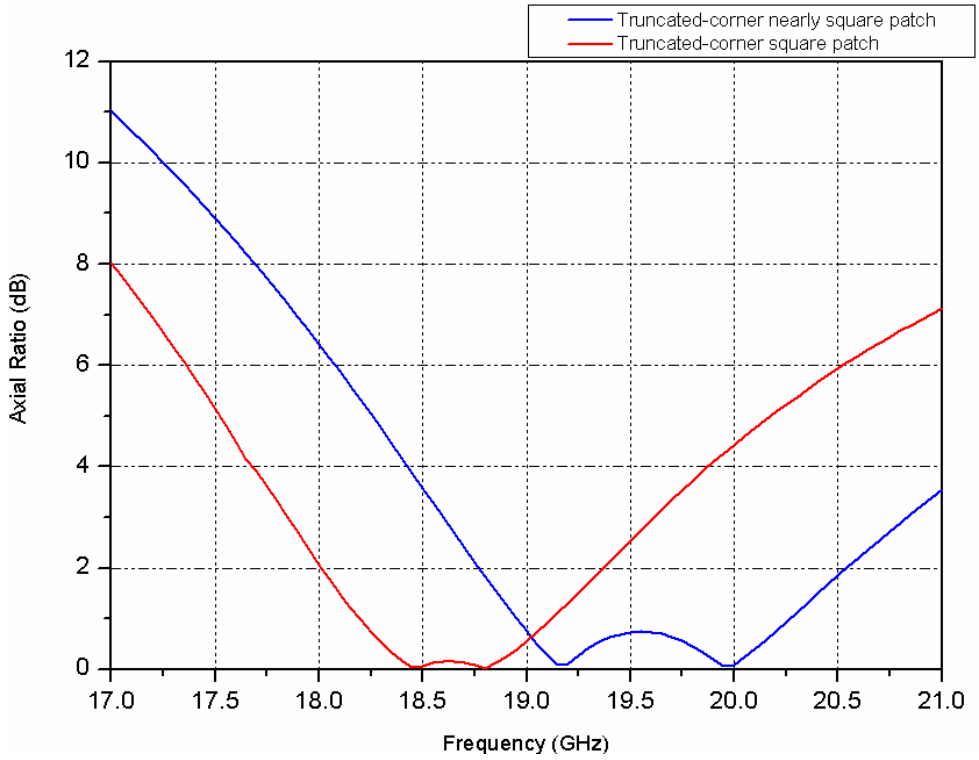

Figure 17: Axial Ratio curves of Truncated-corner nearly square and square patch

4.6 Designing approach on HFSS

In the early period of the designing, a 50 ohm microstrip feedline is used all the time. It is observed that, by using this feedline, the good impedance matching and axial ratio can not be achieved at the same time in the operating bandwidth. From the analysis in Chapter 4.2 and 4.3, we make an extrapolation. The reason for this phenomenon is because a strong coupling between the microstrip line and the rectangular slot makes the radiating at the two edges along x direction (see Figure 11) much stronger than the other two edges, then the axial ratio becomes very bad within this bandwidth. It is an instinctive behavior of this multi-coupled structure. If both of the impe-dance matching and good axial ratio are desired in the same bandwidth, a transformer should be used. The function of the transformer is to transform the low characteristic impedance feedline under the slot to a 50 ohm line which is connected to the excitation port. Thus, under the slot, a broader line can be used to reduce the coupling level to the slot. This is a trade off between the bandwidth and the coupling strength. When only 2.5% bandwidth is required, it is feasible to achieve this by losing some coupling.

The prototype of the transformer, which is used in this design, is a one-step –transformer. As a result of the $\lambda/2$ distance limitation between two adjacent radiators, the length of the microstrip feedline should be shorter than $\lambda/4$. Impedance matching can be achieved by tuning the length and width of the microstrip line transformer. Figure 18 shows a typical Smith chart plot of the impedance locus versus different widths of the microstrip line transformer. The width of

the microstrip line transformer influences the real part of the input impedance at the port. Moreover, the imaginary part of the input impedance can be adjusted by tuning the length of the microstrip line, which can be observed from Figure 19. When the length of the microstrip line slightly extends, the input impedance locus shifts from inductive area to capacitive area.

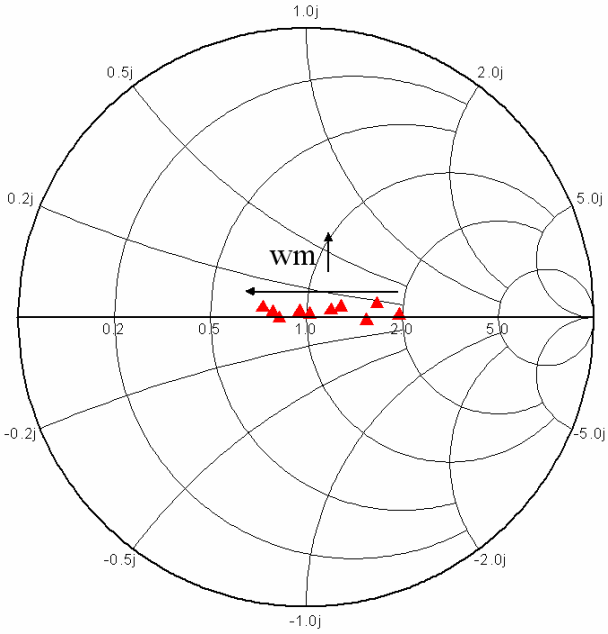

Figure 18: Smith chart plot of the impedance locus versus different widths of the microstrip line transformer

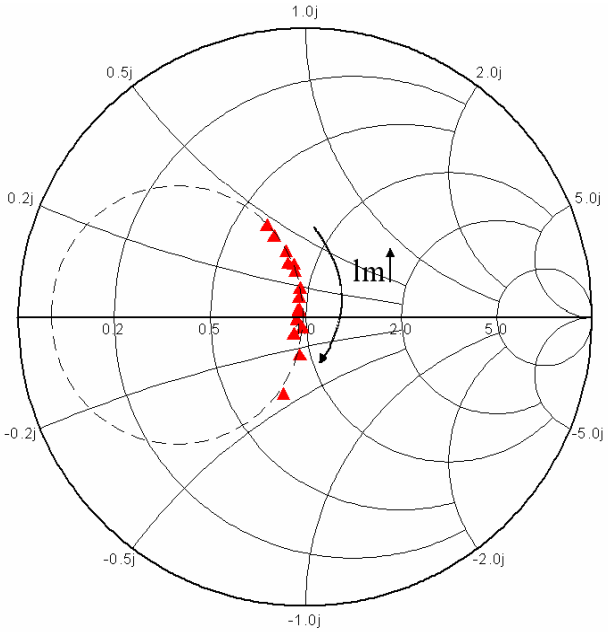

Figure 19: Smith chart plot of the impedance locus versus different lengths of the microstrip line transformer

Figure 20 shows the parametric study to the lengths of the patch (l_p). There is a clear tenden-cy that, when l_p increasing, the resonant frequency shift to the lower frequency. While the width of the patch (w_p) influences the resonance impedance, which can be seen from Figure 21. Figure 22 shows the S_{11} values by different slot lengths (l_s). It is noticed that, the length of the slot mainly affect the coupling level, but not the resonant frequency.

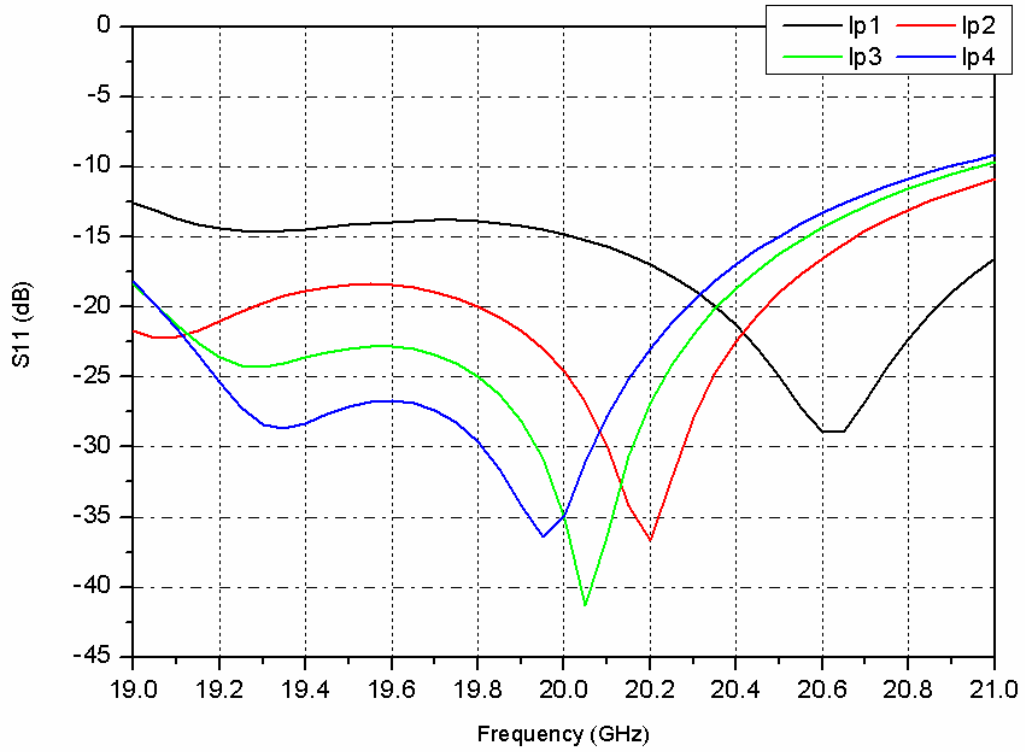

Figure 20: S_{11} values by different length of the patch, l_{p1}=4.6mm, l_{p2}=4. 7mm, l_{p3}=4.8mm, l_{p4}=4.85mm

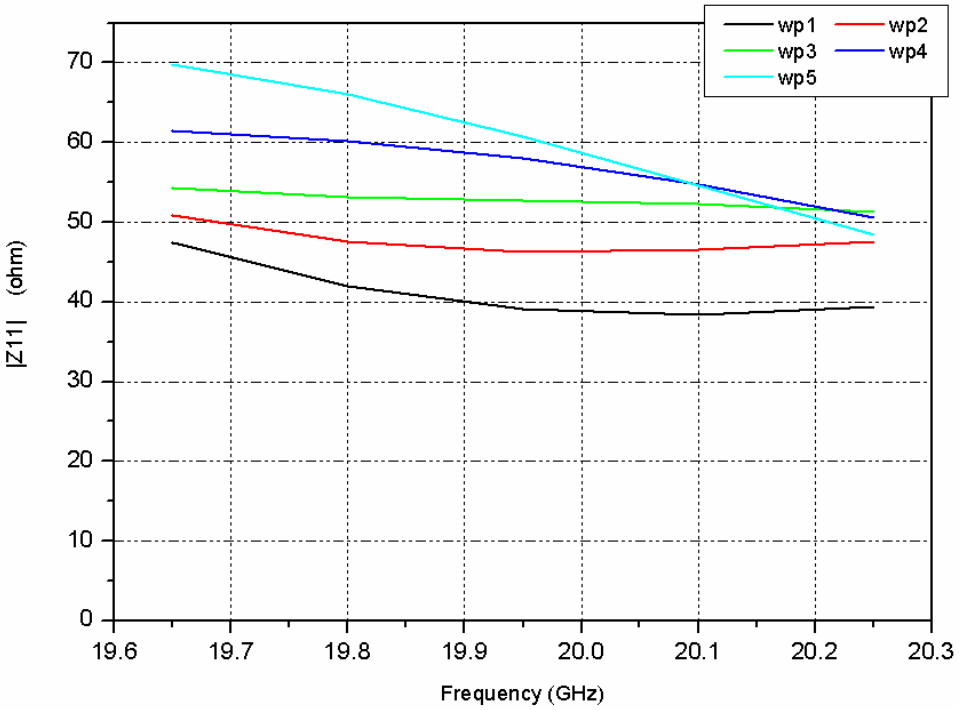

Figure 21: $|Z_{11}|$ values by different width of the patch, w_{p1} =4.29mm, w_{p2} =4. 39mm, w_{p3} =4.49mm, w_{p4} =4.59mm, w_{p5} =4.69mm

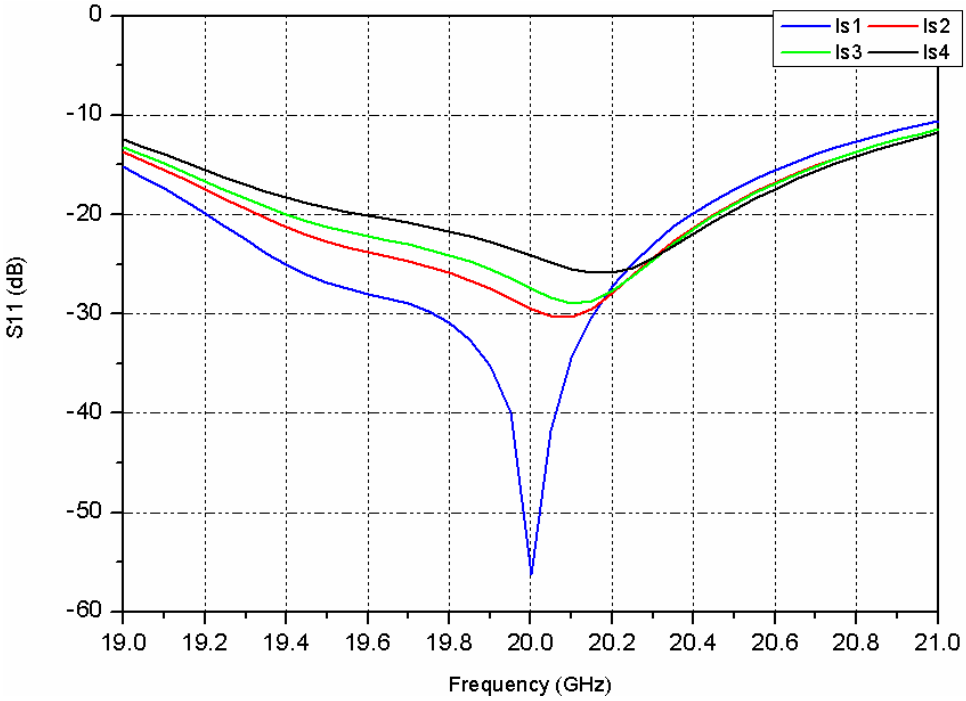

Figure 22: S_{11} values by different slot lengths, l_{s1} =4.14mm, l_{s2} =4. 44mm, l_{s3} =4.64mm, l_{s4} =4.84mm

4.7 The optimized configuration of aperture-coupled antenna

A summary of layer structure and the basic design parameters for the optimized single element are described in Figure 23 and Figure 24. One can control the size of the radiating patch (l_p, w_p) to tune the resonant frequency of the antenna and, up to certain degree, its return loss band-width. The slot position relative to the patch (in this design, the slot is positioned centrally beneath the patch), its length (l_s), and its width (w_s), along with the microstrip feedline stub length (L_{stub}) allow the control of the input impedance of the antenna (see Figure 20-Figure 22). Additionally, in the final optimized configuration, a tapered line is added at the joint of the two different widths of the microstrip feedline to reduce the higher-order modes effect.

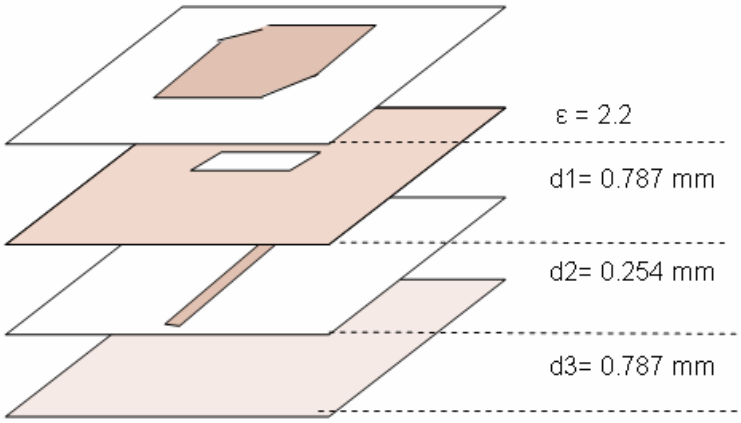

Figure 23: Layer structure of optimized aperture-coupled antenna

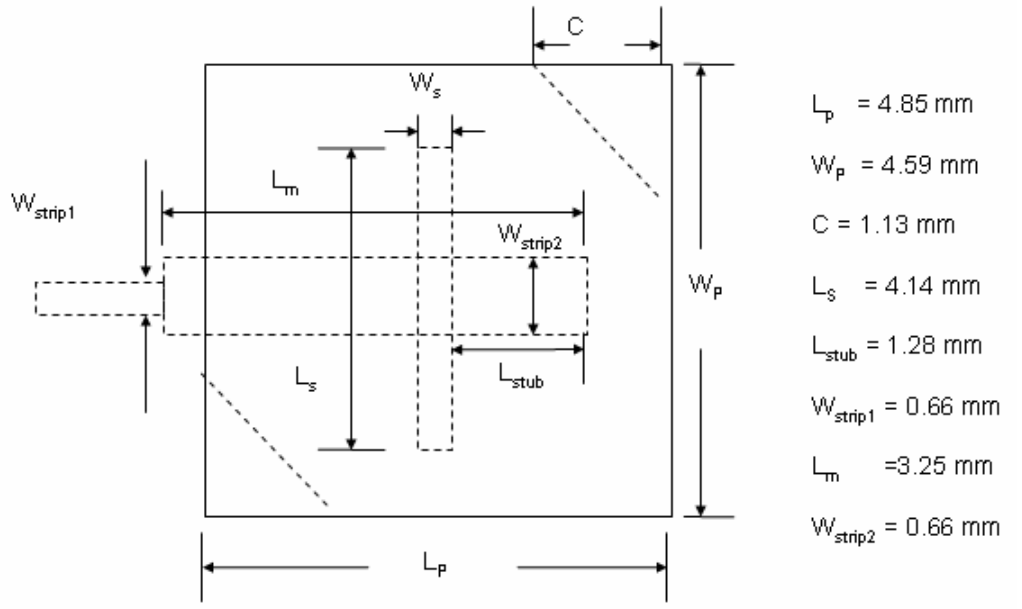

Figure 24: Schematic and dimensions of the optimized aperture-coupled antenna

Theoretically, it is better to use different substrates for each layer. For example, if strong coupling is demanded, then the dielectric constant of the patch better be larger than that of the slot; however, if more bandwidth is demanded, then one can try to reduce the dielectric constant of the patch to achieve more bandwidth by giving up some coupling power. For some realistic and economical considerations, in the design of antenna without transition via, all the layers use the same type of substrate RT/Duroid 5880 ($\varepsilon_r = 2.2$) with different thickness. In Chapter 4.3, we already have the computational value of $lp = 5.06mm$. By well selecting the thickness of the substrates, the optimized layer configuration is achieved as shown in Fig 20. One can reduce the size of the patch by using another substrate with higher dielectric constant, for example Rogers RO 4003 with the dielectric constant $\varepsilon_r = 3.38$.

Finally, a transition-VIA is added to the design above. This transition is used to coupling the energy from the MMIC active component circuit to the radiator. It can be seen as a "black box" to the radiator itself. Some adaptations need to be done on the antenna dimensions after adding the transition-VIA, but it is important to make these adaptations as few as possible, in order to make it comparable with the original antenna without transition. Furthermore, by comparing the antenna before and after adding the transition-VIA, the influences of the transition-VIA can be easily known.

4.8 Simulation result analysis

4.8.1 Without transition VIA

A summary of simulation results for the optimized aperture-coupled antenna without transition VIA is given in Fig 26-33. In order to make the simulation results more comparable to the measurement results, glue layers (Neltec FV 6700 $\varepsilon_r = 2.35$ with the thickness 0.038mm) are added to the model as shown in Figure 25.

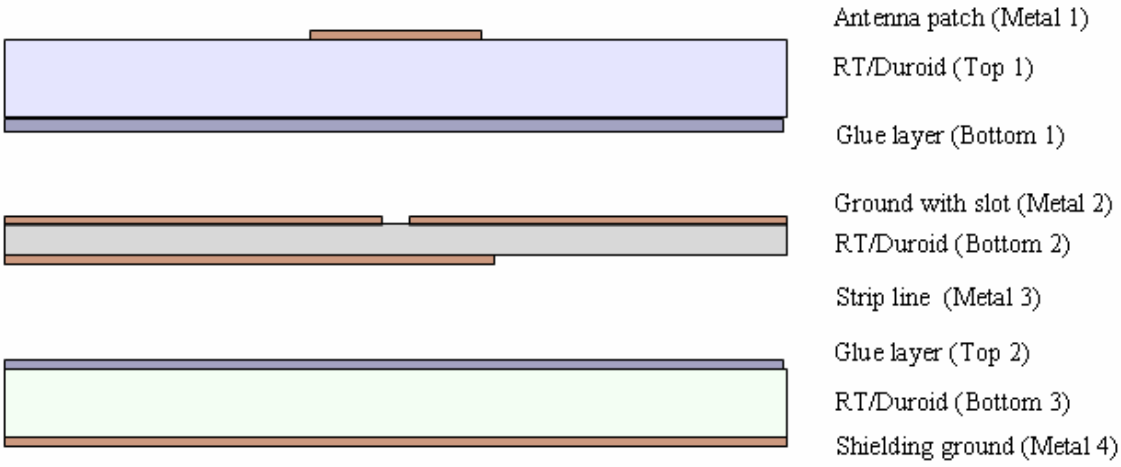

Figure 25: Layer structure for the optimized aperture-coupled antenna without transition

It is found that, in HFSS, the simulation results are different between defining an absorbing boundary of the radiation box and a radiation box which keeps a distance with the substrate boundaries. The radiation box using an absorbing boundary refers to the air box which contacts the boundary of the substrate material and the ground of the simulated structure using an infinite ground. All the presented simulation results are achieved by using an absorbing boundary of the radiation box. Figure 26 makes a comparison of the simulated return losses for the radiation box using and not using an absorbing boundary. It can be seen that, on the return loss depth at the central frequency, when not using an absorbing boundary, the S_{11} level goes deeper.

First of all, the simulated S_{11} parameter for the antenna is shown in Figure 26. An obvious resonance can be noticed around 20 GHz with a -15 dB return loss bandwidth of more than 1 GHz. Within the whole operating bandwidth (19.7 GHz-20.2 GHz), the return loss is below -23 dB. Figure 27 shows a Smith chart plot of the antenna input impedance.

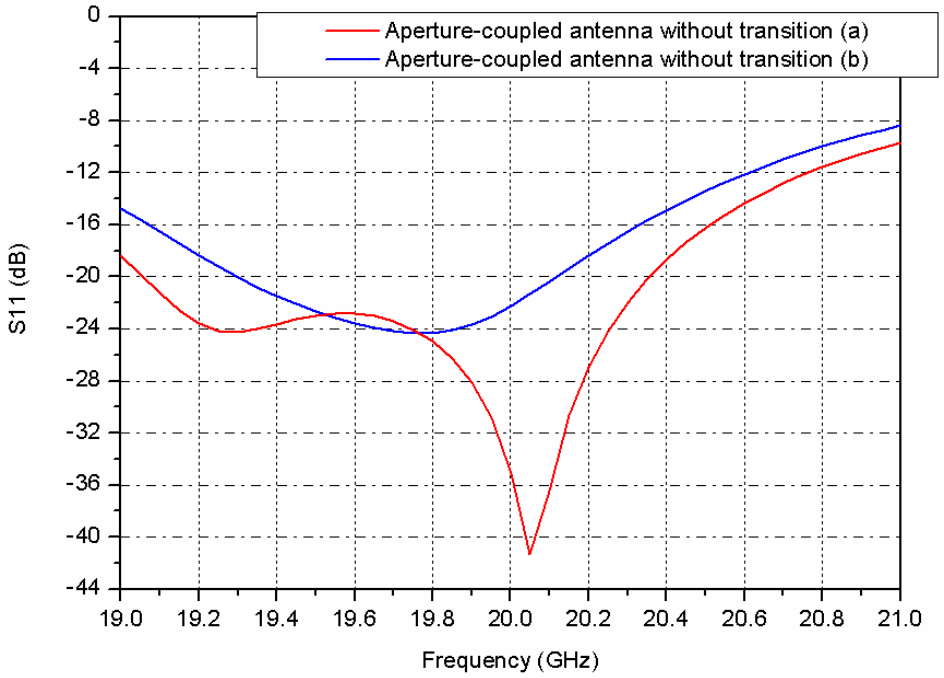

Figure 26: Comparison of S_{11} for the optimized aperture-coupled antenna without transition by two types of radiation boxes

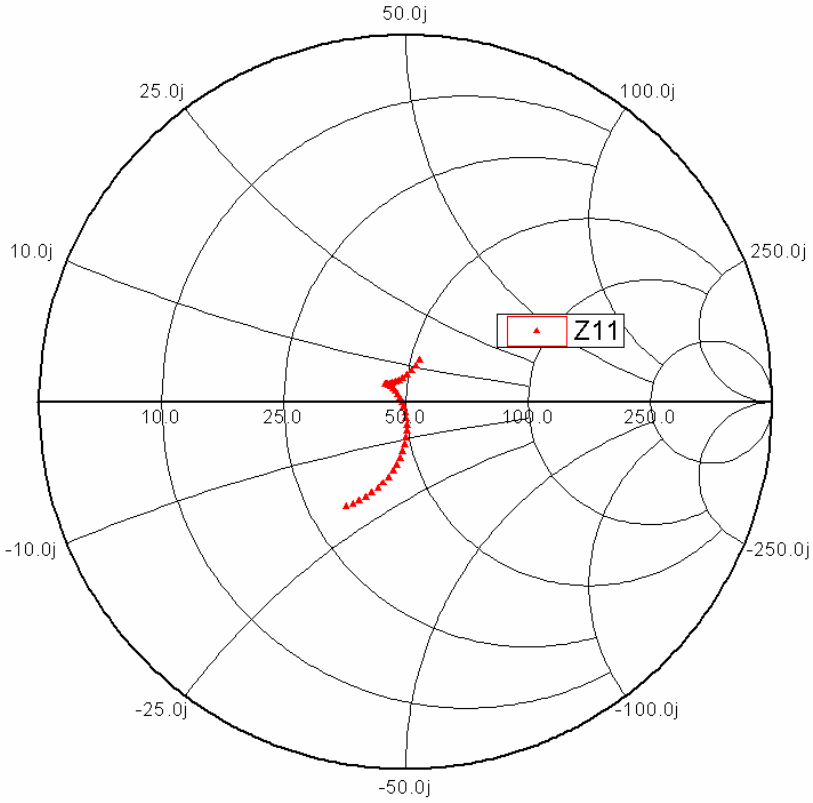

Figure 27: Smith chart plot for the input impedance of optimized aperture-coupled antenna without transition at 19 GHz-21 GHz

The realized gain represents for the antenna gain normalized by the input power. The LHCP realized gain of aperture-coupled antenna in E- and H- planes are shown in Figure 28. In both E- and H-planes, the realized gain in the main radiation direction is about 7 dB, with the 3dB beamwidth is about $75°$. The symmetry of the radiation patterns keep very good in both plane as a consequence of shielding between the microstrip feedline and the patch.

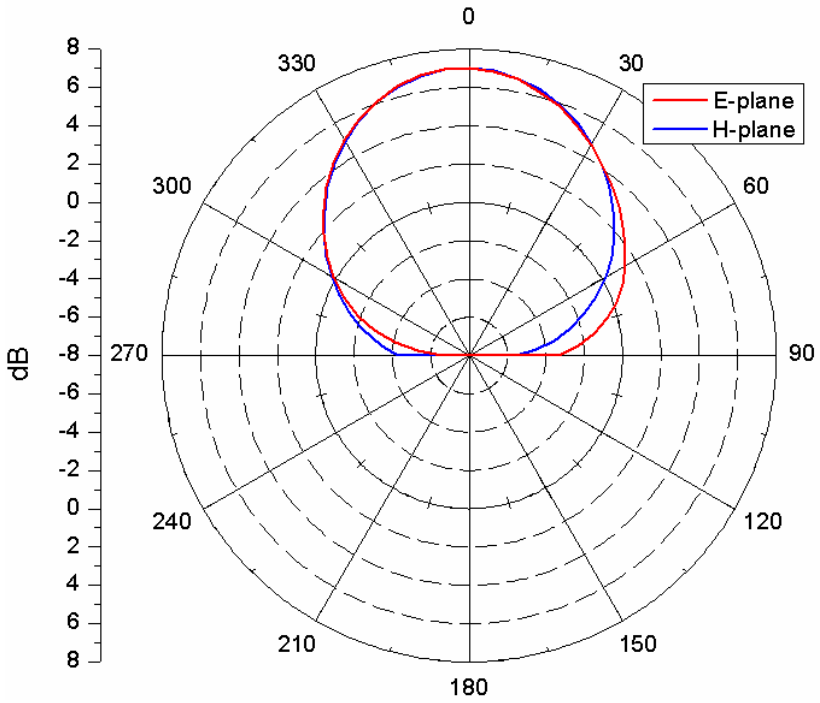

Figure 28: LCHP Gain of aperture-coupled antenna without transition in E- and H-planes at 19.95GHz

Figure 29 and Figure 30 present the realized gain for the left-hand-circular polarization (LHCP) and the right-hand-circular polarization (RHCP) in E- and H-plane respectively.

Figure 31 shows the axial ratio level from 19 GHz to 21 GHz. The axial ratio is nearly 0 dB at 19.95 GHz, and below 1dB in the operating bandwidth (19.7 GHz-20.2 GHz).

Figure 32 shows the axial ratio in E- and H-planes at the central frequency 19.95 GHz. In E-pane, there is nearly $200°$ beamwidth that the axial ratio is below 3 dB. In H-plane, $180°$ beamwidth is observed for the axial ratio below 3 dB. Slight asymmetry is found in both planes' axial ratio level. This is probably due to the perturbation configuration of the patch.

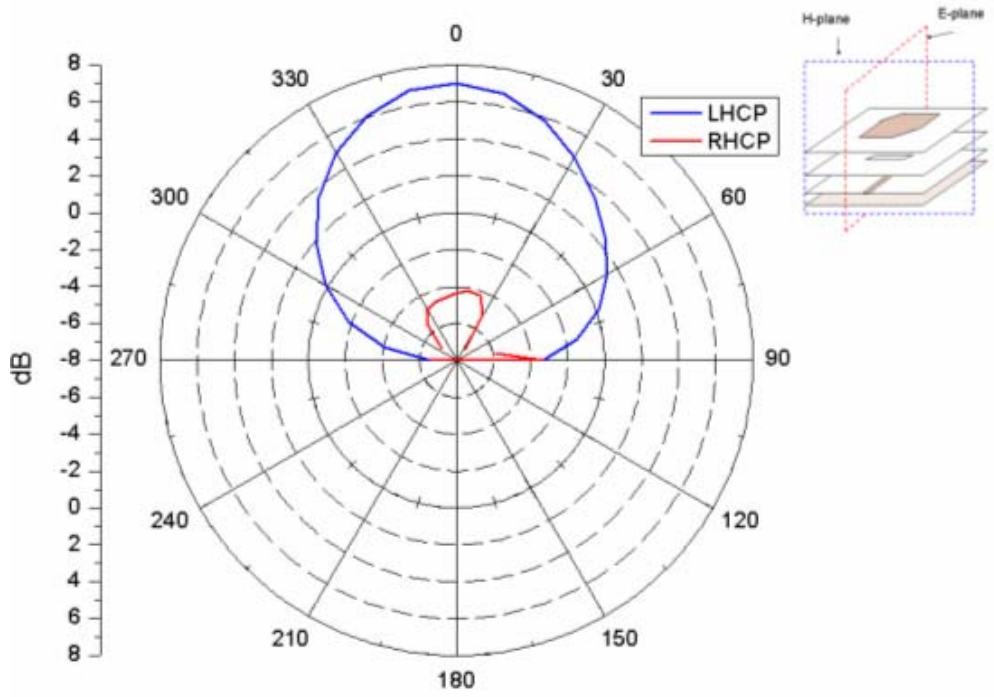

Figure 29: Realized gain for LHCP and RHCP in E-plane for the aperture-coupled antenna without transition

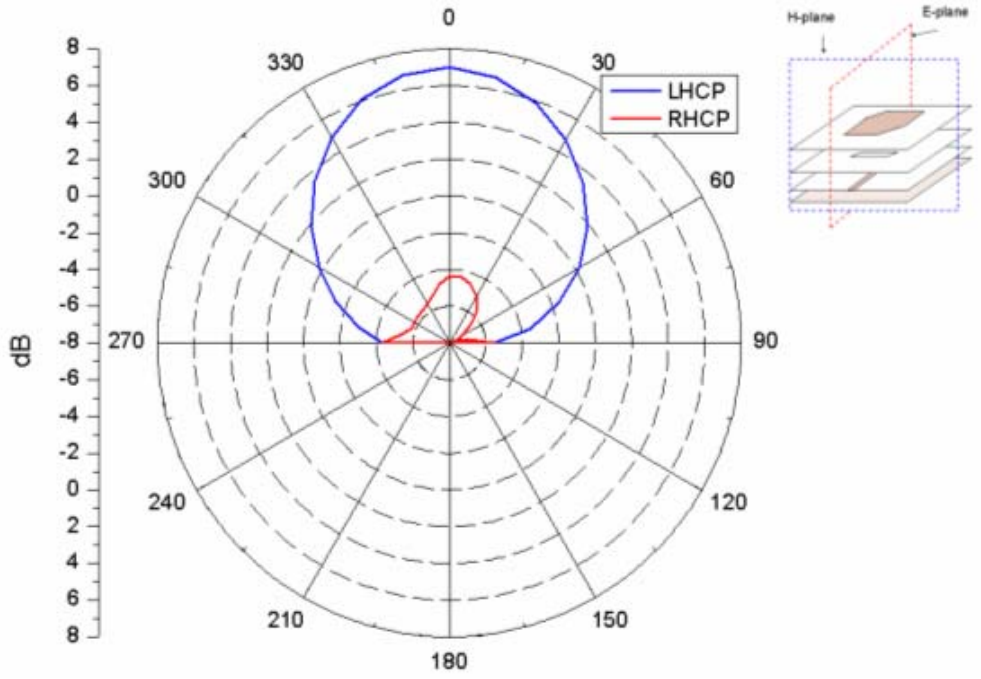

Figure 30: rE for LHCP and RHCP in H-plane for the aperture-coupled antenna without transition

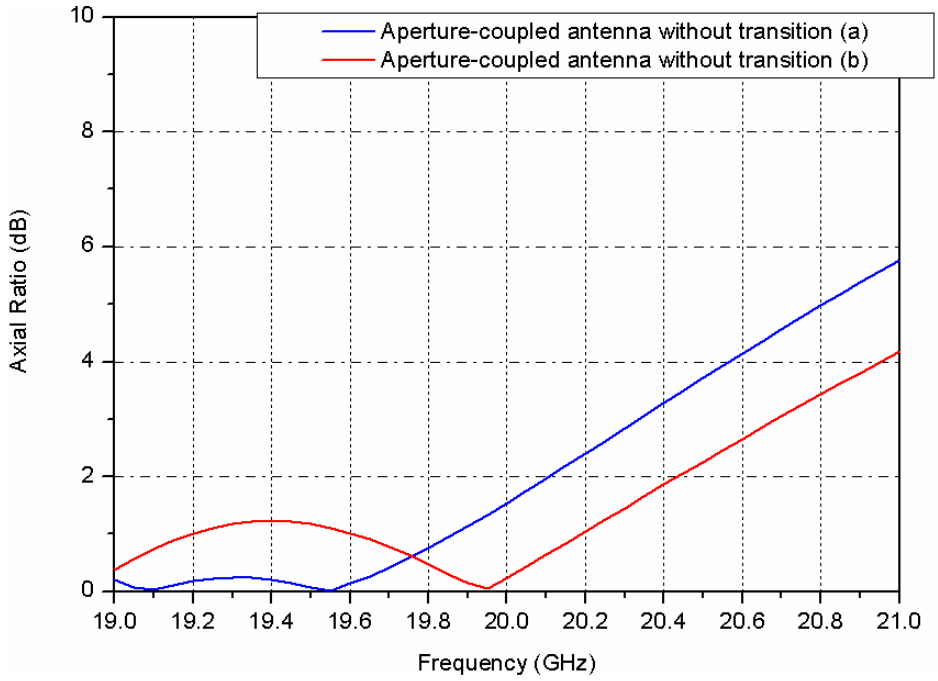

Figure 31: Axial Ratio when $\theta = 0°, \phi = 0°$, for the optimized aperture-coupled antenna without transition

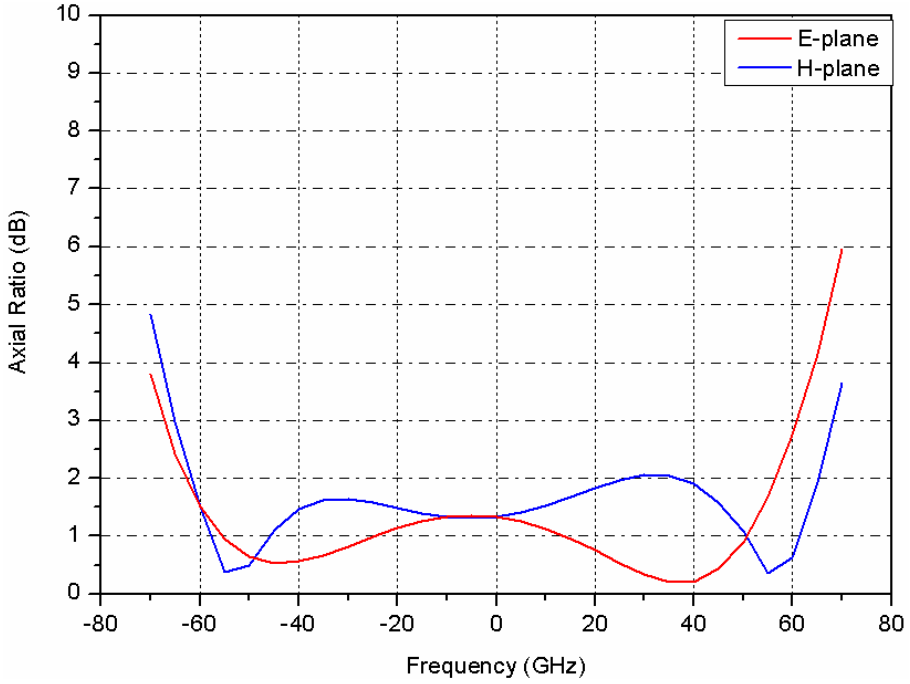

Figure 32: Axial Ratio in E-plane and H-plane at 19.95GHz for the optimized aperture-coupled antenna without transition

Figure 33-Figure 35 show the 3D radiation patterns of the aperture-coupled antenna without transition-VIA. A broad boresight and fairly good symmetry are clearly seen.

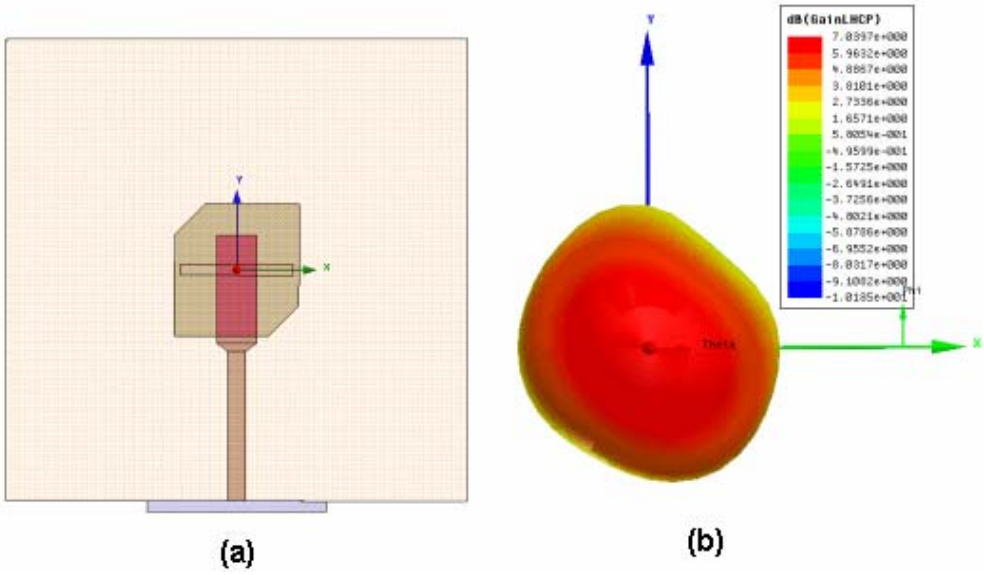

Figure 33: (a) Aperture-coupled antenna without transition top view, (b) 3D top view of LHCP gain

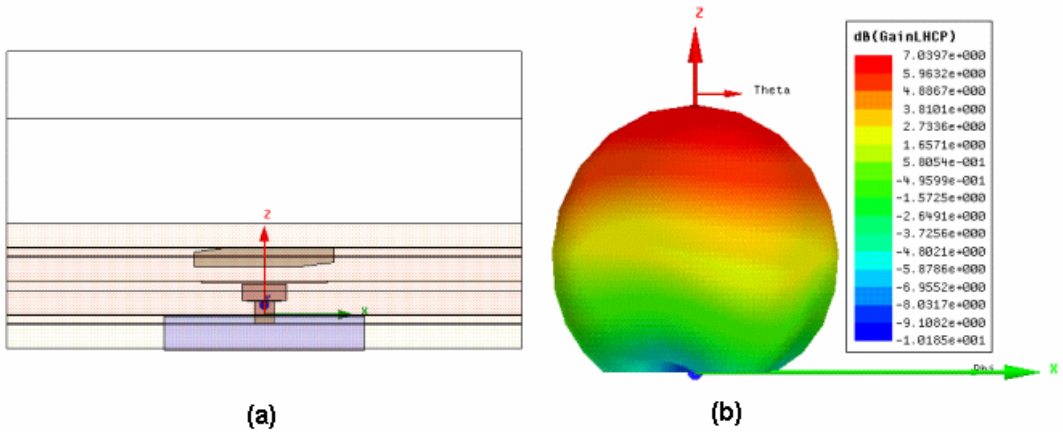

Figure 34: (a) Aperture-coupled antenna without transition front view, (b) 3D front view of LHCP gain

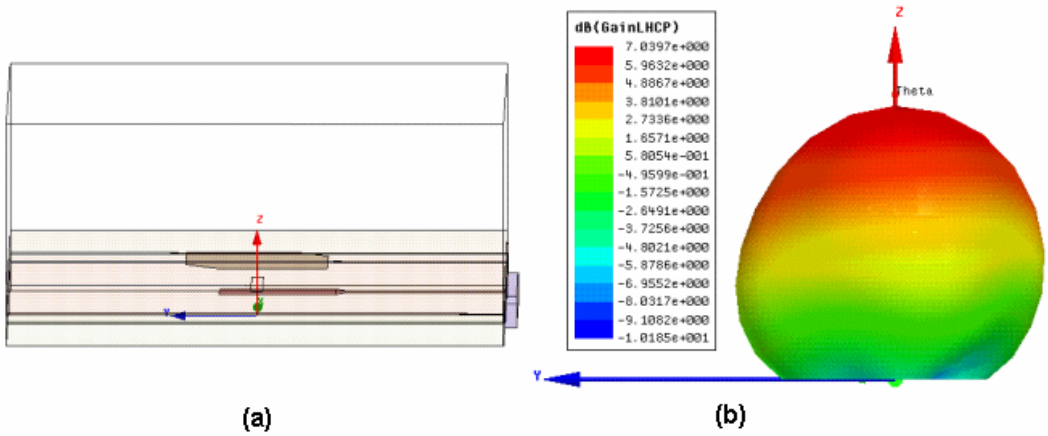

Figure 35: (a) Aperture-coupled antenna without transition side view, (b) 3D side view of LHCP gain

4.8.2 With transition VIA

Figure 36 shows the layer structure of the aperture-coupled antenna with transition-VIA. The glue layers (Neltec FV 6700 $\varepsilon_r = 2.35$ with the thickness 0.038mm) are also added to the model.

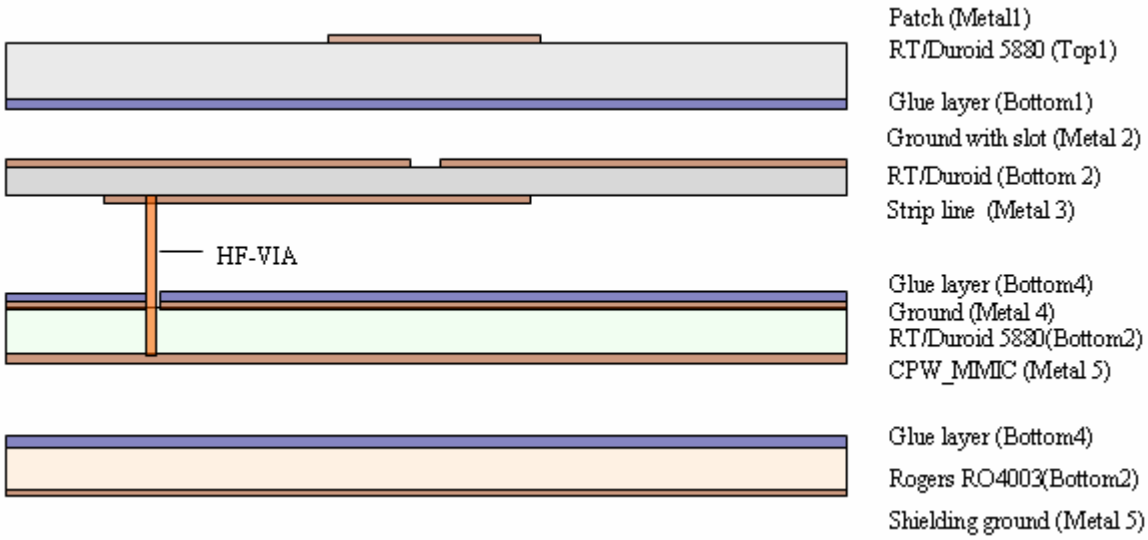

Figure 36: Layer structure for the optimized aperture-coupled antenna with transition-VIA

Similarly, Figure 37 shows the simulated S_{11} parameter for the antenna. A clear resonance can be noticed around 20 GHz with a -15 dB return loss bandwidth of more than 1.5 GHz. Within the whole operating bandwidth (19.7 GHz-20.2 GHz), the return loss is below -25 dB. Figure 38 shows a Smith chart plot of the antenna input impedance.

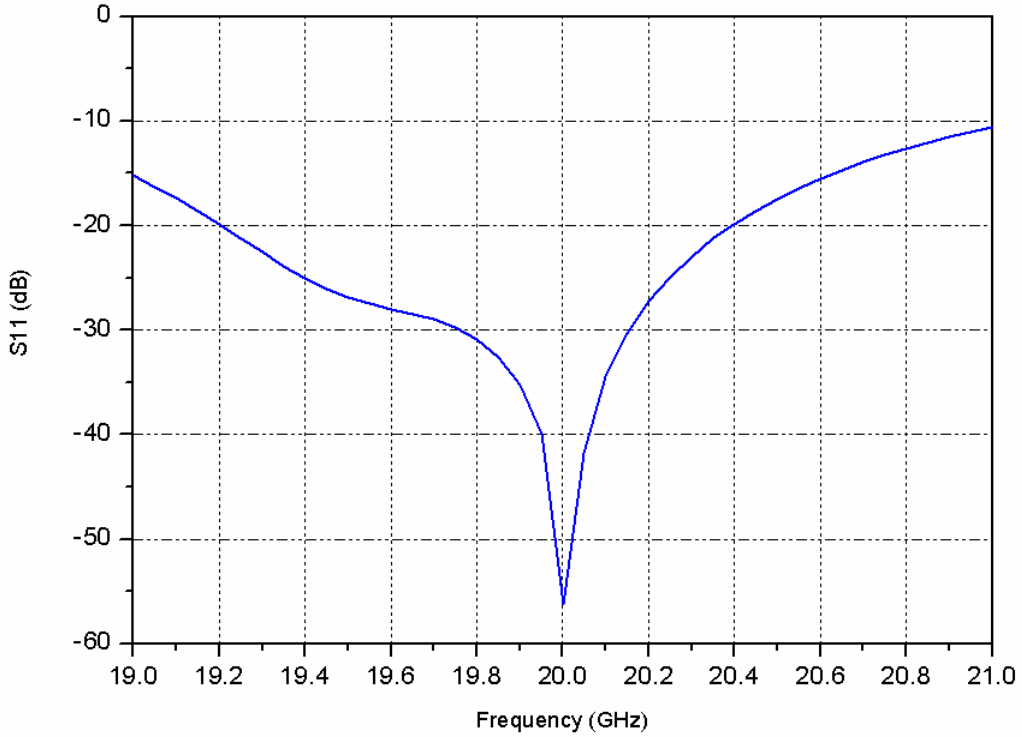

Figure 37: S_{11} for the optimized aperture-coupled microstrip feed antenna with transition

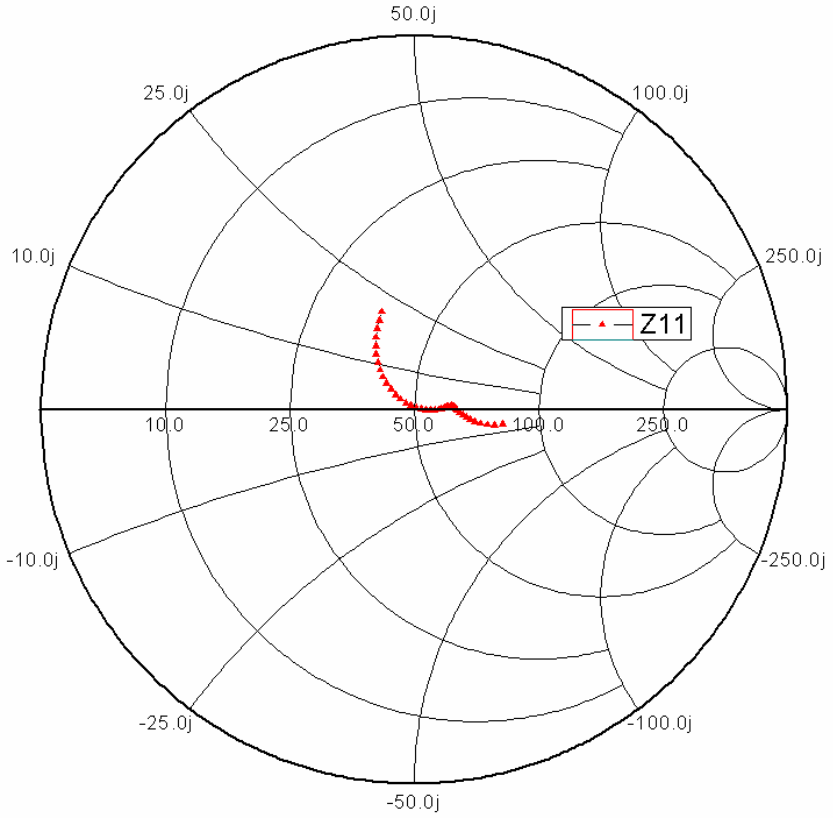

Figure 38: Smith chart representation of single antenna input impedance

The LCHP realized gain (which is the gain normalized to the input power) of aperture-coupled antenna with transition-VIA in E- and H- planes are shown in Figure 39. A gain of 5.3 dB is achieved in the main radiation direction. Compare the aperture-coupled antenna before adding transition-VIA (Figure 28), 1.7 dB gain is attenuated probably because of the adding of transition-VIA.

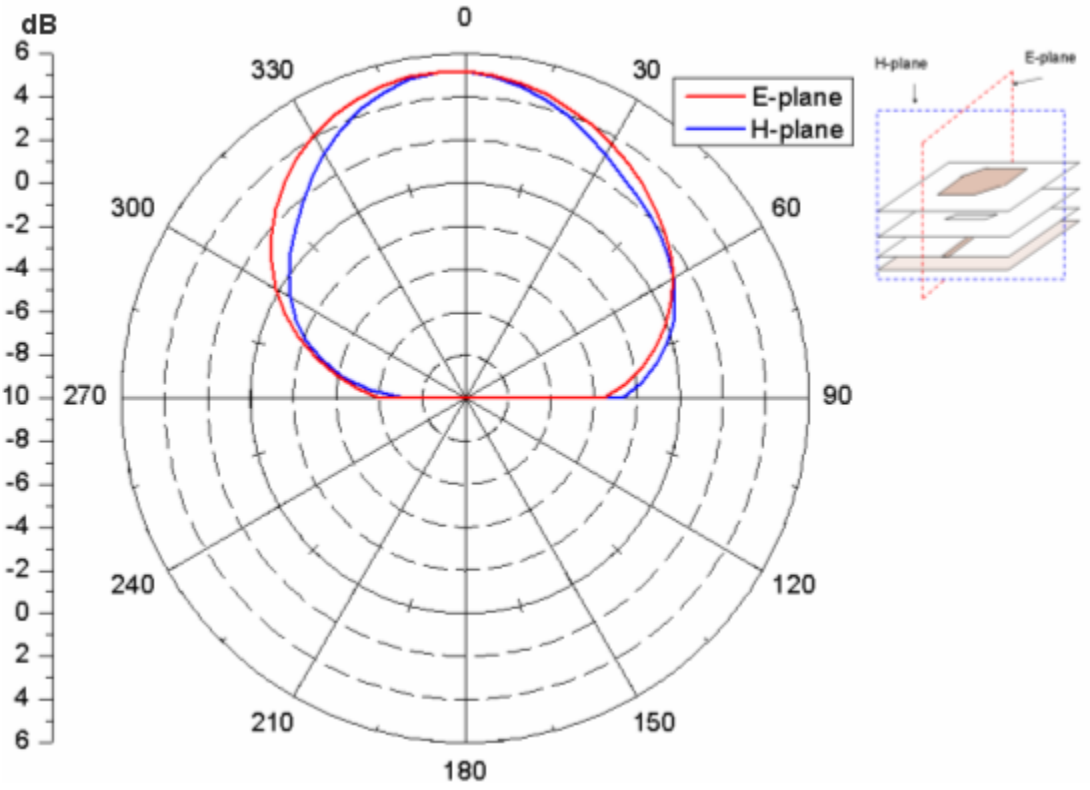

Figure 39: LCHP realized Gain of aperture-coupled antenna with transition in E- and H- planes at 19.95GHz

Figure 40 and Figure 41 present the realized gain for the left-hand-circular polarization (LHCP) and the right-hand-circular polarization (RHCP) in E- and H-planes respectively.

Figure 42 shows the axial ratio level from 19 GHz to 21 GHz. The axial ratio is nearly 0 dB at 19.95 GHz, and below 1dB in the operating bandwidth (19.7 GHz-20.2 GHz).

Figure 43 shows the axial ratio in E- and H-planes at the central frequency 19.95 GHz. In E-pane, there is about $95°$ beamwidth that the axial ratio is below 3 dB. In H-plane, $130°$ beam-width is observed for the axial ratio below 3 dB. Similar to the antenna without transition, slight asymmetry is found in both planes' axial ratio level.

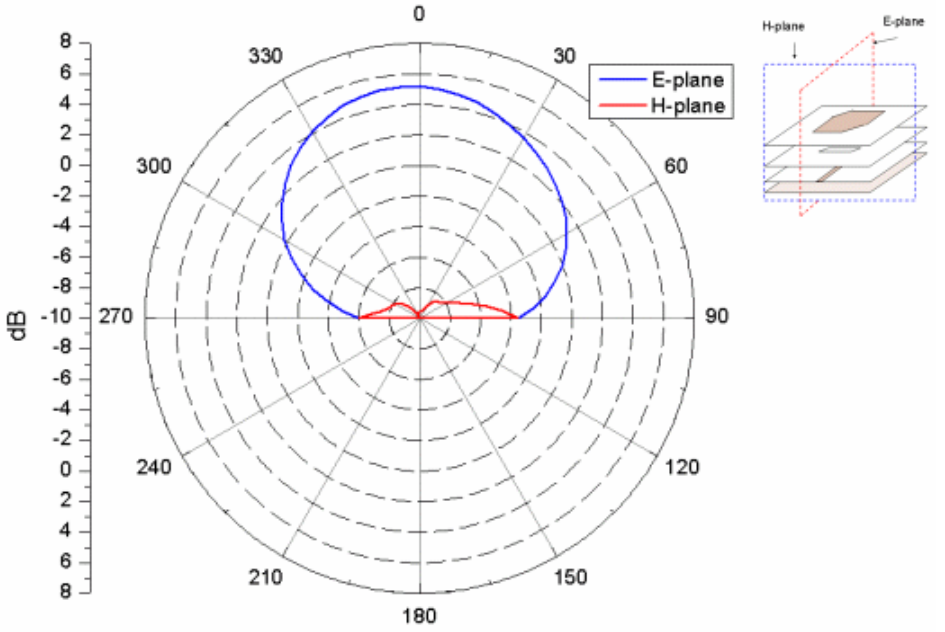

Figure 40: Realized gain for LHCP and RHCP in E-plane

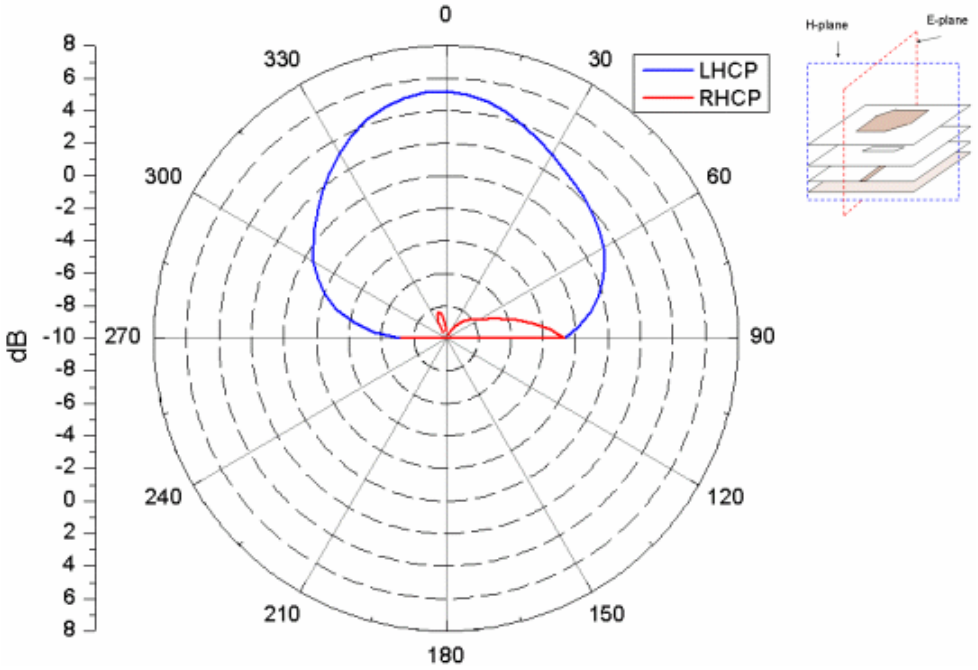

Figure 41: Realized gain for LHCP and RHCP in H-plane

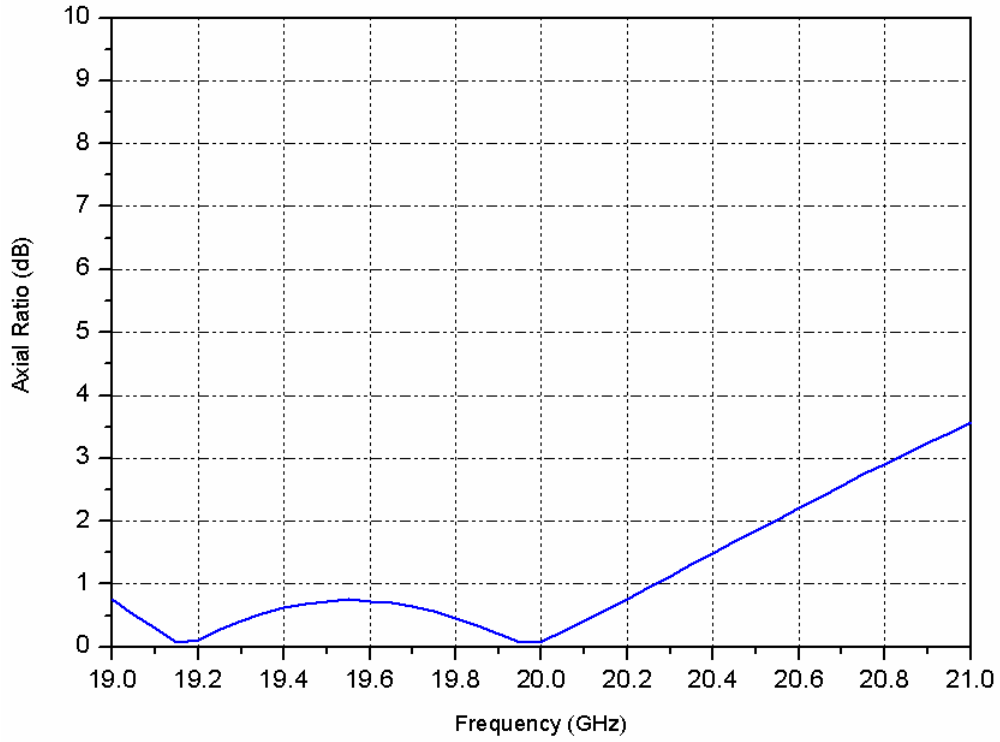

Figure 42: Axial Ratio for the optimized aperture-coupled microstrip feed antenna with transition

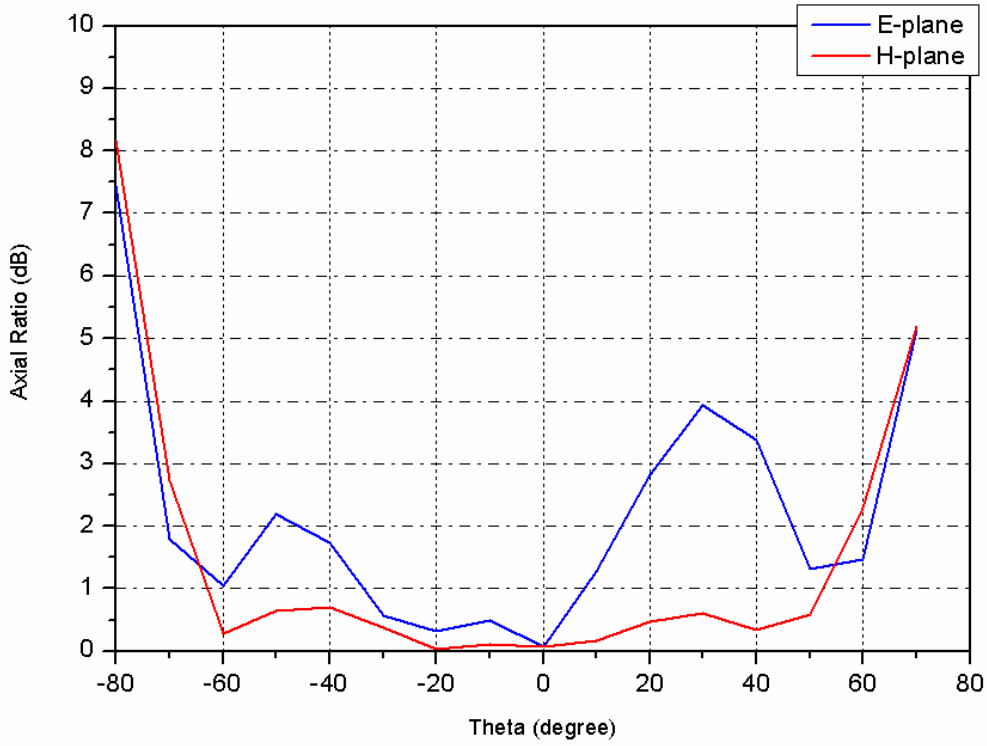

Figure 43: Axial Ratio in E-plane and H-plane at 19.95GHz for the optimized aperture-coupled microstrip feed antenna with transition

Fig 44-46 show the 3D radiation patterns of the aperture-coupled antenna with transition-VIA.

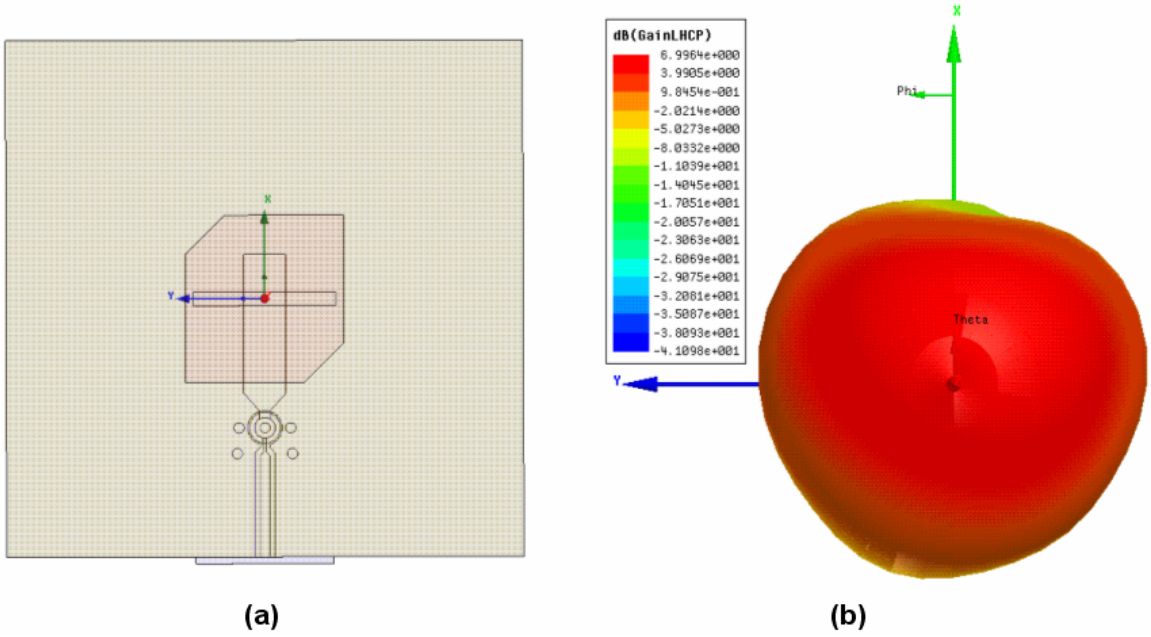

Figure 44: rE radiation pattern 3D top view

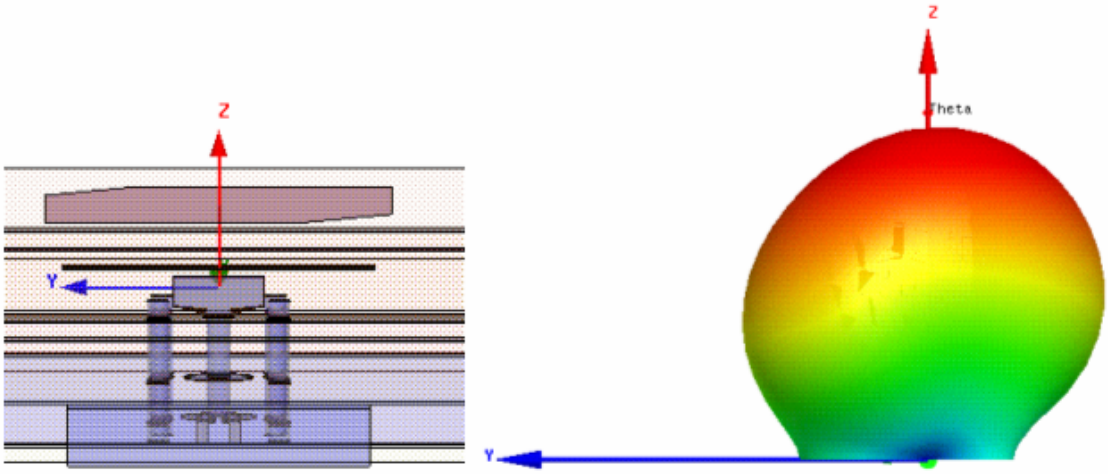

Figure 45: rE radiation pattern 3D side view I

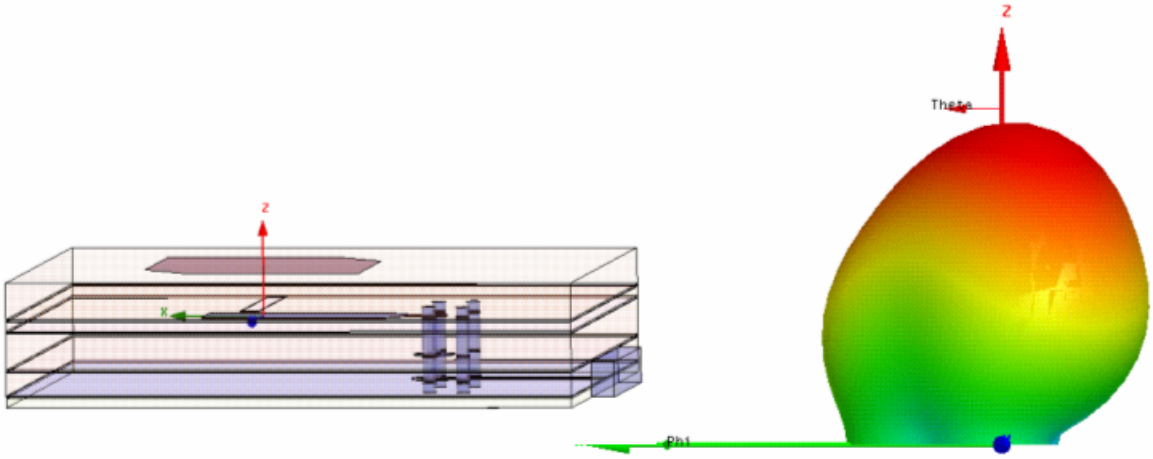

Figure 46: rE radiation pattern 3D side view II

Figure 44 shows the parametric study of series value of l_p (length of the patch),. Similar tendency is observed as shown in Figure 20, which proves the transparency of the transition-VIA to the antenna radiator.

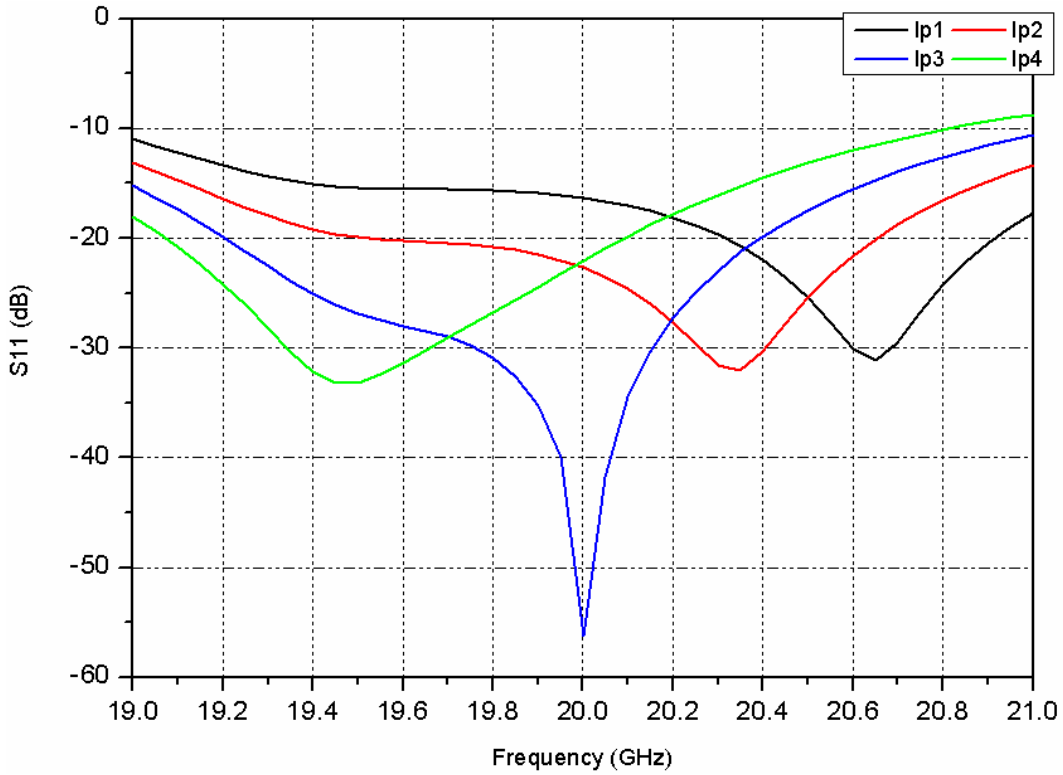

Figure 47: S_{11} values by different length of the patch, l_{p1}=4.65mm, l_{p2}=4. 75mm, l_{p3}=4.85mm, l_{p4}=4.95mm

5 GCPW-fed slot antenna

5.1 The advantages of using GCPW-fed

The microstrip feed for slot antennas suffers from the need for careful alignment of the etchings on the two sides of the board. Also, the use of a microstrip line is not compatible with monolithic fabrication and therefore easier integration with active solid-state devices is not possible. These problems can be solved by coplanar waveguide (CPW).

A conventional CPW on a dielectric substrate consists of a center strip conductor with semi-infinite ground planes on either side as shown in Fig 48. This structure supports a quasi-TEM mode of propagation.

The CPW offers several advantages. Firstly, the CPW is simpler and cheaper to be fabricated than the microstrip line, both the patch and feed lines can be etched in one step, and it eliminates the need for wraparound and via holes. Second, it has low radiation loss, dispersion and broader bandwidth, as a result of supporting quasi-TEM mode propagation as the dominant mode; the radiation form the CPW structure is negligible because the CPW is excited in the odd mode of the coupled slot line [17], due to this mode, the equivalent magnetic currents on both the CPW slots radiate almost out of phase, contributing negligibly to the feed radiation. This feature of a CPW feed is useful in the design of antenna arrays since mutual coupling between adjacent lines is minimized [4]. Third, the characteristic impedance is determined by the ratio of s/w (see Figure 48), so size increase or reduction is possible according to the antenna design or fabrication accuracy limitations; fourth, electric parameters of the CPW change little with the substrate thickness. Moreover, a ground plane exists between any two adjacent lines when the CPW-fed is used in the antenna array; hence cross talk effects between adjacent lines are very weak.

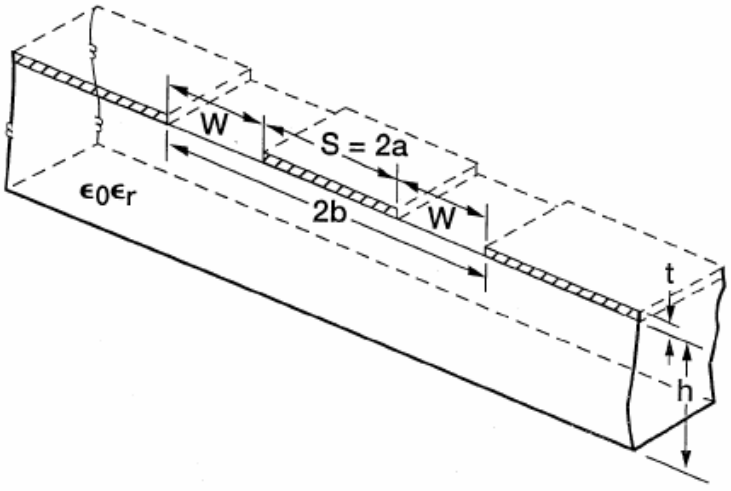

Figure 48: Schematic of a CPW on a dielectric substrate

In a conventional CPW, the ground planes are of semi-finite extent on either side. However, in this project the ground planes are made of finite extent. Thus, a ground plane is added at the back of CPW to form a grounded coplanar waveguide (GCPW) as shown in Figure 49. It is also called conductor-backed coplanar waveguide (CBCPW) in some literatures. This additional ground plane not only acts as a shielding, but also provides mechanical support to the substrate. Usually, the semi-width of the upper ground plane (where lies the coplanar line) is chosen to be greater than the coplanar waveguide wavelength λ_g at the patch resonance frequency. The center conductor width to the slot width ratio s/w is well selected to provide a good impedance match to the feeding via or the coaxial connector.

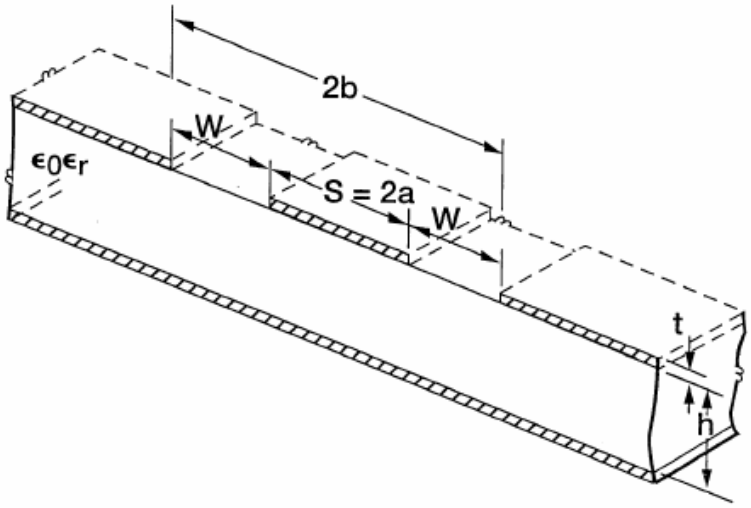

Figure 49: Schematic of a grounded coplanar waveguide (GCPW)

In the Appendix B.7 of [4], methods of designing different types of CPW are stated. The expressions for the characteristic impedance (Z_0) and effective dielectric constant (ε_{eff}) given below are based on the quasi-static analysis.

The underlying assumption in the analysis is that all the interfaces in the structure, including slots, can be replaced by magnetic walls. For analysis purposes, the transmission line structure is divided into two halves: the upper half, which is above the metallization, and the lower half, which is below the metallization. Capacitance per unit length for each half is determined by transforming it into a parallel plate geometry using conformal transformation. These capacitances yield the characteristics of the line, as in the case of a microstrip line. The closed-form expression for the effective dielectric constant (ε_{eff}) of the CPW is represented as

$$\varepsilon_{eff} = 1 + q(\varepsilon_r - 1) \qquad (5.1.1)$$

where q is called the filling fraction. Expressions for q are given below for the GCPW structure shown in Fig. 48 [4]:

$$q = \frac{K(k_2)/K'(k_2)}{K(k_1)/K'(k_1) + K(k_2)/K'(k_2)} \tag{5.1.2}$$

$$Z_{0cpw} = \frac{60\pi}{\sqrt{\varepsilon_{eff}}} \frac{1}{K(k_1)/K'(k_1) + K(k_2)/K'(k_2)} \tag{5.1.3}$$

where, the aspect ratio $k_1 = \frac{a}{b}$, $k_2 = \frac{\tanh(\pi a/2h)}{\tanh(\pi b/2h)}$.

5.2 Basic configuration of GCPW-fed slot antenna

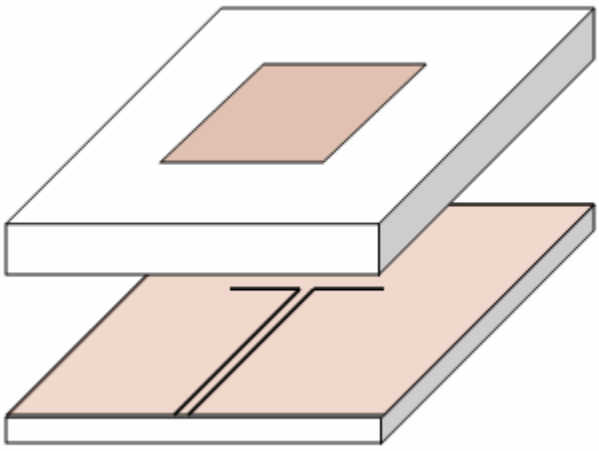

Figure 50: Structure of CPW-fed slot antenna

In Figure 50, a GCPW with a series gap in the center strip conductor is used to couple power to a patch through an aperture in the common ground plane. This is the basic configuration of GCPW-fed slot antenna. This design offers the flexibility of inserting semiconductor devices in the series gap of the feed for controlling the coupling.

The final designed GCPW-fed slot antenna configuration is shown in Fig 56. To achieve impedance matching, a tuning stub is added as depicted in Figure 9. Either an electrically open-ended stub or an electrically short-circuited stub can be used as the tuning stub. In the final design, an electrically open-ended stub is adopted. Note that, even though it is open-ended, it is not capacitively coupled, because the open end of the stub is not located under the center of the patch. Thus, it is equal to the configuration with $L_{stub} = 0mm$ and electrically short-circuited end [17]. For the basic configuration of inductive coupling, the center conductor of the CPW is connected across the slot, which is said to be inductively coupled, since the impedance locus lies in the inductive region on the Smith chart.

The substrate used in CPW-fed slot antenna is normally thick with thickness selected in odd multiples of a quarter-dielectric wavelength (λ_d). The power lost in the substrate due to the surface waves could be considerable when a single slot is used [18]. The loss decreased to half when some parasitic slots are used [18].

5.3 Theoretical model of GCPW-fed slot antenna

The analysis is based on the solution of mixed-potential integral equations by the method of moment (MoM), involving the evaluation of the Green functions of the structure. Since the backed-ground of GCPW causes the complexity in controlling the guided mode, the higher order modes introduce much complexity in computation. Also the geometric of the patch affects the radiated fields. As we did in the aperture-coupled antenna model analysis (see Chapter 4.3), the analyzed model is simplified to a CPW-fed slot patch with a rectangular patch. The main assumption (and limitation) allowing the calculation of the Green functions is that transversely infinite ground planes and substrates have to be considered [19].

The electromagnetic problem is expressed in terms of two integral equations where the unknowns are the distributions of surface electric current $\vec{J}_s$ and charge ρ_s^e on the patch, and the distributions of surface magnetic current $\vec{M}_s$ and charge ρ_s^m over the slots. The slots include the radiating slot, the CPW line and a CPW stub. The fields created by the electric sources are expressed in terms of scalar and vector potential V and $\vec{A}$ [19]:

$$\vec{E}\left(\vec{J}_s\right) = -j\omega\vec{A} - \nabla V, \tag{5.3.1}$$

$$\vec{H}\left(\vec{J}_s\right) = \frac{1}{\mu}\nabla \times \vec{A}, \tag{5.3.2}$$

The fields created by the magnetic sources are expressed in terms of scalar and vector potential ϕ and $\vec{F}$:

$$\vec{E}\left(\vec{M}_s\right) = -\frac{1}{\varepsilon}\nabla \times \vec{F}, \tag{5.3.3}$$

$$\vec{H}\left(\vec{M}_s\right) = -j\omega\vec{F} - \nabla\phi, \tag{5.3.4}$$

where $\varepsilon = \varepsilon_0\varepsilon_{diel}$ is the substrate permittivity. The continuity of the magnetic field across the apertures leads to the following integral equation:

$$
\begin{aligned}
&-\vec{e}_z \times \vec{H}^e(\vec{r}) \\
&= \vec{e}_z \times \left[-j\omega \int_{slots} \left(\overline{\overline{G}}_F^{diel}(\vec{r}/\vec{r}') + \overline{\overline{G}}_F^{air}(\vec{r}/\vec{r}') \right) \vec{M}_s(\vec{r}')\, dS' \right. \\
&\left. -\nabla \int_{slots} \left(G_\phi^{diel}(\vec{r}/\vec{r}') + G_\phi^{air}(\vec{r}/\vec{r}') \right) \rho_s^m(\vec{r}')\, dS' + \frac{1}{\mu} \nabla \times \int_{patch} \overline{\overline{G}}_A^{diel}(\vec{r}/\vec{r}')\, \vec{J}_S(\vec{r}')\, dS' \right]
\end{aligned}
\tag{5.3.5}
$$

while the cancellation of the electric field at the patch level yields a second integral equation,

$$
\begin{aligned}
&-\vec{e}_z \times \vec{E}^e(\vec{r}) \\
&= \vec{e}_z \times \left[-j\omega \int_{patch} \overline{\overline{G}}_A^{diel}(\vec{r}/\vec{r}')\, \vec{J}_s(\vec{r}')\, dS' \right. \\
&\left. -\nabla \int_{patch} G_V^{diel}(\vec{r}/\vec{r}')\, \rho_s^e(\vec{r}')\, dS' - \frac{1}{\varepsilon} \nabla \times \int_{slots} \overline{\overline{G}}_F^{diel}(\vec{r}/\vec{r}')\, \vec{M}_S(\vec{r}')\, dS' \right]
\end{aligned}
\tag{5.3.6}
$$

where $\overline{\overline{G}}_A$ and $\overline{\overline{G}}_F$ are the dyadic Green functions corresponding to the electric and magnetic vector potentials $\vec{A}$ and $\vec{F}$, respectively, created by $\vec{J}_s$ and $\vec{M}_s$. G_V and G_ϕ are the scalar Green functions corresponding to the electric and magnetic scalar potentials V and ϕ, respectively, created by ρ_s^e and ρ_s^m. The Green functions are expressed in terms of Sommerfeld integrals. The expressions of the electric Green functions can be found in Appendix A. The sources (surface charge and current densities) are located at points designated by $\vec{r}$. The integrations in equation (5.3.5) and (5.3.6) are performed over the source surface, namely the aperture's surface for the magnetic sources and the patch surface for the electric sources. The indices *air* and *diel* indicate whether the Green functions are calculated in the air or in the substrate. $\left(\vec{E}^e, \vec{H}^e\right)$ is the excitation field [19].

In the integral equations (Eq. 5.3.5, 5.3.6), the slots and the patch are divided into rectangular cells. The surface currents are expanded into rooftop basis functions overlapping two adjacent cells. The weight of each basis function is obtained by applying the Galerkin method and solving the MoM matrix equation [19]. The numerical excitation of the odd mode in the CPW line is provided by two magnetic charges located in both slot lines. These magnetic charges are equal in magnitude and $180°$ out of phase. The reflection coefficient of the antenna is extracted from the study of the standing wave in the line.

To reduce the computation time, the following simplifications are made: (i) the interactions between the magnetic current on the CPW line and the electric current on the patch are neglected. Therefore the corresponding elements in the MoM matrix are set to zero; (ii) no transverse component is assumed in the radiating slot, which implies that the slot width w must be small compared with the wavelength λ_g ($w < \lambda_g / 20$) [19].

5.4 Aperture geometry and substrate selection

The GCPW-fed aperture-coupled patch antenna basically consists of a resonant microstrip patch excited by a non-resonant aperture fed by a GCPW. A truncated-corner nearly square patch is again chosen to be the geometric of the patch (see Chapter 4.5). In Chapter 3.4, the two basic CPW feedline structure are presented, connecting with simple rectangular slots. In this chapter, we mainly concern to the different aperture configurations. The aperture configuration influences the input impedance of the antenna in a certain level. Figure 51 shows four different aperture configurations that are tested when choosing models. The rectangular slot are the most basic one, consist of a rectangular non-resonant slot excited by a shorted CPW. The second configuration is called Divided rectangular, which is a modification of the previous one that ends the slot in a U-shaped slot. The third one is a rectangular slot with stub. It is a modification of the rectangular slot by adding a stub of length L_S . The length of stub L_S is approximately $3\lambda_g / 4$ (λ_g is the guided wavelength), if it is based on the electrically short-circuited end configuration. If the stub is electrically open-ended, the required stub length is reduced by $\lambda_g / 2$ due to the $180°$ rotation of the impedance locus.

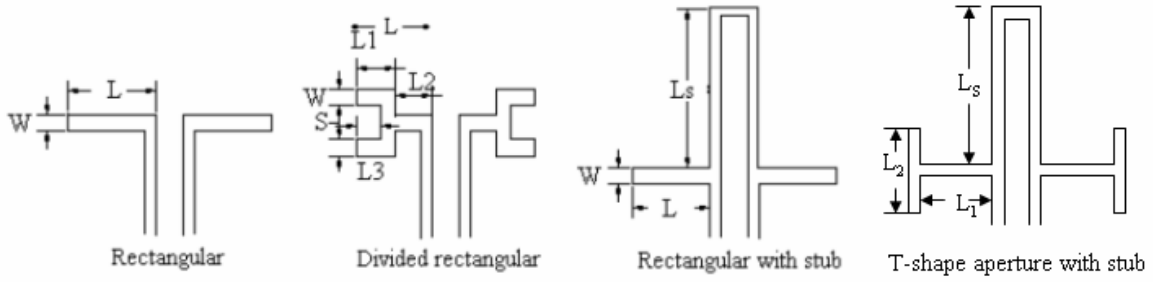

Figure 51: Sketches of the different slot configurations

The T-shape aperture with stub is the adaptive configuration of the previous one by adding two parallel slots perpendicular to the main radiating edges of the patch. As stated in Chapter 4.3, the coupling increases when the slot become shorter than the resonant length. The use of this T-slot enables selection shorter slots for the same amount of coupling, thus insuring that the slot can be operated well below its resonant frequency. This helps to excite TM_{01} mode, then increases the circular polarization level. The excitation slot contributes an inductive part to the total input impedance. The tuning stub with length L_s compensates this inductive effect.

The dielectric constant of the substrates determines the bandwidth at some level. We need the power coupled as much as possible to the patch. While the deeper the coupling level is, the narrower the impedance matching bandwidth is. In other words, the top patch should be “loosely coupled” in order to trade off the bandwidth. To do so requires the lower dielectric layer to have a greater dielectric constant than the upper layer. If the layers have the same dielectric constant or

the upper layer has a higher value, it will tight resonant loops and results in lower impedance bandwidths. But if the dielectric constant of the lower layer is too high, then it will aggravate the surface wave problem. For the thickness of the substrates, better use $h_1 \geq h_2$ (h_1 is the thickness of the GCPW substrate, h_2 is the thickness of the patch substrate). It is for the sake of better coupling the power to the patch. Thus a series of simulations have been done as following to find the best result.

5.5 Special considerations when using GCPW-fed structure

5.5.1 Propagating modes analysis

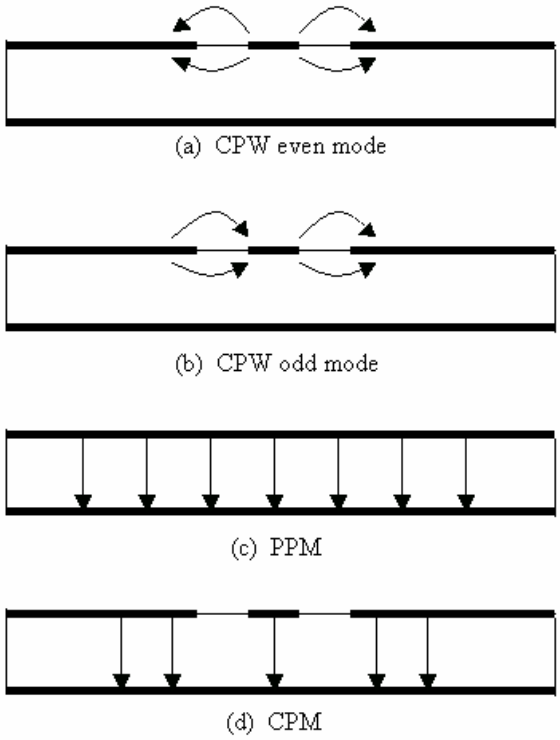

Figure 52: Schematic model of the field lines for the modes propagating in GCPW

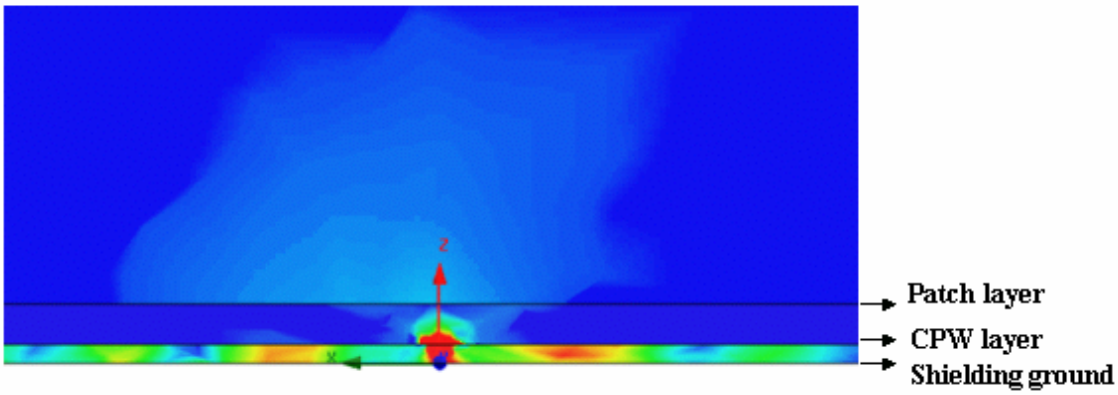

Figure 53: Strong PPM modes reduces radiation efficiency of the antenna

The dominant mode propagating in CPW is Quasi-TEM, which has no low frequency cutoff. This mode is a balanced mode (even mode) as shown in Figure 52(a). Since there are gaps on both sides of the center strip in the CPW, this configuration can be seen as two coupled slot lines. The coupled slot line mode may be excited in the CPW as an unbalanced mode (odd mode) as shown in Figure 52(b). To prevent excitation of this coupled slot line mode, air bridges between the two ground planes are often used so that the RF potentials of the two ground planes on both sides of the center conductor are kept equal. Here, series of VIAs are added because of the existence of the third ground plane.

As shown in Figure 52 (c) and (d), parallel-plate modes (PPM) and coplanar microstrip (CPM) modes are excited as unwanted modes in most GCPW (grounded coplanar waveguide). In order to remove heat from the active circuit below the CPW-feed and reduce the backlobe level, an additional ground plane is often added to the opposite side of the substrate accommodating a CPW as described in Chapter 5.2, This GCPW also provides a good mechanical characteristics. However, it causes the complexity in controlling the guided mode. First, in addition to the two ground planes on both sides of the central conductor, the third shielding ground must be maintained at the same RF potential. Otherwise, higher order modes are introduced such as PPM and CPM [22]. To solve this problem, series of VIAs are added between the upper grounds and the shielding ground. In addition, it is found that a leakage loss is caused by the wave propagating away from the central CPW region. This is due to the unwanted PPM. Obviously, the ground planes on both sides of the substrate form a parallel-plate waveguide. As shown in Figure 53, most of the power transmits as the parallel-plate waves between the CPW and the shielding ground below it. In this case, the radiation efficiency is very low.

The unwanted modes propagating in the GCPW-feed as shown in Figure 52(b), (c), (d) cause the leakage of power, which is the main component of the attenuation. Adding VIAs and air bridges can eliminate these modes; choosing the appropriate thickness and dielectric constant of the substrate, and using the GCPW-feedline as short as possible can reduce the influences of these unwanted modes. Further discuss is presented in the next chapter.

5.5.2 Analysis on high VSWR phenomenon when using broad GCPW feedline

To measure the antenna, a connector is soldered to the CPW feedline. Thus, the width of the CPW line should not be too narrow in order to connect with the pin of the connector. Connectors with the type 19S 102-40M from Rosenberger Hochfrequenztechnik GmbH & Co.KG are used in the fabrication. This kind of connector can work at the frequency 10GHz-26.5GHz, the pin's diameter is 0.4mm. This requires the width of the CPW line larger than 0.4mm. However, the broad CPW has spurious radiation problem, and the high VSWR (voltage standing wave ratio) of it reduces the radiation efficiency. The reason is analyzed in the following content.

If the feedline has no loss, and matches both the transmitter output impedance and the antenna input impedance, then will maximum power be delivered to the patch. In this case the VSWR will be 1:1 and the voltage and current will be constant over the whole length of the feedline. Any deviation from this situation will cause a standing wave of voltage and current to exist on the line.

$$VSWR = \frac{1+|\Gamma|}{1-|\Gamma|} \qquad (5.5.2.1)$$

Analysis of how the VSWR occurs on the feedline:

The reflection coefficient "Γ" is a measure of mismatch seen at the antenna by the feedline and is equal to:

$$\Gamma = \frac{(Z_a - Z_0)}{(Z_a + Z_0)} \qquad (5.5.2.2)$$

Here Z_a is the antenna impedance and Z_0 is the feedline impedance. These two impedances are both complex numbers. The phase of the reflected signal is advanced or delayed depending on whether the antenna appears inductive or capacitive to the feedline. If the antenna appears inductive, the voltage is advanced in phase, and if the antenna is capacitive, the voltage is delayed. The reflective signal travels back to the transmitter and adds to the incident signal at that point.

Thus, any mismatch at the antenna gives rise to a second 'traveling' wave which goes in the opposite direction from the incident wave. When $Z_a = Z_0$ the reflection coefficient is zero and there is no reflected signal. In this case, all power is absorbed by the antenna. This is the ideal situation where VSWR is concerned. The problem is that this condition is rare. As two traveling waves pass each other in opposite directions, they set up an interference pattern called a 'standing wave'. At certain places on the feedline the voltages will add producing a voltage maximum, and

at others their relative phase difference will cause a voltage minimum to exist on the feedline [26]. These maximum and minimum points occur $\frac{1}{4}\lambda$ apart (see Figure 54 below).

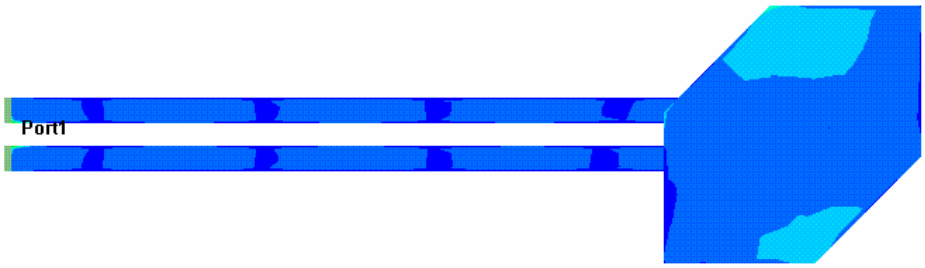

Figure 54: E-mag near field drawing of the CPW-fed antenna by Designer v2.1

Principally, the characteristic impedance Z_0 of the CPW is determined by $\frac{s}{w}$, s is the width of the center conductor of the CPW, w is the width of the slot. From this point of view, the broad CPW and narrow CPW could have the same characteristic impedance. However, it is preferable to use a small value of s, as in this case the magnetic currents through the slots of the CPW flow in each other's proximity and properly cancel out each other's radiation. For this reason, smaller values of s result in less spurious radiation (feeding radiation, excitation of surface waves, etc.) from the CPW-feed. Comparing the simulation results of different groups of s and w, with the same theoretical Z_0 as shown in Figure 55 and Figure 56, it is obviously that, for the narrow GCPW line, the return loss doesn't change much when extending the GCPW-feed; but the opposite situation for the broad GCPW line. In order to ignore the discontinuity between the excitation wave port and the CPW feedline, we don't normalize the CPW feedline to 50 ohm, then the "renormalization" function in the Ansoft HFSS is forbidden. Since the characteristic impedance of the CPW feedline is about 56 ohm, we use this 56 ohm to normalize the Smith chart. When we draw it in Origion Pro 7.0, we will have a Smith chart with the center point 1.2. In [26], some experiments are carried on different width of CPW. It is proved that, CPW transmission lines can be perturbed by interaction with surface wave modes if the ground-to-ground spacing is to large relative to the dielectric waveguide and substrate height. This may prove to be a concern when using long CPW lines (i.e. longer than $1000\mu m$) on thin substrates unless $(s+2w)/T < 0.3$.

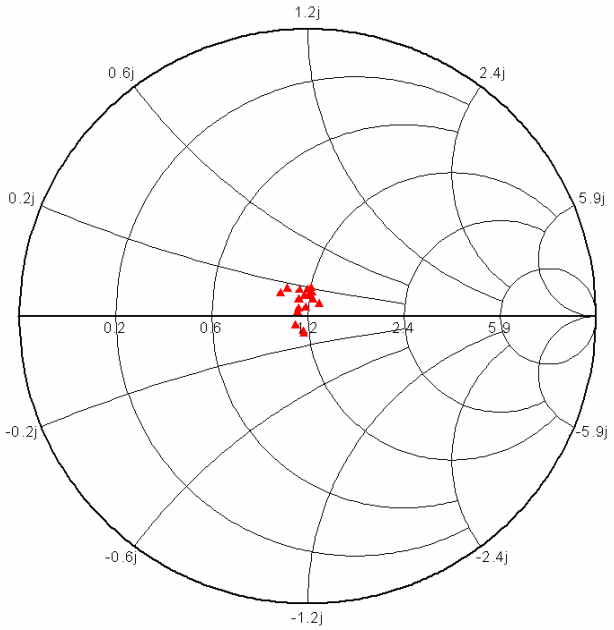

Figure 55: Plot of S parameters at the port when tuning the length of CPW feedline. s=0.45mm, w=0.1mm

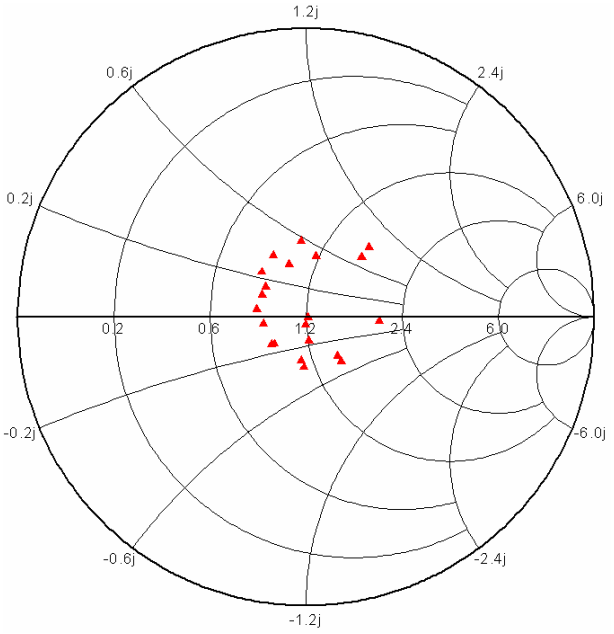

Figure 56: Plot of S parameters at the port when tuning the length of CPW feedline. s=1.15mm, w=0.25mm

After a series of tests, the reason of strong VSWR can be concluded as following:

1. The wide slot has spurious radiation reduces the efficiency of the antenna.

2. The presence of the shielding plane and the CPW ground plane promote the generation of parallel plate modes, reducing the efficiency of the antenna. Extending the CPW will deteriorate the antenna efficiency and distort the pattern.
3. The existence of the odd mode in the CPW causes the unwanted slot line modes. This also reduces the efficiency, but not as much as the parallel plate modes.
4. Since the results were achieved by simulating software. If the length of feed line between a discontinuity and a port is too short that results can also be distorted.

5.6 Approach to impedance matching

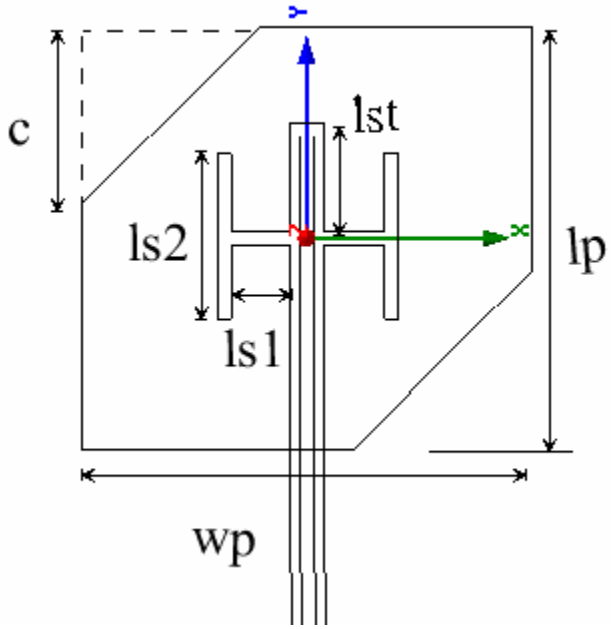

Figure 57: The geometric of the patch and the GCPW-feed

In Chapter 3.4 and 5.2, the effects of the different CPW feedline and coupled slots are presented respectively. For good impedance matching, the total input impedance at the excitation port should be pure real value and numerically equal to the characteristic impedance of the port. On Smith chart, impedance matching expresses as the S_{11} curve passing the center, when it is at the central frequency of the operation bandwidth. For the reason stated in Chapter 3.4, inductively coupled apertures and open-ended GCPW feedline with tuning stub are used here. The dimensions of the GCPW are always chosen in such a way that an odd-mode characteristic impedance Z_0 (Eq. 5.1.3) of 50Ω is obtained. Resonant frequencies are defined at maximum of the real part of the input impedance Z_{in} [21].

It is quite tricky to achieve the impedance matching for this GCPW-fed antenna, since the geometry structure is complex which has more than ten parameters. All of these parameters could influence both the matching between the antenna patch and the feedline and the matching between the feedline and the port. Thus, it is important to find out the key parameters and their influences to the antenna systems. Figure 57 shows the design of GCPW-fed antenna structure.

Through observing the tendency of matching changes when changing the certain parameters, some rules have been concluded. In case when $l_{s2} = 0$ mm, the impedance matching can be accomplished by tuning the slot length l_{s1} to make the impedance locus touch the $r = 1$ circle on the Smith chart. This equals to tune the real part of the input impedance. However, in order to achieve the circular polarization, crossing aperture gives better axial ratio than the single direction aperture. Then the affect to the impedance matching when tuning the length of aperture becomes more complex than single direction aperture. A parametric of simulations runs on the Ansoft Designer, and the following smith chart shows how Z_0 of the port changes when the apertures in two directions changes respectively. Figure 58 shows how the S parameter at the feeding point changes when l_{s1} increases from 0.36mm to 1.96mm, Figure 59 shows the case when l_{s2} increases from 0.8mm to 2mm. It is observed that, when tuning l_{s1} and l_{s2} separately, the matching point is not moving along the real axis. It shows that tuning l_{s1} and l_{s2} has the similar effects on the S_{11} parameter. It should be noted that, in HFSS, the port is not renormalized to 50 ohm in order to ignore the discontinuity between the excitation port and the feedline. As a result, the center point of the Smith chart is not necessarily to be 1. For example of Figure 58, the center point of the Smith chart is 1.1, which means the characteristic impedance of the feedline is 55 ohm.

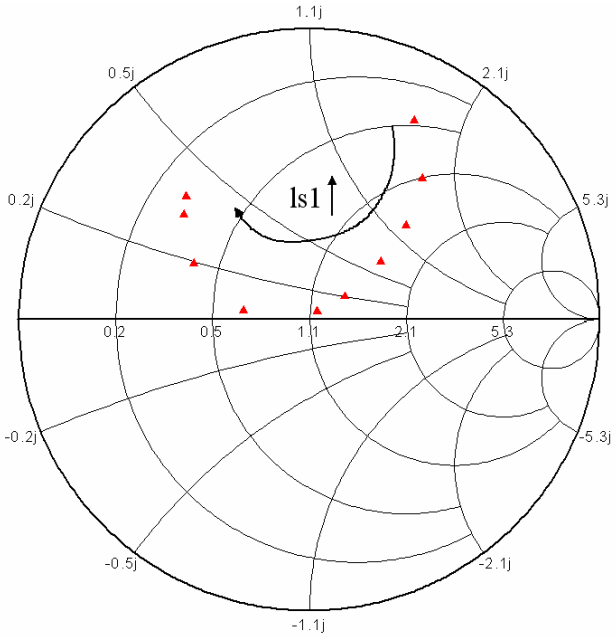

Figure 58: Smith Chart plot of the S parameter when l_{s1} increases from 0.36mm to 1.96mm

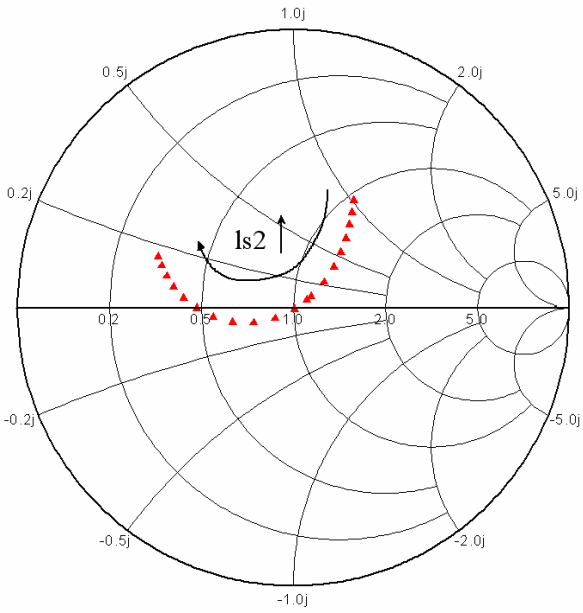

Figure 59: Smith Chart plot of the S parameter when l_{s2} increases from 0.8mm to 2mm

Figure 60 shows the Smith plot of S_{11} parameters when tuning the GCPW stub length l_{stub} from 0.97mm to 1.97mm. As mentioned before, the antenna patch has complex characteristic impedance. Hence, a CPW tuning stub is added to the end of the short-circuited CPW line. This tuning stub helps to cancel out the imaginary part of the antenna patch's impedance, thereby achieving the impedance matching between antenna patch and the feedline. It is equal to rotate the impedance locus toward the real axis of the Smith chart.

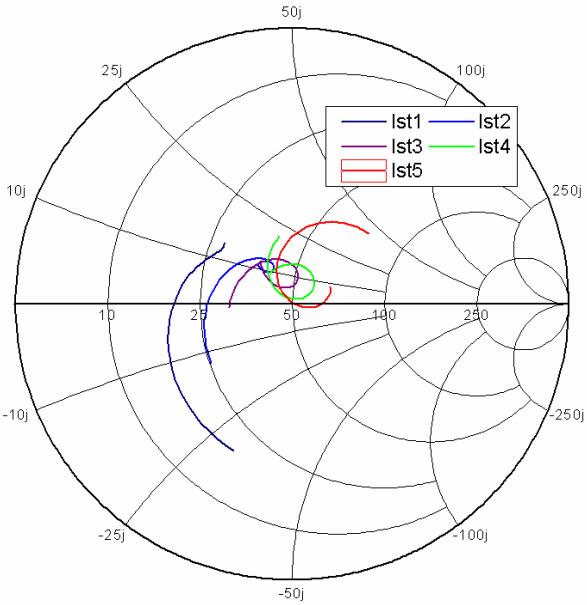

Figure 60: Smith Chart plot of the input impedances for different CPW stub lengths at frequency 19 GHz- 21GHz, l_{st1} =1.97mm, l_{st2} =1.67mm, l_{st3} =1.47mm, l_{st4} =1.27mm, l_{st5} =0.97mm

5.7 The optimized configuration of GCPW-fed antenna

Figure 61 and Figure 62 show the optimized layer structure and the basic design parameters for the GCPW-fed antenna. Similarly to the aperture-coupled antenna, one can control the size of the radiating patch (l_p, w_p) to tune the resonant frequency of the antenna and its return loss bandwidth. Two different layer structures with their geometry dimensions respectively are optimized. Figure 61(a) shows the configuration which uses Rogers 5880 ($\varepsilon_r = 2.2$) with the thickness 0.787 mm as the substrate of the patch, and Rogers TMM 10i ($\varepsilon_r = 9.8$) with the thickness 0.381 mm as the substrate of the GCPW feedline. With a high dielectric constant substrate under the GCPW, the coupling level between the GCPW and the patch decreases, instead the bandwidth is enhanced. Thus, the good axial ratio and impedance matching can be achieved in the same bandwidth. But the parallel plate modes (PPM) in this structure are very serious because of the small distance between the CPW feedline and the shielding ground. In order to reduce the influence of the PPM, a layer structure as shown in Figure 61(b) is adopted, which uses Rogers 5880 ($\varepsilon_r = 2.2$) with the thickness 0.787 mm as the substrate of the patch, and Rogers 5880 ($\varepsilon_r = 2.2$) with the thickness 3.175mm as the substrate of the GCPW feedline. In Figure 61(b), the distance between the CPW feedline and the shielding ground increases, in order to reduce the influences of the shielding ground. By this means, the PPM modes can be reduced to an acceptable level. While the PPM can not be completely removed unless the shielding ground is removed. Besides the geometry of the patch, as presented in Chapter 5.6, the configuration of the GCPW slots and the stub l_{s1}, l_{s2}, l_{st} need to be tuned. Additionally, in the final optimized configuration, a tapered GCPW-line is added to the end of the narrow GCPW-feedline, in order to offer the transition-VIA pad.

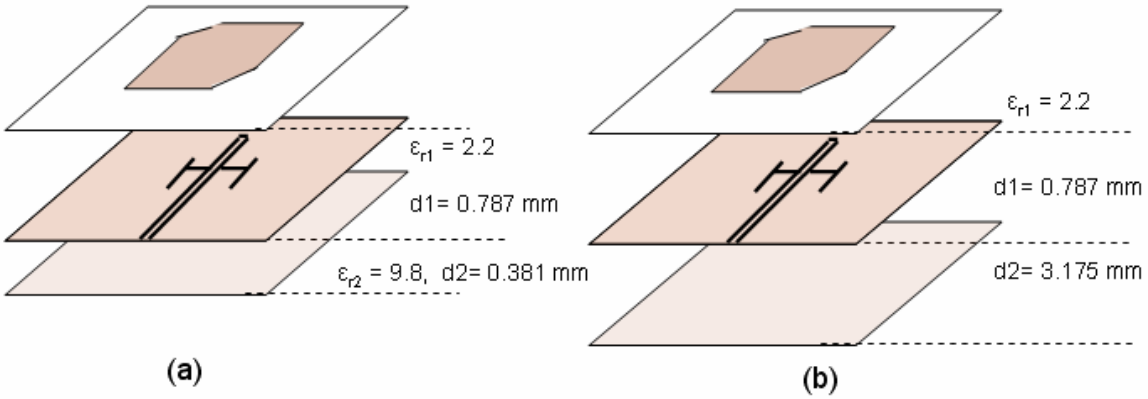

Figure 61: Two optional layer structures of optimized GCPW-fed antenna

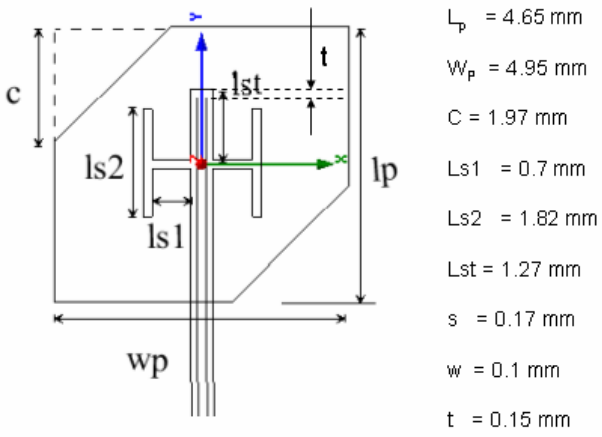

Geometry parameters for layer structure (a)

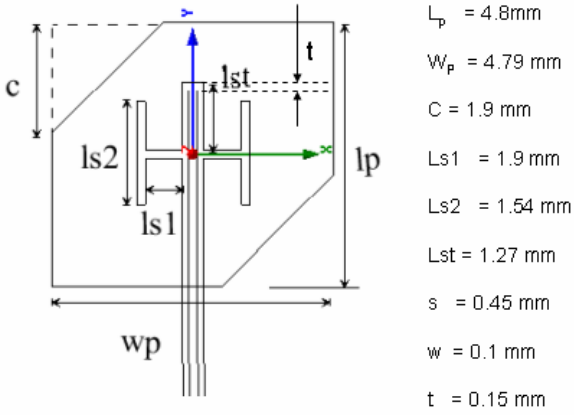

Geometry parameters for layer structure (b)

Figure 62: Schematic and dimensions of the optimized GCPW-fed antennas shows in Fig. 61

5.8 Simulation result and analysis

In Figure 61(a), though the impedance matching and the axial ratio level are all good, the gain is extremely low because of the loose coupling between the GCPW feedline and the patch. Thus the structure as shown in Figure 61(b) is used for optimization. The corresponding simulation results are given in Figure 63-Figure 70. First of all, the simulated S_{11} parameter for the antenna is shown in Figure 63. Compare to aperture-coupled antenna, the GCPW-fed antenna has broader bandwidth. An obvious resonance of -43dB can be noticed around 20 GHz with a -25 dB return loss bandwidth of more than 2 GHz. Within the whole operating bandwidth (19.7 GHz-20.2 GHz), the return loss is below -32dB. Figure 64 shows a Smith chart plot of the antenna input impedance.

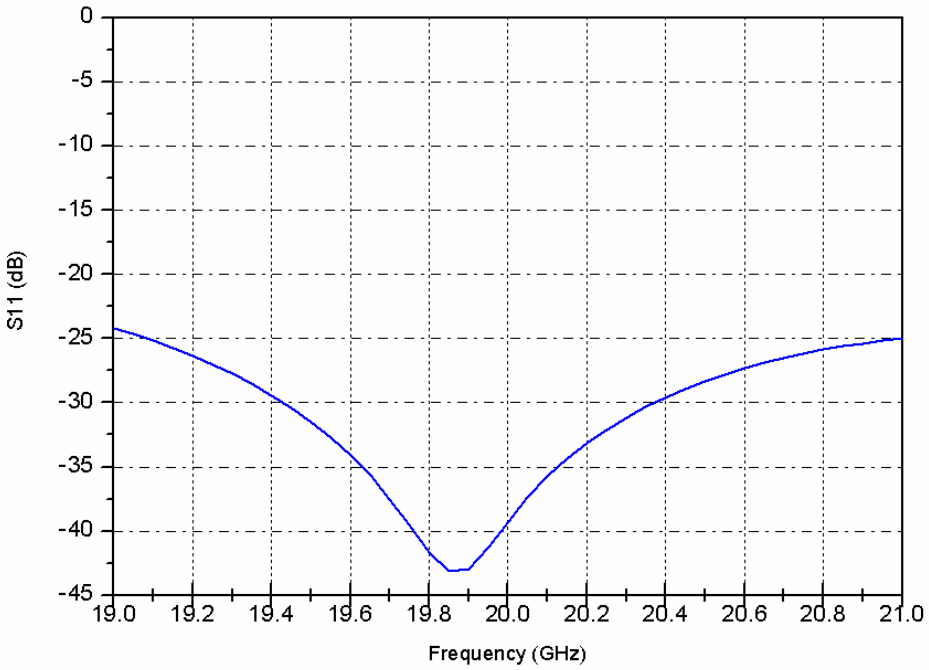

Figure 63: S_{11} parameter for the optimized GCPW-fed antenna

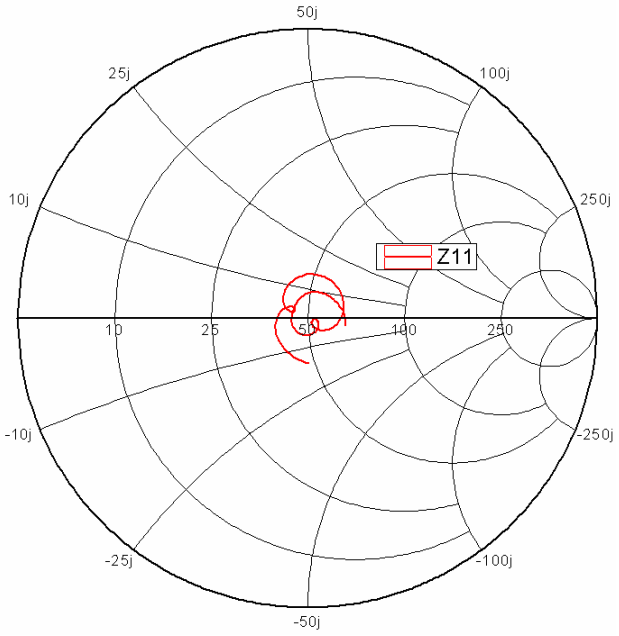

Figure 64: Smith chart representation of GCPW-fed input impedance from 15 to 25GHz

The realized gain represents for the antenna gain normalized by the input power. The realized gain of LHCP at the central frequency 19.95 GHz in E- and H-planes are shown in Figure 65. In the main radiation direction, the radiator has a gain of 4.3 dB. Compare to the aperture-coupled antenna, GCPW-fed antenna has lower gain.

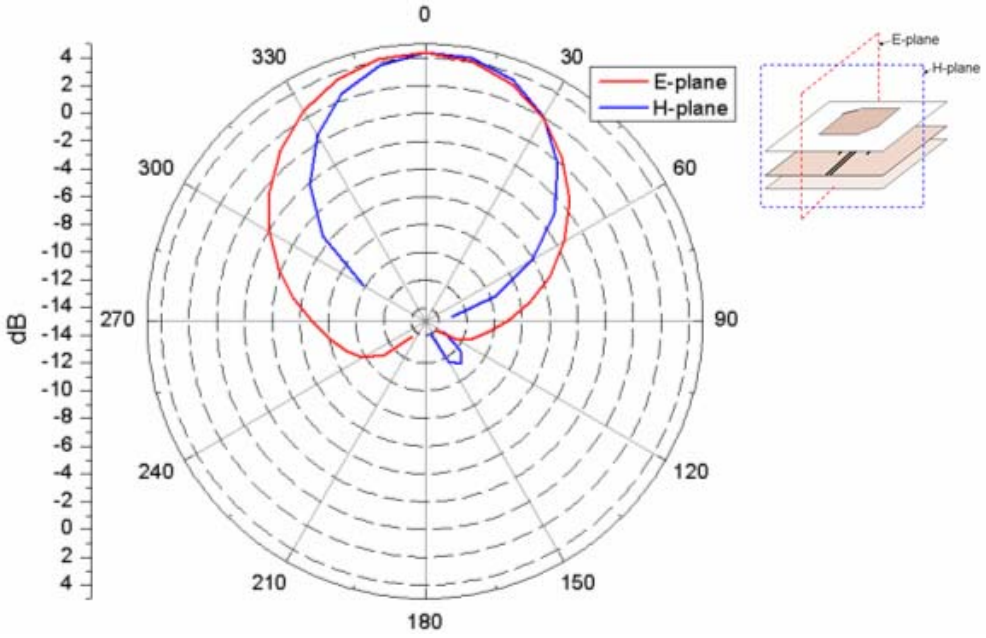

Figure 65: LCHP realized Gain of GCPW-fed antenna with transition in E- and H- planes at 19.95GHz

Figure 66 and Figure 67 present the realized gain for the LHCP and the RHCP in E- and H-plane at the frequency 19.25 GHz. It is found that, this structure is not optimized on circular polarization, which can only get acceptable circular polarization at 19.25 GHz. Further improvement could be done to improve its performance as a circularly polarized radiator (see Chapter7.2).

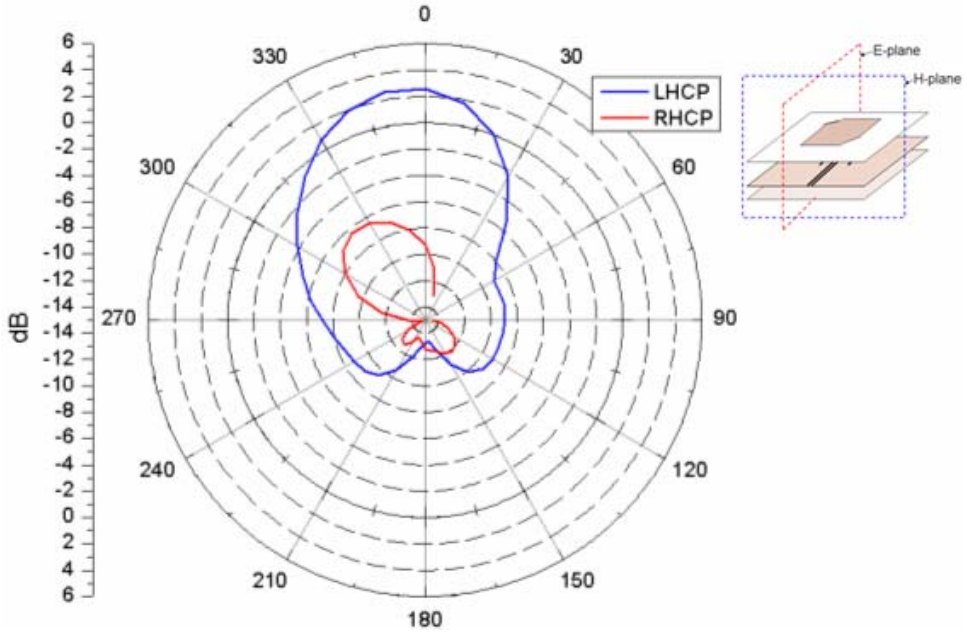

Figure 66: Realized gain for LHCP and RHCP in E-plane for the GCPW-fed antenna at 19.25GHz

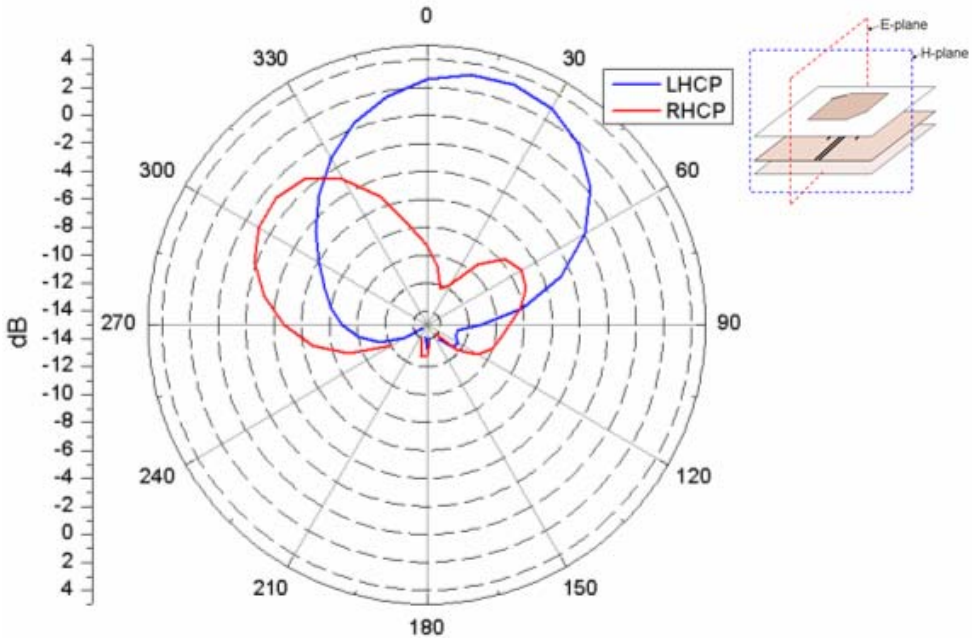

Figure 67: Realized gain for LHCP and RHCP in H-plane for the GCPW-fed antenna at 19.25 GHz

From 68-Figure 70, we can see that the 3D realized gain patterns of the GCPW-fed antenna are asymmetrical and irregular especially in H-plane. This is possibly due to the complex geometric of the GCPW feeding slots.

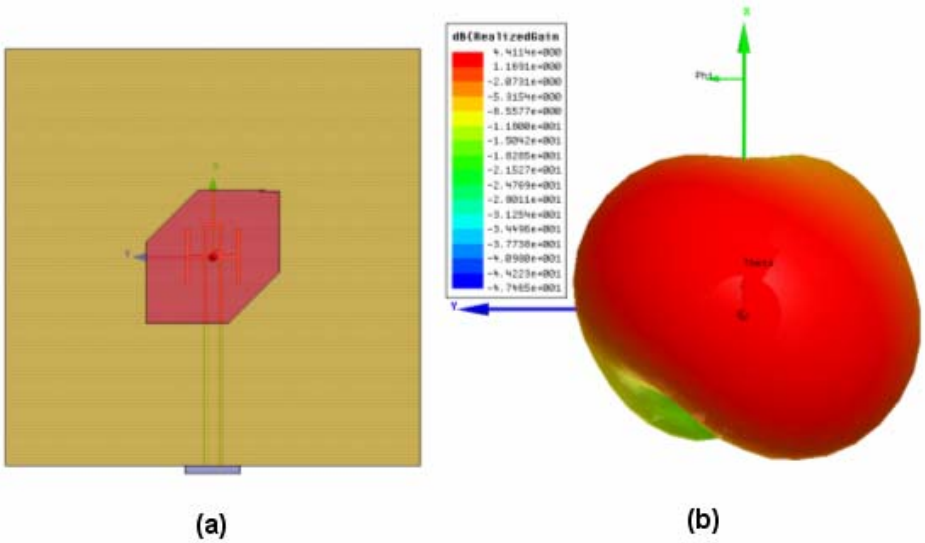

Figure 68: Realized gain 3D plot in HFSS-Top view for the optimized GCPW-fed antenna

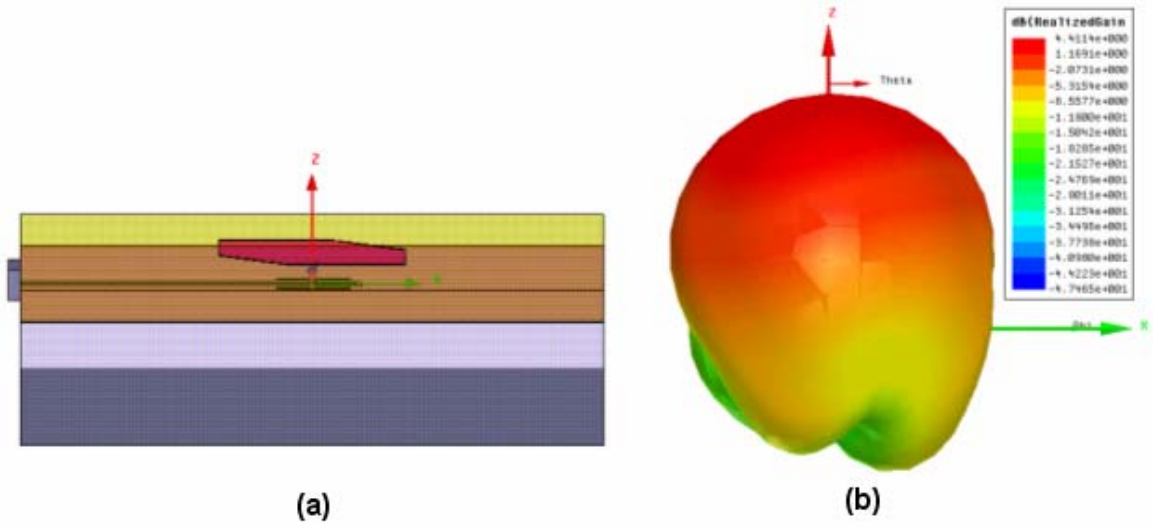

Figure 69: Realized gain 3D plot in HFSS-Side view for the optimized GCPW-fed antenna

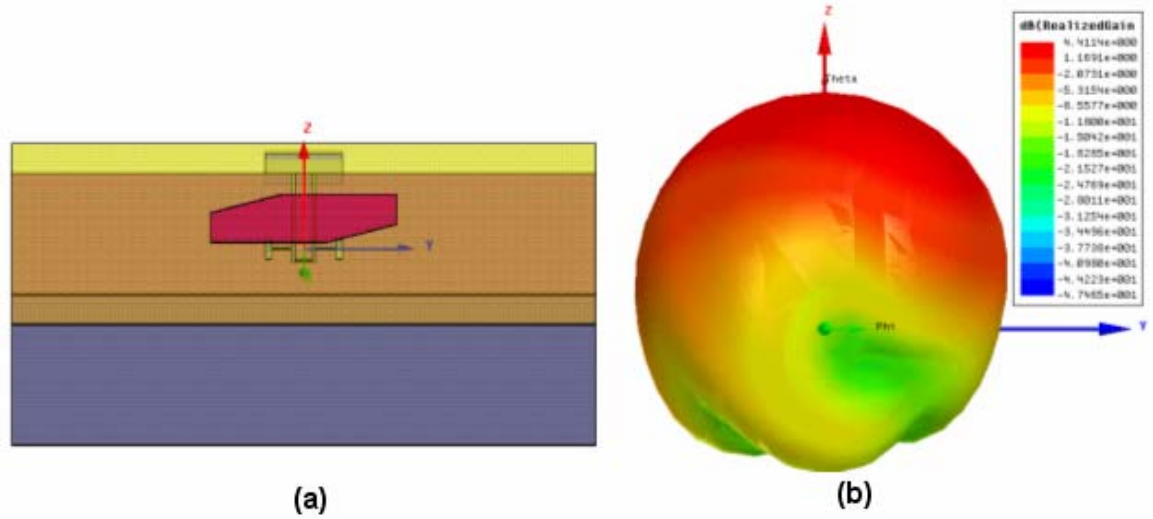

Figure 70: Realized gain 3D plot in HFSS-Front view for the optimized GCPW-fed antenna

5.9 Fabrication consideration

From an optimized model to the final model for fabrication, many factors related to fabrication should be taken into account. For the fabrication, many factors should be taken into account, such as interconnection with the connectors, the arrangement of glue layers and vias between the grounds. Some of these factors can be add into the HFSS model, for example glue layers, vias, even the tolerance of the fabrication, then the influences from them can be observed from the simulation result.

However, some factors seem not be necessary to add into the HFSS model, but may influence the measurement result in unexpected way.

5.9.1 Interconnection impedance compensation

Figure 71 shows the interconnection between the connector and the CPW feedline. Because of the capacitive behavior of the bump discontinuity a CPW section with high Characteristic impedance is the appropriate counteraction in view of minimizing return loss. Some assumptions and estimations should be used when designing the CPW in the HFSS. A dauntless assumption of 70 ohm to the feeding port has been used in this design. By using the renormalization function in Ansoft HFSS, the output impedance at the port can be setup to certain values. Then select correct widths for the CPW feed line to achieve the 70 ohm characteristic impedance.

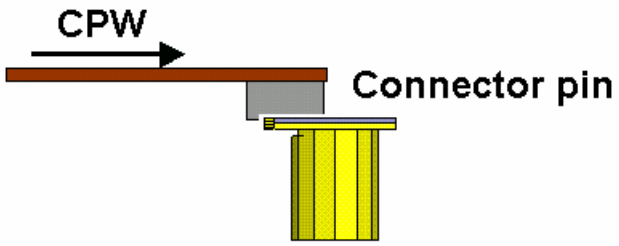

Figure 71: Interconnection between the connector and CPW feed line

6 Measurement

6.1 TRL Calibration

A major problem encountered when making network measurements in microstrip or other non-coaxial media is the need to separate the effects of the transmission medium, in which the device is embedded for testing, from the device characteristics. While it is desired to predict how a device will behave in the environment of its final application, it is difficult to measure this way. The accuracy of this measurement depends on the availability of quality calibration standards [28].

The TRL calibration technique relies only on the characteristic impedance of a short transmission line. From two sets of 2-port measurements that differ by this short length of transmission line and two reflection measurements, the full 12-term error model can be determineed. Due to the simplicity of the calibration standards, TRL can be applied in dispersive transmission media such as microstrip, stripline and waveguide. With precision coaxial transmission lines, TRL currently provides the highest accuracy in coaxial measurements available today.

Table 2: Requirements for TRL standards

Standard	Requirements

REFLECT	Reflection coefficient Γ magnitude(optimally 1)need not be known Phase of Γ must be known within $\pm 1/4\lambda$ Must be the same Γ on both ports May be used to set the reference plane if the phase response of the REFLECT is well-known and specified
THRU	Characteristic impedance Z_0 of the THRU and LINE must be the same Attenuation of the THRU need not be known Insertion phase or electrical length must be specified if the THRU is used to set the reference plane
LINE	Z_0 of the LINE establishes the reference impedance after error correction is applied Insertion phase of the LINE must never be the same as that of the THRU(zero or non-zero length) Optimal LINE length is $1/4\lambda$ or $90°$ relative to the THRU at the center frequency Useable bandwidth of a single THRU/LINE pair is 8:1(frequency span/star frequency) Multiple THRU/LINE pairs (Z_0 assumed identical) can be used to extend the bandwidth to the extent transmission lines are realizable Attenuation of the LINE need not be known insertion phase or electrical length need only be specified within $1/4\lambda$

It is noted that, if a non-zero-length THRU is used but specified to have zero delay, the reference plane will be established in the middle of the THRU. Hence, the THRU will have two times length of the REFLECT. According to the above requirements, we use three different kits:

TRL1 is the TRL design with 1.25λ reflect line with an open end.

TRL2 is the TRL design with 1λ reflect line with a short end.

TRL3 is the TRL design with 2.25λ longer reflect line with an open end,

TRL1 is the TRL designing with 1.25λ reflect line with an open end. With the parameters, $l_{REFLECT\_OPEN} = 1.25 \times 10.14mm = 12.68mm$, $l_{THRU} = 2 \times l_{REFLECT\_OPEN} = 2.5\lambda = 25.36mm$ (The length of the THRU line is twice of $l_{REFLECT}$),

$l_{LINE} = 25.8mm$ (The delay-line is chosen to be slightly longer (say 0.3λ) than the THRU line)

The design of the following two kits is similar to the first one.

TRL2_ is the TRL design with 1λ short-ended reflect line

$l_{REFLECT\_SHORT} = 10.14mm$, $l_{THRU} = 2 \times l_{REFLECT\_SHORT} = 2\lambda = 20.28mm$, $l_{gap} = 21.5mm$

TRL3 is the TRL design with 2.25λ longer open-ended reflect line,

$l_{REFLECT\_OPEN} = 2.25 \times 10.14mm = 22.82mm$, $l_{THRU} = 2 \times l_{REFLECT\_SHORT} = 4\lambda = 40.56mm$,

$l_{gap} = 41.5mm$

7 Conclusion

7.1 Project conclusion

The goal of this thesis is to design, fabricate and measure the Ka-band circularly polarized antenna radiator. Two types of radiators are designed, respectively aperture-coupled antenna and GCPW-fed antenna. A simplified cavity model is used to compute the initial geometry model of the aperture-coupled antenna in Chapter 4.3. The theoretical computation of GCPW-fed antenna is based on the solution of mixed-potential integral equations by the method of moment (MoM), involving the evaluation of the Green functions of the structure.

1) It is proved by both computation and simulation results that the length of the patch lp decides the resonant frequency of the patch, and the width of the patch wp mainly influences the resonant impedance of the patch. This is valid for both types of antenna radiators.

2) A truncated nearly square patch has better performance than a truncated square patch in exciting of circular polarization. Because the resonant frequency is decided by the length of the patch (l_p). While tuning the width of the patch (w_p) can change the resonant resistance of the patch. When a square patch is used to excite CP, it is found that the good impedance matching and good axial ratio can not be achieved at the same frequency. A nearly square patch can offer one more dimension to tune than the square patch. One can tune the width of the patch to adjust the resonant impedance of the patch in order to make both impedance matching and the good axial ratio in the operating frequency bandwidth.

3) The simulation results show that, as long as the impedance matching is kept, the transition-VIA would not have much influence on the antenna's behavior, as we expected. Moreover, the transition-VIA helps to diminish the backward radiation.

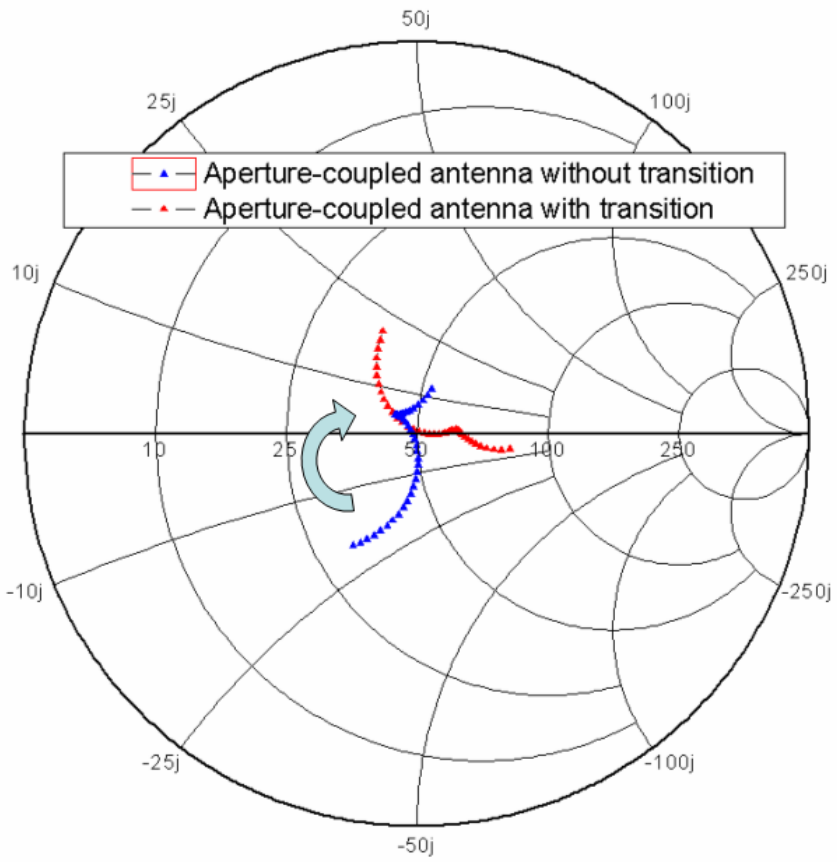

Figure 72: Comparison of input impedances for the aperture-coupled antenna with and without transition-VIA

4) Compared to the aperture-coupled antenna, GCPW-fed antenna has broader bandwidth (see Figure 73), low radiation loss, dispersion and broader bandwidth, as a result of supporting quasi-TEM mode propagation as the dominant mode. Moreover, the GCPW-fed antenna is more possible to use smaller patch size, because it performances well on high dielectric constant substrate, for example, Rogers RT/duroid 6010/6010LM ($\varepsilon_r = 10.2$) or Rogers TMM 10i(tm) ($\varepsilon_r = 9.8$). Additionally, it needs only two substrate layers, which reduce the costs.

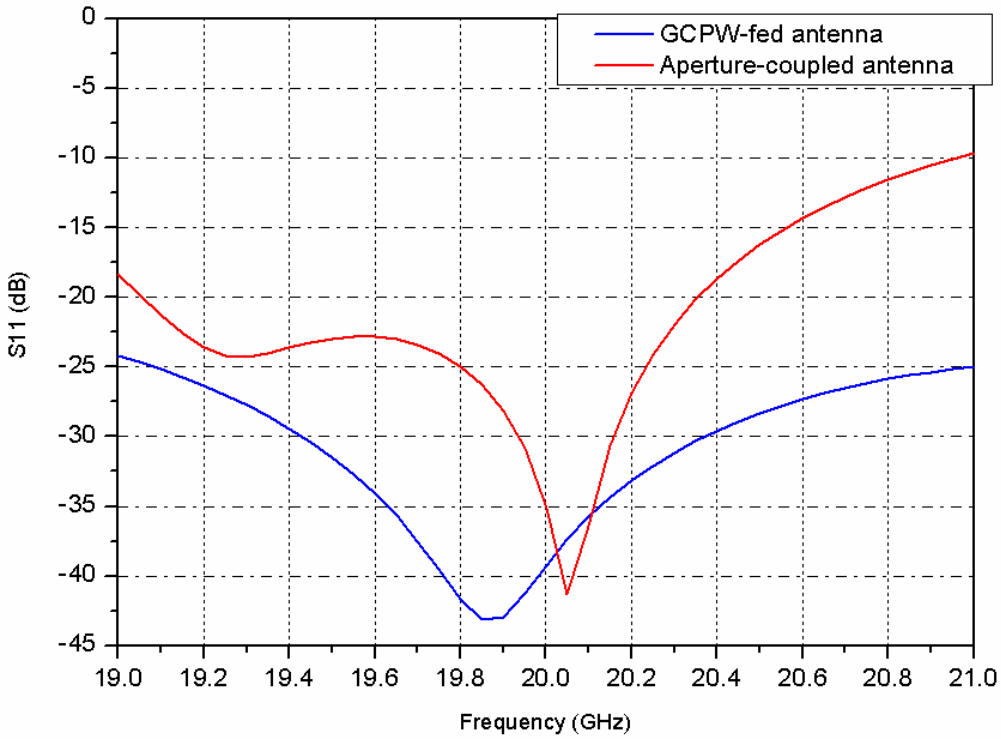

Figure 73: Comparison of impedance matching bandwidth of the two types of antennas

5) For the GCPW-fed antenna, the parallel-plate modes (PPM) cause the surface wave which reduces the radiation efficiency. Adding series of vias along the GCPW feedline can reduce the PPM level, and the density of the vias needs to be properly chosen.

7.2 Improvement suggestion

1) Reducing the size of antenna patch

As the maximum limitation of 0.5λ distance between the adjacent element, size of the antenna patch should be as small as possible, in order to reduce the mutual coupling. In this project, RT/duroid 5880 ($\varepsilon_r = 2.2$) is chosen to be the patch substrate. As presented in Chapter 4.3, the computation result from the cavity model gives $lp = 5.06mm$, after optimized in HFSS, we have $lp = 4.85mm$. In this case, the antenna array will have better performance if we could reduce the size of patch till around 4mm. From the cavity model, we know that the length of the patch is mainly determined by the operating central frequency and the ε_{eff}. Since the operating central frequency is already fixed at 19.95 GHz, we can only change ε_{eff} by choosing another substrate with higher dielectric constant than RT/duroid 5880, for example, RO4003 ($\varepsilon_r = 3.38$).

2) Adding via-array

As single radiator of an antenna array, the unwanted modes should be diminished to extremely low level so as to reduce the interference between the adjacent elements. Thus, adding vias between the grounds can be a good solution. There are no specific rules or instructions about where to add vias. In this design, the positions of the vias can be chosen according to the plotted E-field of the grounds, vias are inserted to the positions where PPM standing waves appear.

Moreover, a via-array could be considered to add between the ground planes. Some previous studies show that, the density of via array influences the input impedance of the radiator more and more greatly when the working frequency increases. The package resonance of the shorting via arrays can be completely removed from DC to several gigahertz frequency ranges by properly selecting the density of shoring via-arrays [27]. In this project, the working frequency band is too high to choose an appropriate density of the via-array. Thus, it is extremely tough to completely remove the package resonance from DC to Ka- band. However, there is a possibility to remove the package resonance out of the working frequency bandwidth by selecting a proper via array density.

3) Using etched silicon structure for the CPW-fed antenna

In order to reduce the level of backward radiation from the CPW and also to remove the heat from MMIC active component circuit, a shielding plane is added to the back of CPW, hence a grounded CPW (GCPW) is formed. However, the presence of this shielding plane and the CPW ground plane promote the generation of parallel plate modes (PPM), which reduces the efficiency of the antenna. The adaptive suggestion is to use an etched silicon structure, that is, to add air cavities to enclose the antenna [29]. Figure 74 shows the comparison of the GCPW-fed antenna and CPW-fed antenna on etched silicon. The adaptive structure has several advantages. First, the layer structure is even simpler than the GCPW-fed antenna. Theoretically, it needs only three layers including the transition-VIA. Second, instead of using a conductor-backed CPW, this structure uses air cavities to control the coupling level and reduce the backward radiation, which can com-pletely remove the unwanted PPM. However, there are some unclear factors about this structure, such as the manufacturing and machining issues might be critical. Also, the cavity tends to diminish the achievable impedance bandwidth.

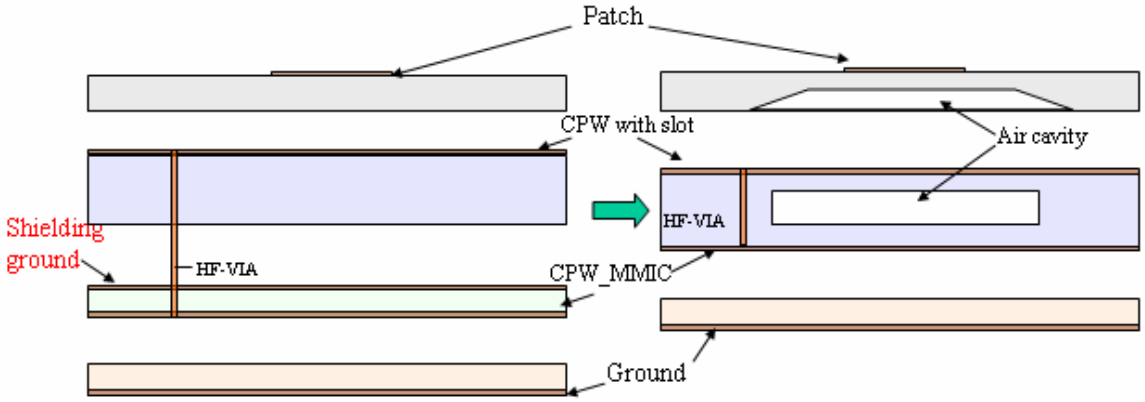

Figure 74: Comparison of GCPW-fed antenna (on the left) and CPW-fed slot-coupled microstrip antenna on etched silicon (on the right)

4) Using thick substrate with low dielectric constant beneath CPW

Due to the time limits, the author couldn't complete the optimization of GCPW-fed model. Two kinds of approach can be done in the future. One is as presented in (3), the other is to use a thick substrate with low dielectric constant beneath CPW. Some test models are simulated. It is found that when using RT 5880 ($\varepsilon_r = 2.2$) as the CPW substrate, the thickness of the substrate is better more than 1.5 mm. Due to the transition-VIA's total length having a limitation of 2.4 mm, it is critical to use this kind of structure with the original transition-VIA, which means, some adaptive should be done on the transition-VIA part to make it possible for longer vias.

Additionally, a problem when using thin substrate thickness for a GCPW-fed antenna should be noticed. When the substrate thickness of the CPW is less than the substrate thickness of the patch, which is above the CPW feedline, how to place the excitation port becomes a tricky problem. In this project, the HFSS model of the GCPW-fed antenna is imported from the Ansoft Designer v2.1 model, so there is a default built-up model done by the program itself. Some more study need to be done on this port, trying to change the size and the position in Z-axis, to make sure the port will not influence much on the simulation results.

5) Measurement equipment for CPW

In this project, due to the substrate material and measurement surroundings problems, the GCPW-fed antenna is not selected to be fabricated in the end. Anyhow, there are some suggestions to the future measurement to the CPW structures. We take the GCPW-fed antenna in this project for example. The best solution to measure a narrow CPW line is using a CPW probe station as shown in Figure 75. The CPW probe station could supply the probes that are small enough for the narrow CPW line and give more accurate result for the S parameters than the connector. The relevant information could be found at the website http://www.ggb.com/ .

Figure 75: Probe stations for the CPW measurement

Acknowledgement

This project is funded by German Ministry of Education and Research (BMBF) under administration of German Aerospace Center (DLR) covered by research contracts 50YB0101 and 50YB0104. I sincerely thank to DLR and Antenna group in Chalmers University of Technology facilitating and giving administration authorities to my master thesis project. I am very grateful to Prof. Per-Simon Kildal, Head, Antenna group, CTU, for his encouragement and assessing the result of my work.

I would like to thank Prof. A. Schroth, Head, Navigation & Guidance systems for accepting my nomination. I wish to thank Dr. A. Dreher, Head, Antenna Research Group for providing good facilities and working environment. I specially thank to Dr. Michael Thiel for giving much guidance to my work and helping me with the pre- and post- fabrication works.

I would like to extend my thanks to Marcos V. T. Heckler for continuous support especially his knowledge in impedance matching, which is included in Chapter 4.6. I want to extend my thanks to Dr. Yang Jian, Antenna group in CTU for his support and encouragement. I would like to extend my thanks to Frau Krumbholz, librarian for literature support. I would extend my thanks to research fellows Mi Hong, Giang and all the members of Antenna research group, DLR for their valuable company.

References

[1] C. Hunscher, M. Thiel, A. Dreher, S. Holzwarth, L. C.Stange, H. Pawlak, A. Molke, A. F. Jacob, “Smart Antenna Terminal (SANTANA)-Final Report”, BMBF und DLR 50YB0101, June, 2004.

[2] C. Hunscher, R. Mayer, A. Jacob, L.C. Stange, A. Dreher, L.Richard, N.Niklasch, “Active antenna for multimedia communication over satellite”, final report, MNBF Vorhaben 50 Y 0004, Dec. 2001

[3] Per-Simon Kildal, “Foundations of antennas”, Chapter 5 of “Microstrip antennas, and spectral domain methods”, ISBN 91-44-01322-1, 2000

[4] R. Garg, P. Bhartia, I. Bahl, A. Ittipiboon, “Microstrip antenna design handbook”, ISBN 0-89006-513-6, 2000.

[5] Stephen D. Targonski and David M. Pozar, “Design of Wideband Circularly Polarized Aperture-coupled Microstrip Antennas”, IEEE Trans. On antennas and propagation, vol. 41, NO. 2, pp. 214-220, Feb. 1993.

[6] John Huang, “A Ka-band circularly polarized high-gain microstrip array antenna”, IEEE Transactions on antennas and propagation, vol. 43, NO.1, Jan. 1995.

[7] N.Herscovici and David M. Pozar, “Full-wave analysis of aperture-coupled microstrip lines”, IEEE Trans. Microwave Theory and Techniques, vol.MTT-39, pp.1108-1114, July 1991.

[8] David M. Pozar, “A review of aperture coupled microstrip antennas: History, Operation, Development, and Applications”, May 1996.

[9] Laurent Giauffret, Jean-Marc Laheurte, A. Papiernik, “Study of various shapes of the coupling slot in CPW-fed microstrip antennas”, IEEE Transactions on antenna and propagation, vol.45, NO.4, April 1997.

[10] David M. Pozar, “A microstrip antenna aperture coupled to a microstrip line”, Electronics Letters, vol.21, no.2,pp.49-50, January 1985.

[11] P. Bhartia, K. V. S. Rao and R. S. Tomar, “Millimeter wave microstrip and printed circuit antennas”, Artech House, 1991.

[12] David M. Pozar, “A reciprocity method of analysis of printed slot and slot-coupled microstrip antennas”, IEEE Transactions on antenna and propagation, vol. AP-34, pp.1439-1446, Dec. 1996.

[13] J. P. Daniel, G. Dubost, C. Terret, “Research on planar antennas and arrays: Structures Rayonnantes”, IEEE Tansactions on antenna and propagation, vol.35, NO. 1 Feb. 1993.

[14] Paolo Moretti, J. Piotr Starski, Bengt I Svensson, Lars Manholm, “Numerical Investigation of Vertical Contactless Transitions for Multilayer RF Circuits”, Chalmers University of Technology, Ericsson Microwave systems.

[15] J.Moore, R.Pizer, “Moment Methods in Electromagnetic Techniques and Applications”. Chapter 11 of “Antennas Mounted on Vehicles on an Imperfect Ground Plane, Vo4.3: Network-analyzer experiments”. Research Studies Press LTD., England, 1986.

[16] N. Herscovici, “CAD of aperture fed microstrip transmission lines and antennas: software and user’s manual” Artech House, 1996.

[17] Gupta, K. C., et al., “Microstrip Lines and Slot Lines”, 2nd ed., Artech House, Norwood, MA,1996.

[18] Kobayashi, H. K. Hirasawa, and K. Fujimoto, “Slot Array Antennas Fed by Coplanar Waveguide for Millimeter wave Radiation,” IEEE Trans. on Microwave Theory and Techniques, vol. MTT-46, 1998, pp. 800-805.

[19] L. Giauffret, J. M. Laheurte, “Theoretical and experimental characterization of CPW-fed microstrip antennas”, IEEE Pro.-Microwave and Antennas Propagation, vol. 143, No. 1, Feb. 1996.

[20] Jean-Marc Laheurte, Linda P.B. Katehi and Gabriel M. Rebeiz, “CPW-Fed Slot Antennas on Multilayer Dielectric Substrates”, IEEE Transactions on antenna and propagation, vol.44, NO.8, Aug. 1996.

[21] Steven Mestdagh, Walter De Raedt, Guy A.E. Vandenbosch, “CPW-Fed Stacked Microstrip Antennas”, IEEE Transactions on antenna and propagation, vol.52, NO.1, January 2004.

[22] Tatsuo Itoh, “Overview of Quasi-Planar Transmission Lines”, part IV, IEEE Transactions on microwave theory and techniques, vol.37, NO. 2, Feb. 1989.

[23] Robert W. Jackson, “Mode Conversion at Discontinuities in Finite-Width Conductor-Backed Coplanar Waveguide”, IEEE Transactions on Microwave Theory and Techniques, vol. 37, No. 10, Oct. 1989.

[24] J. Zehentner, J. Machae, “Properties of CPW in the Sub-mm Wave Range and Its Potential to Radiate”, Czech Technical University, on the internet.

[25] Tatsuo Itoh, “Overview of Quasi-Planar Transmission Lines”, part IV, IEEE Trans. on microwave theory and techniques, vol.37, NO. 2, Feb. 1989.

[26] Edward M. Godschalk, “ Surface wave phenomenon in wafer probing environments”, Cascade Microtech Inc., 1992.

[27] Jiayuan Fang, Jin Zhao and Jingping Zhang, “Shorting Via Arrays for the Elimination of Package Resonance to Reduce Power Supply Noise in Multi-layered Area- Array IC Packages”, IEEE Symposium on IC/Package Design Integration, Feb,1998, Santa Cruz, CA.

[28] Agilent Technologies, “Agilent Network Analysis Applying the 8510 TRL Calibration for Non-coaxial Measurements---Product Note 8510-8A”, part 1, May 2001.

[29] Chris R. Trent, Tom M. Weller, “ Design and Tolerance Analysis of a 21 GHz CPW-fed, Slot-Coupled, Microstrip Antenna on Etched Silicon”, The University of South Florida, 2002.

Appendix A

Magnetic Green functions

This Appendix contains the expressions of the magnetic Green functions for a horizontal magnetic dipole located at the ground plane level ($z_0 = -h$) (see Figure 76)

$$G_{Fx}^{air} = \frac{\varepsilon_0}{4\pi} S_0 \left[\frac{\varepsilon_{diel}}{\cosh(u_{diel} h) DTM} e^{-u_{air} z} \right],$$

$$G_{Fx}^{diel} = \frac{\varepsilon_0}{4\pi} S_0 \left[\frac{\varepsilon_{diel}}{\cosh(u_{diel} h) DTM} \times \left(\cosh(u_{diel} z) - \frac{\varepsilon_r u_{air}}{u_{diel}} \sinh(u_{diel} z) \right) \right],$$

$$G_{Fz}^{air} = -\frac{\varepsilon_0}{4\pi} \cos\theta (\varepsilon_{diel} - 1) S_1 \left[\frac{1}{DTM.DTE} \frac{e^{-u_{air} z}}{\cosh(u_{diel} h)} \right],$$

$$G_{Fz}^{diel} = -\frac{\varepsilon_0}{4\pi} \cos\theta (\varepsilon_{diel} - 1) S_1 \left[\frac{\varepsilon_{diel}}{DTM.DTE} \frac{2\sinh\left(u_{diel}(z+h)\right)}{\sinh(2u_{diel} h)} \right],$$

$$G_{\phi}^{air} = \frac{1}{4\pi\mu} S_0 \left[\frac{e^{-u_{air} z}}{DTM \cosh(u_{diel} h)} \times \left(\varepsilon_{diel} - \frac{u_{air}\left(\varepsilon_{diel} - 1\right)}{DTE} \right) \right],$$

$$G_{\phi}^{diel} = \frac{1}{4\pi\mu} S_0 \left[\frac{\cosh(u_{air} z) - \frac{\varepsilon_{diel} u_{air}}{u_{diel}} \sinh\left(u_{diel} z\right)}{DTM \cosh(u_{diel} h)} + \frac{2\left(\varepsilon_{diel} - 1\right) u_{diel} \cosh\left(u_{diel}\left(h+z\right)\right)}{DTM.DTE.\sinh\left(2u_{diel} h\right)} \right],$$

where

$$DTE = u_{air} + u_{diel} \coth\left(u_{diel} h\right),$$
$$DTM = \varepsilon_{air} u_{air} + u_{diel} \tanh\left(u_{diel} h\right),$$
$$u_{air} = k_\rho^2 - k_0^2,$$
$$u_{diel} = k_\rho^2 - \varepsilon_{diel} k_0^2$$

and k_ρ is the spectral variable, z the observer position, θ the angle between source and observer, and $S_n[\ ]$ the Sommerfeld integral of degree n.

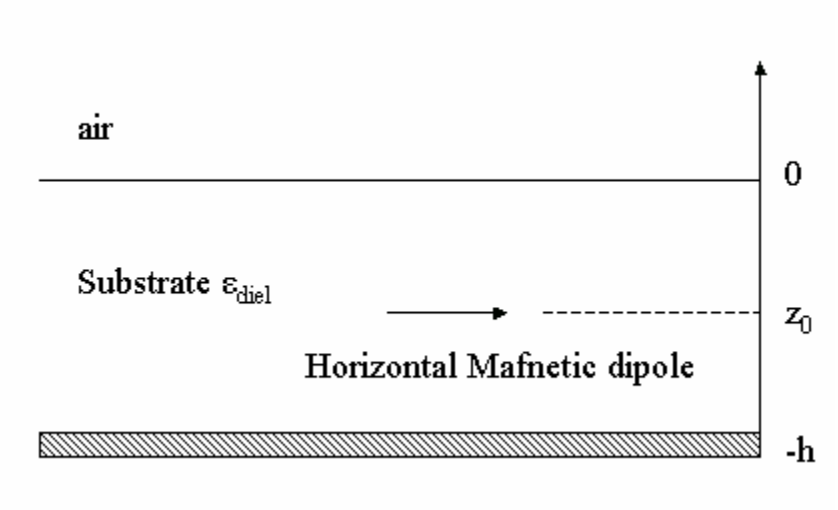

Figure 76: Horizontal magnetic dipole